TOWARDS QUANTITATIVE PHYSICS-INFORMED DEVICE LEVEL MODELS FOR ORGANIC LIGHT-EMITTING DIODES

Zur Erlangung des akademischen Grades eines

Doktors der Naturwissenschaften (Dr. rer. nat.)

von der Fakultät für Physik des
Karlsruher Instituts für Technologie (KIT)

angenommene

Dissertation

von

M. Sc. Simon Kaiser

Tag der mündlichen Prüfung:	19.05.2023
Erster Gutachter:	Prof. Dr. Wolfgang Wenzel
Zweiter Gutachter:	Prof. Dr. Markus Garst

This work is licensed under a Creative Commons 'Attribution-ShareAlike 4.0 International' license.

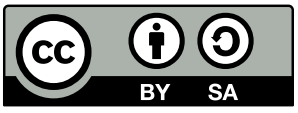

ERKLÄRUNG

Ich versichere hiermit, dass ich meine Doktorarbeit selbständig und unter Beachtung der Regeln zur Sicherung guter wissenschaftlicher Praxis im Karlsruher Institut für Technologie (KIT) in der aktuellen Fassung angefertigt habe.

Karlsruhe, 12.04.2023

Simon Kaiser

PUBLICATIONS

Some ideas and figures have appeared previously in the following

Articles

† indicates equal contributions

[A1] **S. Kaiser**, T.-H. Ke, F. Symalla, T. Neumann, A. D. Özdemir, A. Fediai and W. Wenzel. 'De Novo kMC Simulation of a Complete OLED Stack'. *in preparation*. 2023.

[A2] T. Neumann, F. Symalla, T. Strunk, A. Feidai, **S. Kaiser**, P. Friederich and W. Wenzel. '28-1: *Invited Paper*: Bottom-Up OLED Development by Virtual Design: Systematic Elimination of Performance Bottlenecks Using a Microscopic Simulation Approach'. In: *SID Symposium Digest of Technical Papers* 53.1 (2022), pp. 322–325. DOI: 10.1002/sdtp.15485.

[A3] C. Degitz, M. Konrad, **S. Kaiser** and W. Wenzel. 'Simulating the Growth of Amorphous Organic Thin Films'. In: *Organic Electronics* 102 (2022), p. 106439. DOI: 10.1016/j.orgel.2022.106439.

[A4] A. D. Özdemir†, **S. Kaiser**†, T. Neumann, F. Symalla and W. Wenzel. 'Systematic kMC Study of Doped Hole Injection Layers in Organic Electronics'. In: *Frontiers in Chemistry* 9 (2022). DOI: 10.3389/fchem.2021.809415.

[A5] **S. Kaiser**, N. B. Kotadiya, R. Rohloff, A. Fediai, F. Symalla, T. Neumann, G.-J. A. H. Wetzelaer, P. W. M. Blom and W. Wenzel. 'De Novo Simulation of Charge Transport through Organic Single-Carrier Devices'. In: *Journal of Chemical Theory and Computation* 17.10 (2021), pp. 6416–6422. DOI: 10.1021/acs.jctc.1c00584.

[A6] **S. Kaiser**, T. Neumann, F. Symalla, T. Schlöder, A. Fediai, P. Friederich and W. Wenzel. 'De Novo Calculation of the Charge Carrier Mobility in Amorphous Small Molecule Organic Semiconductors'. In: *Frontiers in Chemistry* 9 (2021), p. 1082. DOI: 10.3389/fchem.2021.801589.

[A7] **S. Kaiser**, F. Symalla, D. Wehl, T. Neumann and W. Wenzel. '22-3: Tuning ETL Mobility by Disorder Passivation'. In: *SID Symposium Digest of Technical Papers* 52.1 (2021), pp. 270–273. DOI: 10.1002/sdtp.14666.

[A8] F. Symalla, A. Fediai, J. Armleder, **S. Kaiser**, T. Strunk, T. Neumann and W. Wenzel. '43-3: Ab-initio Simulation of Doped Injection Layers.' In: *SID Symposium Digest of Technical Papers* 51.1 (2020), pp. 630–633. DOI: 10.1002/sdtp.13946.

[A9] P. Friederich, A. Fediai, **S. Kaiser**, M. Konrad, N. Jung and W. Wenzel. 'Toward Design of Novel Materials for Organic Electronics'. In: *Advanced Materials* 31.26 (2019), p. 1808256. DOI: 10.1002/adma.201808256.

[A10] F. Symalla, P. Friederich, **S. Kaiser**, T. Strunk, T. Neumann and W. Wenzel. '26-4: Computer-Aided Optimization of Multilayer OLED Devices'. In: *SID Symposium Digest of Technical Papers* 49.1 (2018), pp. 340–342. DOI: 10.1002/sdtp.12556.

Presentations

[P1] **S. Kaiser**, F. Symalla, T. Neumann, A. Plews, D. V. Velpen, E. Vandeplas, T.-H. Ke and A. Nejim. '(Invited) Automated Multiscale Design Flow for Organic LED Design'. In: *ECS Meeting Abstracts* MA2021-01.32 (2021), p. 1059. DOI: 10.1149/MA2021-01321059mtgabs.

[P2] **S. Kaiser**, F. Symalla, D. Wehl, T. Neumann and W. Wenzel. 'Tuning ETL Mobility by Disorder Passivation'. SID (virtual). 2021.

[P3] T. Neumann, F. Symalla, D. Wehl, T. Strunk, **S. Kaiser** and W. Wenzel. 'Digital Twins in OLED Development: A Review on Virtual Characterization and Improvement of OLED Materials and Devices'. IMID (Seoul). 2021.

[P4] T. Neumann, F. Symalla, **S. Kaiser**, A. Fediai and W. Wenzel. 'Parameter-Free OLED Device Simulations with Doped Injection Layers'. IMID (Seoul). 2020.

[P5] F. Symalla, A. Fediai, J. Armleder, **S. Kaiser**, T. Strunk, T. Neumann and W. Wenzel. 'Ab-Initio Simulation of Doped Injection Layers.' SID (virtual). 2020.

[P6] F. Symalla, P. Friederich, **S. Kaiser**, T. Strunk, T. Neumann and W. Wenzel. 'Computer-Aided Optimization of Multilayer OLED Devices'. SID (Los Angeles). 2018.

Poster presentations

- Paris International School on Advanced Computational Materials Science (PISACMS), 2018, Paris, France
  Influence of mesoscopic structure on device properties of organic solar cells

- European Materials Research Society (E-MRS) Spring Meeting 2019, Nice, France
  Ab initio charge transport simulation of amorphous small molecule organic semiconductors

- KIT im Rathaus, Karlsruhe, 2019, Germany
  Simulationsgestützte Optimierung organischer Leuchtdioden

Project contributions

- 'Multi-Skalen-Modellierung von Materialien und Bauelementen für die Energieumwandlung' (MSMEE) funded by the Baden-Württemberg Stiftung

- 'EXTended Model of Organic Semiconductors' (EXTMOS) funded by the European Union Horizon 2020 research and innovation programme

CONTENTS

1

INTRODUCTION

Organic semiconductors (OSCs) are a class of material based on organic molecules or polymers with similar applications as inorganic semiconductors, e.g. as organic light-emitting diodes (OLEDs) [1], organic solar cells (OPVs) [2] or organic field-effect transistors (OFETs) [3]. These OSCs offer unique possibilities in device manufacture and use, such as cost-effective mass production via printing applications or spin-coating [4], aided by the low cost of required materials [5], and the possibility of building flexible devices (demonstrated in fig. 1.1).

While OPV and OFET applications are still in their infancy, OLEDs have evolved into a fully commercialized technology for lighting and display applications [1, 6]. By now, OLED displays have become the standard technology in smart phones, are on the rise for TV applications and are receiving increasing interest in the automotive area due to technical advantages such as flexibility [7], transparency [8], low thickness and the potential to produce displays in arbitrary shapes [9]. Despite their high level of technological readiness, OLEDs still face a major challenge that hinders the exploitation of their full potential: In spite of decades of research and Bn$ investments, especially devices emitting light in the deep-blue colour range suffer from limited efficiency and low lifetimes. The potential in the design of OPV devices – thin, flexible, semi-transparent at various colours – enables a new level of flexibility in integrating OPV into everyday infrastructure, such as windows, blinds or walls of high-rise structures. Production on a large scale, e.g. with roll-to-roll printing, allows fabrication of comparably cheap devices even on large areas. However, OPVs still lag too far behind inorganic solar cells in both efficiency and lifetime to be viable for use in a large-scale. Application of OFET technology is currently limited to inexpensive devices where computational performance and transistor size are not crucial, e.g. printed radio-frequency identification (RFID) tags in logistics.

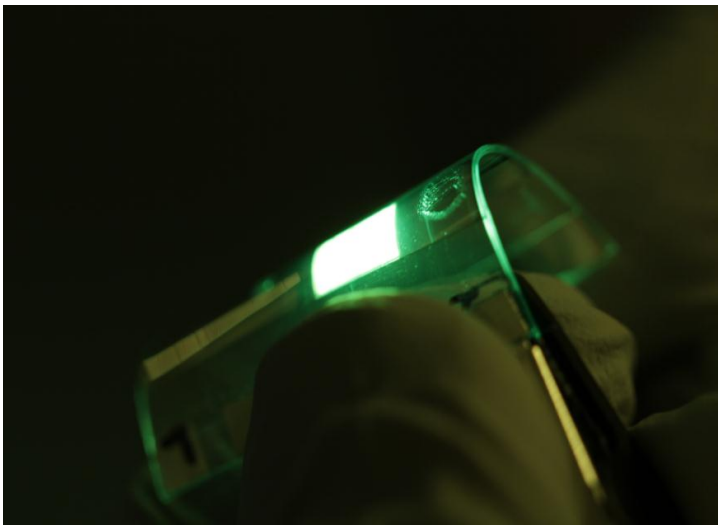

Figure 1.1: Flexible OLED manufactured at the Light Technology Institute at KIT. Photograph taken by Ralph Eckstein.

This work focuses on the, presently, most relevant application of OSCs, OLEDs, while the methods are applicable to OPVs and, to a lesser extent, OFETs as well. Starting with the discovery of electroluminescence in organic materials by Pope et al. [10] and Helfrich et al. [11] in the 1960s and spurred by the discovery of electroluminescence at low voltages by Tang and Van Slyke in 1987 [12], researchers have made great efforts at improving OLED device performance [13]. Synthetization of phosphorescent and later thermally activated delayed fluorescence (TADF) emitter molecules raised the achievable internal quantum efficiency (IQE) from 25 % to 100 % [14, 15]. Chemical doping reduced the injection barriers into the OLED and increased the number of mobile charge carriers [16–18]. Addition of layers with specifically targeted materials confine excitons to the emissive layers (EMLs) and improve charge carrier balance within the device, reducing loss processes [1, 6]. These improvements have lead to the modern OLED evolving from the comparatively primitive single- or bilayer to finely tuned multilayer devices with each layer comprising one or more organic materials, each serving a specific function [19–21]. Recent advances to overcome bottlenecks employ increasingly complex emission systems, e.g. hyperfluorescence and co-emission, resulting in devices with high efficiency [22–26]. The comparably short operational lifetime of deep-blue devices, however, limits the practical application of OLEDs in display and lighting applications [22–25, 27, 28].

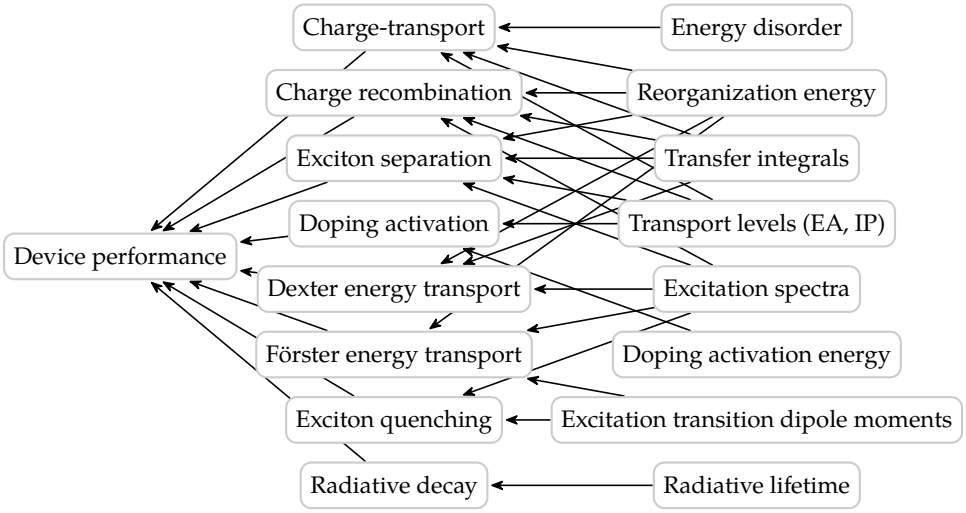

Figure 1.2: An entangled interplay of microscopic processes and material properties determines the performance of OLED devices.

A central challenge in the design of efficient and durable devices is the high level of complexity, induced by an entangled interplay of a multitude of microscopic processes that determine device performance. The above mentioned notion to improve on device deficiencies with increasingly intricate setups further adds to the overall complexity. The microscopic processes are triggered and influenced by a large number of material properties with complex interdependences, sketched in fig. 1.2. However, balancing these processes is the key to designing durable and efficient devices. Experimental observation of these processes is limited to secondary effects and averaged quantities, turning device design by experiment alone into a process of trial and error. These trial and error approaches can produce viable devices only by imposing severe restrictions on the otherwise vast parameter space, especially by regarding only a small number of candidate molecules. Computational models that resolve these microscopic processes and quantify their rates can aid lift these restrictions and systematically identify, and consequently resolve, performance bottlenecks.

While eliminating performance bottlenecks and thereby increasing the lifetime of OLEDs seems to be an optimization task on the level of device engineering, it actually requires balancing of the microscopic processes which are rooted in fundamental physics, namely the quantum nature of organic matter, and is therefore subject to fundamental research in physics and chemistry. To support experimental efforts, com-

putational approaches have long since been established in OLED research and development [29, 30]: Quantum chemistry methods, e.g. density-functional theory (DFT), are applied on the molecular level to compute basic material properties, such as highest occupied molecular orbital (HOMO), lowest unoccupied molecular orbital (LUMO) or excitation energies [31]. While these methods are well established, they fail to include environmental effects and therefore cannot correctly predict the impact of structural molecular properties on device performance. On the device level, drift-diffusion models were adapted from inorganic semiconductor simulations to compute device properties like the current density–voltage (J–V) characteristic. These methods, however, are based on parametric continuum-scale models, requiring calibration with experiment, thereby inheriting the limitations of experiment discussed above and cannot be used for fully virtual design.

To bridge the gap between fundamental chemistry and device design, multiscale simulation approaches for organic electronic applications have been recently developed [32–35]. In these simulations charge carrier and exciton dynamics are computed at the mesoscopic scale via the simulation of millions of single microscopic processes – charge hops, exciton formation and transport, etc. – with rates based on molecular properties. However, mesoscopic modelling of OLEDs is still challenging due to the low permittivity of OSC materials necessitating explicit treatment of the electron–electron interaction, as well as the interplay of energy disorder and charge transport. Ultimately, though, this approach does not require parametrization with experiment and enables fully virtual design. The device characteristics computed with such a multiscale workflow, e.g. charge and exciton trajectories, provide a unique insight into the device operation, since many relevant processes are not readily, some even not at all, accessible experimentally, enabling researchers to systematically understand and eliminate performance bottlenecks in OLED devices [36].

To date, *de novo* simulations, i.e. without parametrization with experiment, have been applied to address individual aspects of OLED design, such as charge transport [34, 37, 38] or excitonic quenching [39] in simplified devices, while the next step of device modelling, the microscopic simulation of charge and exciton dynamics in complete OLEDs stacks, was limited to models parametrized with experimental data [36, 40].

In this thesis, I will improve the current methods to achieve the *de novo* multiscale simulation of a full OLED stack to experimental accuracy. To this end, chapter 2 introduces the properties of organic small molecules and OSCs, the working principle of OLEDs and an overview of fundamental methods used in the multiscale workflow. Chapter 3 discusses the multiscale workflow used throughout this work. Chapter 4 improves the workflow to compute reliable, accurate and precise material and device properties, benchmarking the multiscale workflow on a large number of materials and systems. Besides these benchmarks, the chapter contrives a simple method to improve electron mobility in electron transport materials. Chapter 5 extends the workflow to include doped injection layers, which are crucial parts of efficient OLEDs. Chapter 6 uses the multiscale workflow to parametrize macroscopic drift-diffusion models and presents a general method to circumvent performance penalties of the kinetic Monte-Carlo (kMC)[41] device model, e.g. stemming from the inclusion of doped injection layers, which impede the simulation of complete OLED stacks. Finally the enhanced multiscale workflow is used to compute the device characteristics of a complete OLED stack both with a macroscopic drift-diffusion model and the kMC device model *de novo*.

2

FUNDAMENTALS

This chapter gives a brief overview on charge and exciton transport in disordered organic semiconductors (OSCs), the working principles of the organic light-emitting diode (OLED) as an application of OSC and the main focus of this work, as well as fundamental theory and methods required for the multiscale simulation methods described in chapter 3.

Section 2.1 briefly discusses the fundamental principles of OSCs. Organic light-emitting diodes (OLEDs), as one of the application of OSCs, are introduced in section 2.4. Sections 2.2 and 2.3 discuss charge and energy transport of OSCs and theoretical models to describe them. Finally the basic principles of two methods fundamental for the multiscale workflow, density-functional theory (DFT) and kinetic Monte-Carlo (kMC)[41], are presented in sections 2.5 and 2.6.

2.1 PROPERTIES OF ORGANIC SEMICONDUCTORS (OSCS)

OSCs consist of organic small molecules or polymers, which are vapour deposited or solution processed into thin films. The molecules are non-covalently bound by Van der Waals interaction forming amorphous or crystalline structures depending on their molecular structure and processing conditions. This work focuses on organic small molecules vapour deposited into thin amorphous films, as these are prevalent in OLEDs applications [4].

Semiconducting properties arise for aromatic molecules with conjugated double bonds. The overlapping sp^2 orbitals of neighbouring molecules form σ-bonds while the remaining p_z orbitals hybridize to delocalized π-orbitals, as depicted in fig. 2.1. Due to the large overlap of sp^2 orbitals, σ-bonds are stronger than π-bonds, leading to the latter de-

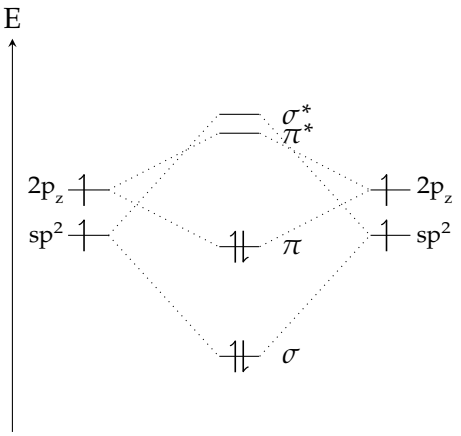

Figure 2.1: sp^2 and $2p_z$ orbitals of a C–C double bond splitting into bonding and anti-bonding σ and π molecular orbitals.

termining the chemical properties of the molecule. Hybridization opens a gap between bonding and non-bonding orbitals, with the bonding π-orbital as highest occupied molecular orbital (HOMO) and non-bonding π*-orbital as lowest unoccupied molecular orbital (LUMO) [42].

2.2 CHARGE TRANSPORT IN AMORPHOUS OSCS

Polarization effects induced by neighbouring molecules lead to small variations in the energy of each molecule, well approximated by a Gaussian distribution of states [43–47]. The half-width of this Gaussian distribution is referred to as energetic disorder (σ) and is in the order of $\mathcal{O}(100\,\text{meV})$. Polarization effects in the medium influence the energy levels of a molecule, replacing HOMO and LUMO with ionization potential (IP) and electron affinity (EA) as polaron energy levels relevant for charge transport.

In contrast to inorganic semiconductors, electronic states in OSCs strongly localize on single molecules due to weak intermolecular coupling and strong energetic disorder [48]. These localized electronic states restrict charge transport to a sequence of hopping processes between neighbouring molecules [49, 50]. The rate of these hopping processes can be approximated with the semi-empiric Arrhenius type Miller–Abrahams or Marcus rates [51] discussed in the following subsections.

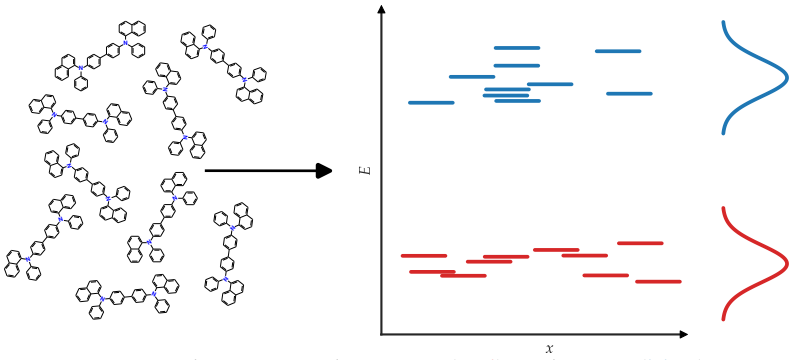

Figure 2.2: In amorphous OSCs, the HOMO (red) and LUMO (blue) energies of the individual molecules vary due to the unique combination of conformation and environment. The distribution of energy levels is well represented each molecule are well approximated by a Gaussian distribution of states.

Going towards more ordered systems than the amorphous molecules studied here, the transport regime crosses over from hopping transport to band-like transport. In this crossover regime, other methods, such as Ehrenfest or surface hopping approaches, can be employed to describe charge transport [52–55].

2.2.1 *Miller–Abrahams rate*

The hopping rate can be approximated by the semi-empiric Miller–Abrahams (MA) rate [56]

$$k_{if} = \omega_0 \left|J_{if}\right|^2 \begin{cases} \exp\left(-\frac{\Delta E_{if}}{k_B T}\right), & \text{for } \Delta E_{if} > 0 \\ 1, & \text{otherwise} \end{cases} \tag{2.1}$$

for a hop from site i to f with the assumption that any amount of excess energy from a hop downward in energy ($\Delta E_{if} < 0$) can be dissipated and an activation energy in the form of a Boltzmann factor is required for a hop upward in energy ($\Delta E_{if} > 0$). The hopping rate is determined by a prefactor ω_0, the electronic coupling J_{if} and the activation barrier, which depends on the energy difference of final and initial state ΔE_{if}, Boltzmann constant k_B and temperature T. In small molecule OSCs, ΔE_{if} can be much larger than the vibrational frequencies of the molecules, leading to a systematic overestimation of hops downward in energy.

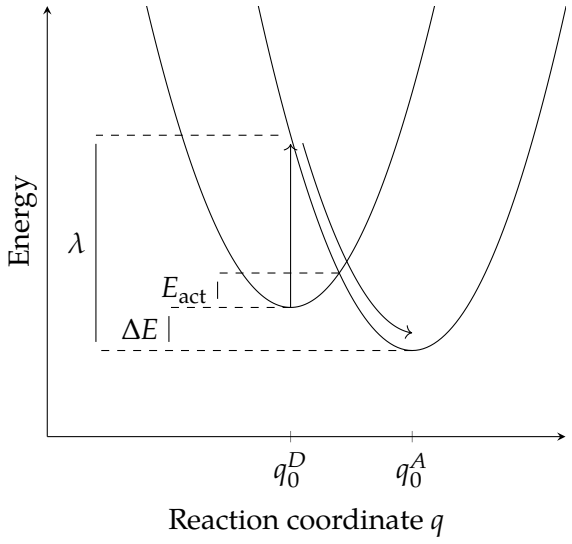

Figure 2.3: Two states of the total system, namely the donor D being charged q_0^D and the acceptor A being charged q_0^A in their respective equilibrium states, represented by Marcus parabolas. Using the harmonic approximation, the activation E_{act} can be calculated from the energy difference of both states ΔE and the reorganization energy λ.

2.2.2 *Marcus theory*

Marcus-theory [57] – originally developed for a quantitative description of electron transfer between reactants in solution – allows formulation of a more sophisticated hopping rate including polaronic effects. As with the MA rate, temperature is assumed to be large compared to the vibrational frequencies $k_B T \gg \hbar\omega$, allowing for a classical treatment of molecular vibrations.

Initially the donor molecule D is charged and the acceptor molecule A is uncharged. The Franck–Condon principle makes a direct electron transfer from A to D very unlikely. However, thermal fluctuations can lead to the system fluctuating into a conformational transition state where the charged states of either molecule are in resonance. Approximating a harmonic potential energy surface, the activation energy for charge transfer, E_{act}, is given by

$$E_{act} = \frac{1}{4\lambda} (\Delta E + \lambda)^2 \tag{2.2}$$

where the reorganization energy

$$\lambda = \frac{\omega_{\text{vib}}}{2}\left(q_0^A - q_0^D\right)^2 \tag{2.3}$$

corresponds to the energy removed from the system to reorganize the conformation of A from the equilibrium conformation with the charge localized on D (q_0^D) to the equilibrium conformation with the charge localized on A (q_0^A), depicted in fig. 2.3.

Combining the full prefactor and activation energy into the Arrhenius equation [58, 59] leads to the Marcus rate [57, 60]

$$k_{DA} = \frac{2\pi}{\hbar}|J_{DA}|^2 \frac{1}{\sqrt{4\pi\lambda k_{\text{B}}T}} \exp\left(-\frac{(\lambda + \Delta E)^2}{4\lambda k_{\text{B}}T}\right) \tag{2.4}$$

with the reorganization energy λ discussed above, temperature T, electronic coupling J_{DA} and energy difference ΔE between localized molecular states on D and A.

2.2.3 *Drift-diffusion equations*

On the macroscopic scale, charge transport in OSC devices can be described using the drift-diffusion (DD) equations established in inorganic semiconductor physics. These describe the current density $J_{n/p}$ as a drift component driven by the external field E and a diffusion component driven by gradients in the charge carrier density n (p) [61]

$$\begin{aligned} J_n &= q\mu_n nE + qD_n\nabla n \\ J_p &= q\mu_p pE - qD_p\nabla p \end{aligned} \tag{2.5}$$

with the elementary charge q, the electron (hole) mobility μ_n (μ_p) and the diffusion constant $D_{n/p}$, given by the generalized Einstein relation [62]

$$D_{n/p} = \mu\eta\frac{k_{\text{B}}T}{q}\,, \tag{2.6}$$

where η is a function of the charge carrier density n (p) and the disorder σ [63]. The continuity equations

$$\begin{aligned} \nabla J_n - q\left(\frac{\delta n}{\delta t}\right) &= qRnp \\ \nabla J_p + q\left(\frac{\delta p}{\delta t}\right) &= -qRnp \end{aligned} \tag{2.7}$$

account for charge conservation, where R is the rate for electron–hole recombination.

The DD equations 2.5 and 2.7, together with the Poisson equation

$$\nabla E = \frac{q(p-n)}{\epsilon_r \epsilon_0}\,, \tag{2.8}$$

give a set of partial differential equations, which can be solved numerically to compute current and charge carrier densities in OSC devices.

2.3 ENERGY TRANSPORT IN AMORPHOUS OSCS

Due to the weak screening at the low permittivity of $\varepsilon_r \approx 3$, commonly found in amorphous OSCs, electron–hole-pairs form tightly bound Frenkel-Excitons with exciton binding energies $E^* \approx 1\,\mathrm{eV}$ [64]. As with single charge carriers, weak intermolecular coupling and energetic disorder lead to the excitons localizing on single molecules. These excitons transfer from donor D^* to acceptor A mostly via non-radiative transport, as low overlap of absorption and emission spectra renders radiative exciton transfer negligible [65]. Non-radiative transfer is possible via Dexter electron transfer or Förster resonance energy transfer (FRET)[66].

Consider a system with one electron localized on donor and acceptor molecule each. In the regime of weak electronic coupling the electronic coupling can be written as [67]

$$\begin{aligned} J &= \left\langle \Psi_i \middle| \hat{V}_\mathrm{C} \middle| \Psi_f \right\rangle \\ &= \frac{1}{2}\left\langle \Psi_\mathrm{D}^*(1)\Psi_\mathrm{A}(2) - \Psi_\mathrm{D}^*(2)\Psi_\mathrm{A}(1) \middle| \hat{V}_\mathrm{C} \middle| \Psi_\mathrm{D}(1)\Psi_\mathrm{A}^*(2) - \Psi_\mathrm{D}(2)\Psi_\mathrm{A}^*(1) \right\rangle \\ &= \frac{1}{2}\left\langle \Psi_\mathrm{D}^*(1)\Psi_\mathrm{A}(2) \middle| \hat{V}_\mathrm{C} \middle| \Psi_\mathrm{D}(1)\Psi_\mathrm{A}^*(2) \right\rangle - \frac{1}{2}\left\langle \Psi_\mathrm{D}^*(1)\Psi_\mathrm{A}(2) \middle| \hat{V}_\mathrm{C} \middle| \Psi_\mathrm{D}(2)\Psi_\mathrm{A}^*(1) \right\rangle \\ &- \frac{1}{2}\left\langle \Psi_\mathrm{D}^*(2)\Psi_\mathrm{A}(1) \middle| \hat{V}_\mathrm{C} \middle| \Psi_\mathrm{D}(1)\Psi_\mathrm{A}^*(2) \right\rangle + \frac{1}{2}\left\langle \Psi_\mathrm{D}^*(2)\Psi_\mathrm{A}(1) \middle| \hat{V}_\mathrm{C} \middle| \Psi_\mathrm{D}(2)\Psi_\mathrm{A}^*(1) \right\rangle \end{aligned} \tag{2.9}$$

with the Coulomb coupling operator $\hat{V}_\mathrm{C}$, the initial state

$$\begin{aligned} \Psi_i &= \Psi_\mathrm{D}^*\Psi_\mathrm{A} \\ &= \frac{1}{\sqrt{2}}\left(\Psi_\mathrm{D}^*(1)\Psi_\mathrm{A}(2) - \Psi_\mathrm{D}^*(2)\Psi_\mathrm{A}(1)\right), \end{aligned} \tag{2.10}$$

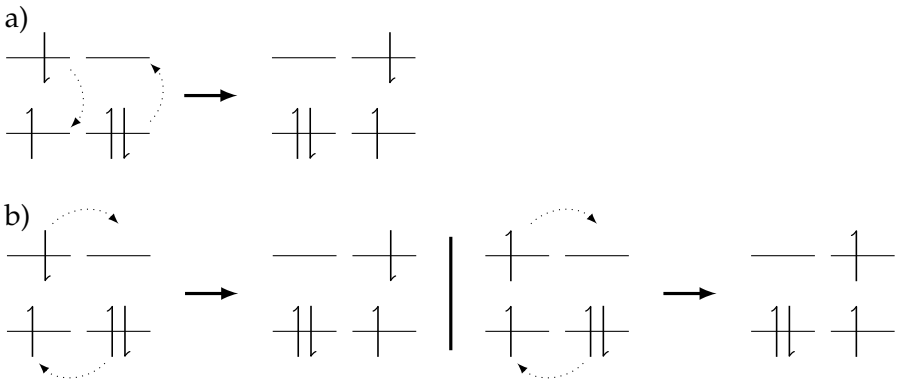

Figure 2.4: a) Förster resonance energy transfer (FRET) of a singlet exciton as correlated excitation and deexcitation of two molecules and b) Dexter transfer of singlet (left) and triplet exciton (right).

and the final state

$$\begin{aligned}\Psi_f &= \Psi_\mathrm{D}\Psi_\mathrm{A}^* \\ &= \frac{1}{\sqrt{2}}\left(\Psi_\mathrm{D}(1)\Psi_\mathrm{A}^*(2) - \Psi_\mathrm{D}(2)\Psi_\mathrm{A}^*(1)\right).\end{aligned} \tag{2.11}$$

The second and third term in eq. 2.9 describe a direct exchange of electrons between both molecules, which is called Dexter transfer [68]. The first and last term in eq. 2.9 describe a correlated excitation of A and de-excitation of D with the electrons staying on their respective molecules. This energy transfer is called FRET. If the distance between the molecules is large compared to their size, the electrostatic interaction can be approximated by the dipole–dipole interaction. Then the Förster coupling is given by

$$J_\mathrm{DA}^\mathrm{Förster} \approx \frac{\left|\vec{d}_\mathrm{D}\right|\left|\vec{d}_\mathrm{A}\right|}{r_\mathrm{DA}^3}\kappa \tag{2.12}$$

with the dipole moments of acceptor and donor, $\vec{d}_\mathrm{A}$ and $\vec{d}_\mathrm{D}$, the distance between A and D, r_DA, and an orientation factor, $\kappa = \cos\phi - 3\cos\theta_\mathrm{D}\cos\theta_\mathrm{A}$, reflecting the relative orientation between the transition dipoles.

Both transfers are sketched in fig. 2.4. Lacking spin–orbit coupling, dipole transitions between singlets and triplets are forbidden. Dexter transfer requires wave function overlap, limiting its range. For singlets the likelihood of Dexter and Förster transfer depends on the distance, with Dexter transfer dominating at short distances $r \lesssim 1\,\mathrm{nm}$ [65].

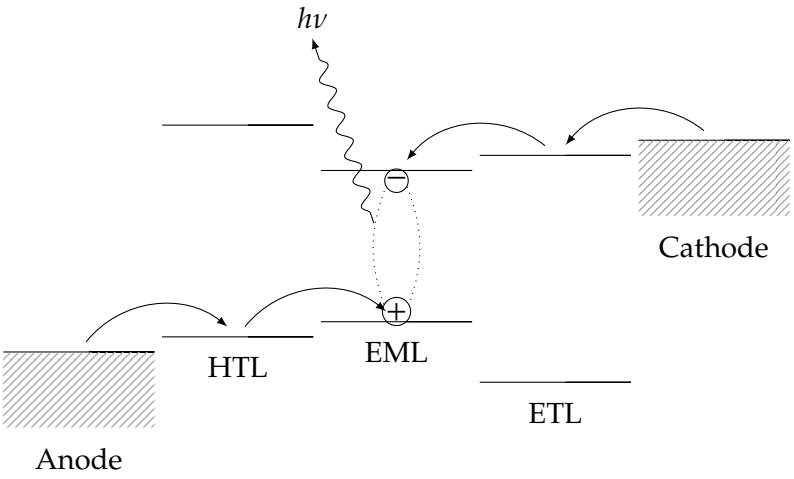

Figure 2.5: Schematic energy diagram illustrating the operation of a three-layer OLED: Electrons are injected from the cathode and travel through the electron-transport layer (ETL) towards the emissive layer (EML). Holes are injected from the anode and travel through the hole-transport layer (HTL). In the EML, hole and electron can form an exciton and recombine radiatively. Energy barriers at the EML–ETL and –HTL interfaces hinder charge carriers from passing through the EML to prevent leakage current.

2.4 ORGANIC LIGHT EMITTING DIODES (OLEDS)

In its simplest form, an OLED consists of a single-layer OSC sandwiched between electrodes. This setup was used in the discovery of electroluminescent properties of OSCs in a thin film of anthracene by Pope et al. [10] and Helfrich et al. [11].

The operation of an OLED is illustrated in fig. 2.5: Electrons and holes are injected via the cathode and anode, respectively. At operating condition, charge movement in the device follows the applied field towards the opposite electrode. If hole and electron meet, they can form an exciton. Excitons formed in the emissive region can transfer onto an emitter and decay radiatively, emitting light.

Low spin–orbit coupling of light elements most prevalent in OSCs – namely C, H, O and N – leads to long lifetimes of triplets, which increases the probability for their thermal decay or quenching via other excitons or polarons. Stochastic distribution of hole- and electron-spins

leads to 75 % triplets and 25 % singlets, limiting the internal quantum efficiency (IQE) of fluorescent emitters to 25 %. Inclusion of heavy atoms, e.g. Ir, increases spin–orbit coupling, allowing inter system crossing (ISC) and thus radiative triplet decay in these phosphorescent emitters [14, 69, 70].

To increase the efficiency of an OLED multiple layers have to be used to improve charge injection, reduce exciton quenching processes and leakage current at opposite electrodes. Such an OLED is depicted in fig. 2.5. The hole injection layer (HIL) is usually designed as a doped injection layer (DIL) to optimize hole injection by Fermi level alignment of the hole transport levels with the electrode. The hole-transport layer (HTL) transports holes injected into the HIL to one or more active regions of the OLED, the emissive layer (EML). Most EMLs consist of a host molecule acting as transport material for either hole or electron and an emitter molecule with an energy gap in the desired spectral range. If the emitter molecule doesn't act as an exciton trap, exciton blocking layers prevent excitons from escaping the EML into the transport layers. Electron injection layer (EIL) and electron-transport layer (ETL) correspond to HIL and HTL, facilitating electron injection from the cathode and transporting them into the EML [4, 71, 72].

2.5 ELECTRONIC STRUCTURE CALCULATIONS

Calculation of the Marcus-rate (eq. 2.4) requires information about quantum mechanical properties of the molecules, e.g. energy levels and molecular orbitals. These properties can be computed within the Born–Oppenheimer [73] approximation using DFT [74]. DFT is founded on the Hohenberg-Kohn theorem [75], which states that the ground state of the N-electron system is uniquely defined by the charge density $\rho(\mathbf{r})$. Thus allowing application of a variational principle $\delta E\left[\rho\right]/\delta\rho = 0$, leading to the Kohn–Sham equations [76]

$$\left(T_{\mathrm{el}}^{\mathrm{ref}} + V_{\mathrm{eN}} + \int \frac{\rho(\mathbf{r})}{|\mathbf{r}-\mathbf{r}'|} d\mathbf{r}' + V_{\mathrm{XC}}[\rho]\right) \varphi_i^{\mathrm{KS}}(\mathbf{r}) = \varepsilon_i^{\mathrm{KS}} \varphi_i^{\mathrm{KS}}(\mathbf{r}) \quad (2.13)$$

with the Kohn–Sham orbitals $\varphi_i^{\mathrm{KS}}(\mathbf{r})$ of individual electrons moving in an effective single-particle potential and orbital energies $\varepsilon_i^{\mathrm{KS}}$. The first term in brackets, $T_{\mathrm{el}}^{\mathrm{ref}}$, corresponds to the kinetic energy of the electrons in a non-interacting reference system with the same electron density as

the real system. The second term, V_{eN}, describes the potential caused by the nuclei. The third term contains the Coulomb potential of the electron due to the charge density of all electrons. The last term, $V_{\mathrm{XC}}[\rho]$, is the exchange–correlation functional, which accounts for exchange and correlation effects, e.g. the difference in kinetic energy of the real and reference system and the self-interaction of the electrons with their own contribution to the charge density. The exact form of the exchange–correlation functional is not known, requiring approximate functionals. The main functionals used throughout this work are a combination of Becke's exchange functional and Perdew's correlation functional (BP86)[77, 78] and the hybrid exchange-correlation functional (B3LYP)[79] along with a Gaussian basis set of split valence quality (def2-SVP)[80].

2.6 KINETIC MONTE-CARLO METHOD

The kinetic Monte-Carlo (kMC)[41] method is a variant of Monte-Carlo (MC) methods to simulate the temporal evolution of a system. Each kMC step starts with the system in a discrete state i at time t, which after some time Δt transitions into a different state f. If $\Delta t > \tau_{\mathrm{equilib}}$, i.e. the dwell time in the state i is longer than the relaxation time into equilibrium, the transition probabilities, $k_{if'}$, depend only on the current state i and not on the history of the system. Thus for any given state i knowledge of all $k_{if'}$ is sufficient to propagate the system. From all possible transitions into a new state f, one transition is chosen at random with a probability weighted by k_{if}. Assuming the processes to be uncorrelated Poisson processes, the probability of finding the system in the state i after a time $t + \Delta t$ is

$$P(\Delta t) = \exp\left(-\Gamma_i^{\mathrm{tot}} \Delta t\right) \tag{2.14}$$

with the total rate $\Gamma_i^{\mathrm{tot}} = \sum_{f'} k_{if'}$ of the system transitioning into any state $f \neq i$. To propagate the system in time, a dwell time for the system in state i can be drawn from the distribution of $P(\Delta t)$ as

$$\Delta t = -\frac{\ln(u')}{\Gamma_i^{\mathrm{tot}}} \tag{2.15}$$

with a random number from the uniform distribution $u' \in (0, 1]$

To simulate the temporal evolution of a system initially in state i at $t = 0$ with the kMC method,

1. calculate rates $k_{if'}$ for transitions to any state $f' \neq i$,
2. draw two uniform numbers u, $u'(0, 1]$,
3. select the transition into state f with

$$\sum_{j=0}^{f-1} k_{ij} < u\Gamma_i^{\text{tot}} \leq \sum_{j=0}^{f} k_{ij}\,, \tag{2.16}$$

4. transition the system into state f,
5. propagate the system time by $\Delta t = \ln(u')/\Gamma_i^{\text{tot}}$ (eq. 2.15) and
6. repeat until system converges into a steady-state.

3

MULTISCALE MODELLING OF ORGANIC SEMICONDUCTORS

As discussed in section 2.2, charge transport in disordered OSCs can be described as a series of hops between localized molecular states with rates approximated with the Marcus rate (eq. 2.4). With energy disorders commonly found in OSC materials employed in OLED devices, hops to a large portion of neighbouring molecules are suppressed by the Boltzmann factor in the Marcus rate equation, leading to charge transport following hopping pathways with varying resistivities. The length of these percolation pathways depends on the energy disorder and typically ranges from 10 nm to 100 nm for organic small molecules commonly used in OSCs [81–83]. These percolation pathways determine the conductance of the system. Accurate sampling of charge transport thus requires representative mesoscale systems consisting of ten-thousands to millions of sites. Input parameters of the Marcus rate equation, such as electronic couplings, site energy difference and reorganization energy, on the other hand, depend on the individual molecules and their electronic structure, which are influenced by their unique environment. Treating these diverging length scales in a single model currently is not feasible, they can be taken into account, however, with a multiscale modelling approach. This approach spans the length scales from a few angstroms at the single molecular level to several 100 nm at the device level by treating relevant effects at different length scales with individual models which are tightly coupled into the complete multiscale workflow.

The individual steps of the multiscale workflow for material and OSC device characterization are depicted in fig. 3.1. The workflow starts with single-molecule DFT calculations in vacuum to parametrize classical force fields and compute atomic partial charges (section 3.1). These parameters are used to generate atomistically resolved morphologies of $\mathcal{O}(1000)$ molecules with a MC based protocol [84] mimicking physical vapour deposition (section 3.1). For a number of molecules within this

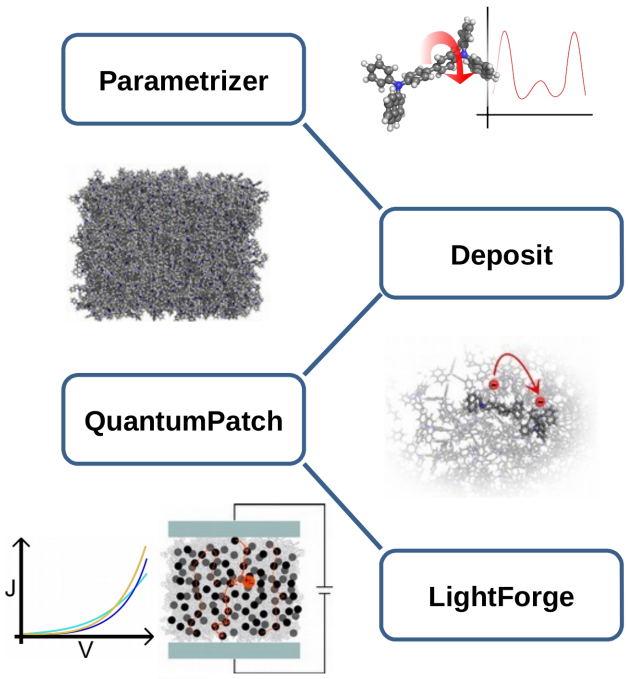

Figure 3.1: Multiscale workflow used in this work to compute material and device properties of OSCs. Taken from [A7].

morphology, parameters for the Marcus rate, i.e. electronic couplings, site energy disorder, reorganization energy, IP and EA are calculated in a self-consistent embedding-procedure using the QUANTUMPATCH (QP)[85] method (section 3.2). From these electronic structure parameters and the atomistic morphology a coarse-grained system at the device scale is created using a stochastic method developed by Baumeier et al. [86] and extended by Symalla et al. [34] (section 3.3). Finally, based on these device scale systems, OSC device operation is simulated using the kMC protocol LIGHTFORGE (LF)[34](section 3.4).

The methods of this multiscale workflow to simulate OSC device operation were initially developed by Symalla et al. [34], Neumann et al. [84], Friederich et al. [85] and Strunk et al. [87], used and improved throughout this work [A1–A10, P1, P3]. Based on these works, the following sections introduce the individual simulation methods of the multiscale workflow, while the reader is referred to literature for a more detailed discussion [88–91]. Chapter 4 benchmarks the multiscale workflow by computing material properties of a large set of different materials (section 4.1.1), as well as device characteristics of two single-

layer devices (section 4.2) and an OLED (section 4.3) *de novo*. Based on these data, section 4.1.2 investigates a method to improve ETL performance by disorder passivation. Chapter 5 extends this workflow to incorporate DILs into device simulations. Chapter 6 combines this work to simulate an experimentally validated OLED stack *de novo* on the macroscopic scale using an established DD model (section 6.3) and on the mesoscale using the kMC model (section 6.5).

3.1 MORPHOLOGY GENERATION

The multiscale modelling workflow starts with the generation of a thin-film morphology representing amorphous organic layers used in OLED devices. This work uses the MC protocol DEPOSIT [84], which mimics physical vapour deposition to generate the amorphous morphologies. Single molecules are sequentially added to the simulation box sampling the morphology surface using a MC based basin hopping approach with simulated annealing (SA). Intermolecular interactions are modelled using Lennard-Jones (LJ) potentials (parameters listed in table A.1) and Coulomb potentials based on an electrostatic potential (ESP) fit [92] of the single molecule in vacuum. To model different molecular configurations, rotations of dihedrals around single bonds are performed, while bond lengths and angles are kept fixed during deposition. The energy of each configuration is computed using molecule-specific intramolecular force fields derived by step-wise rotation of dihedral angles of single molecules in vacuum and computing DFT energies of each configuration. To improve sampling, multiple SA cycles with identical starting conditions are run in parallel, with one molecule selected based on the Metropolis-criterion [93]. Molecules are kept fixed after deposition to achieve linear scaling of computing time.

Choice of morphology size requires a trade-off between simulation time and accuracy in following methods. Typical morphologies generated in this work contain 1000 to 2000 molecules in a simulation box with a base are of 80 Å × 80 Å to 90 Å × 90 Å and periodic boundary conditions (PBC) in x- and y-direction and enough space in z-direction to fit all molecules. While $\mathcal{O}(10\,000)$ MC steps are sufficient to accurately sample the morphology surface and conformations of small molecules, accurate sampling of larger molecules with multiple dihedral-angles requires $\mathcal{O}(100\,000)$ MC steps [94]. SA starts at an artificially high temperature

with the final temperature fixed by the experimental conditions during vapour deposition, usually room temperature.

3.2 ELECTRONIC STRUCTURE CHARACTERIZATION

Modelling charge transport with Marcus-theory (section 2.2.2) requires several material parameters which are influenced by polarization effects caused by the unique environment of each molecule in the morphology. We use the QP [85] method to self-consistently take into account the unique environment of each molecule. The QP method starts by calculating the electronic ground state charge density of each molecule in vacuum using DFT and fits point charges to each atom reproducing the electrostatic potential of the molecule. In the next steps, molecular ground state charge densities are calculated in a self consistent iterative process, exposing the molecule to the point charges of surrounding molecules, until the total energies converge.

Transfer integrals J, reorganization energy λ and energetic disorder σ, as static contribution to site energy differences ΔE, as well as IP and EA for device simulations are calculated within the converged electrostatic environment. The following sections describe the calculation of the microscopic Marcus-rate parameters J, λ, IP and EA and σ.

Electronic coupling

The electronic couplings J_{if} for electron (hole) transport can be calculated from the Kohn–Sham (KS) LUMOs (HOMOs) φ following the Löwdin orthogonalization procedure [95]. The electronic couplings between the single molecules i and f are computed as [96]

$$J_{if} = \frac{H_{if} - \frac{1}{2}\left(H_{ii} + H_{ff}\right) S_{if}}{1 - S_{if}^2}, \tag{3.1}$$

with the matrix elements

$$H_{if} = \left\langle \varphi_i \middle| H_{\mathrm{KS}} \middle| \varphi_f \right\rangle \tag{3.2}$$

of the effective one-electron Hamilton operator of the dimer system H_{KS} between the LUMO (HOMO) orbitals on molecules i and f $\varphi_{i,f}$ extended to the dimer system and the wave function overlap

$$S_{if} = \langle \varphi_i | \varphi_f \rangle \,. \tag{3.3}$$

The electronic couplings J_{if}^{Dexter} for Dexter energy transport (second and third term in eq. 2.9) are approximated by [39]

$$J_{if}^{\mathrm{Dexter}} \approx \sum_{n,m} \left\langle \varphi_i^{\mathrm{H}} \middle| n \right\rangle \left\langle \varphi_f^{\mathrm{H}} \middle| n \right\rangle \langle n | H_{\mathrm{KS}} | m \rangle \left\langle m \middle| \varphi_i^{\mathrm{L}} \right\rangle \left\langle m \middle| \varphi_f^{\mathrm{L}} \right\rangle \tag{3.4}$$

with $|\varphi_i^{\mathrm{H}}\rangle$ ($|\varphi_i^{\mathrm{L}}\rangle$) the KS HOMO (LUMO) on molecule i and $\langle n|$ and $\langle m|$ representing a complete basis.

Reorganization energy

Different timescales of electronic processes and the nucleic response allow partitioning charge transfer from a donor molecule D to an acceptor molecule A into the steps illustrated in fig. 3.2: Initially D is in its relaxed charged state and A in its relaxed neutral state (I). Charge transfer, being a fast electronic process compared to the nucleic response, leaves D uncharged in the relaxed charged conformation and A charged in the relaxed uncharged conformation (II). Subsequent structure relaxation leaves D in its relaxed uncharged state and A in its relaxed charged state (III). Using Nelsen's four point procedure [97] the reorganization energy λ can be calculated by adding a charge to A and performing the relaxation $E_2 \rightarrow E_3$ and removing the charge from D and performing the relaxation $E_2' \rightarrow E_3'$, giving the reorganization energy

$$\lambda = \lambda_A - \lambda_D = (E_2 - E_3) + (E_2' - E_3') \tag{3.5}$$

Site energy disorder

As discussed in section 2.2, the density of states (DOS) in amorphous OSCs approximately follows a Gaussian distribution [43–47]. The width

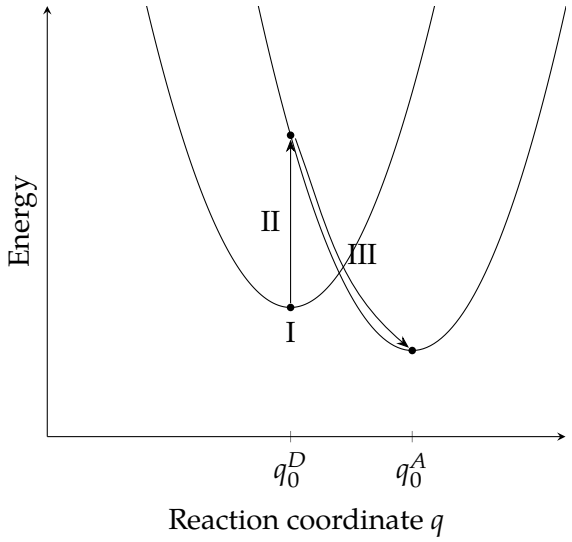

Figure 3.2: Charge transfer from donor molecule D to acceptor molecule A partitioned into three steps: Initial state (I), charge transfer from D^* to A (II) and subsequent relaxation into ground state of both D and A^* (III).

σ of this Gaussian distribution is commonly used to quantify the disorder of the system. Electrostatic interactions can induce spatial correlations of site energies causing deviations from the Gaussian disorder [98–100]. As electronic couplings J decay exponentially with distance, long range correlations between site energies have only a minor impact on hopping transport. A more reliable quantity to describe the hopping transport is therefore the local disorder

$$\sigma(\Delta E) = \sqrt{\frac{1}{2(N-1)} \sum_{i,j \neq i} \Delta E_{ij}^2} \tag{3.6}$$

with site energy differences ΔE_{ij} of only molecule pairs with non-vanishing electronic couplings and the factor 2 in the denominator to account for double counting $\Delta E_{ij} = \Delta E_{ji}$. ΔE_{ij} are approximated by the difference in KS HOMO or LUMO energies of molecules i and j.

Without spatial correlations of site energies, global and local disorder are related by

$$\sigma(E) = \frac{1}{\sqrt{2}} \sigma(\Delta E). \tag{3.7}$$

Unless otherwise noted, the local disorder $\sigma \equiv \frac{1}{\sqrt{2}}\sigma(\Delta E)$ is used throughout this work.

Site energy

Site energies for holes and electrons are taken to be the IP and EA, respectively, of the molecule in its environment. Differences in the IP and EA between molecules of different species or a species of molecules and the electrode workfunction can be up to several eV, while typical site energy disorder σ of the involved species are on the order of 100 meV. For hops between molecules of different species or charge injection and extraction at the electrode, energy barriers typically have a larger impact on ΔE than the site energy disorder σ of the involved species. IPs of molecules A are calculated as the total energy difference of the system with and without an additional hole or electron on molecule A, respectively. The IP of a molecule species is taken as the average over the IPs of a small number of molecules in their unique environment. EA is either calculated in the unique environment, as the IP, or from vacuum values using an empirical correction fitted to low-energy inverse photoemission spectroscopy (LEIPS)[101] measurements.

3.3 STOCHASTIC STRUCTURE EXPANSION

The system size for OSC device simulations is determined by the explicit layout of the device or constrained by the percolative nature of charge transport in amorphous OSCs [82]. Typical OLEDs devices have a thickness of a few 100 nm, e.g. the red OLED simulated in chapter 6. Percolation paths, which can define the conductance of a material, reach several 10 nm up to 100 nm depending on the energy disorder of the material [83]. Efficient use of computational resources restricts microscopic input to morphologies in the low 10 nm × 10 nm × 10 nm size, ΔE_{if} and J_{if} of few $\mathcal{O}(1000)$ pairs, λ, IP and EA of few molecules. We therefore use the *stochastic dominance competition model* developed by Baumeier et al. [86] to create device-scale systems from the atomistic morphology and microscopic parameters from electronic structure calculations. Points are iteratively distributed randomly in the system of given dimensions

until the target density of points is reached. A radius is drawn according to the target distribution of nearest-neighbour distances in the atomistic morphology for each point. If a point falls within the radius of another point or another point is enclosed its radius, the new point is discarded. Symalla et al. [34] refined this method by scaling the radii by a factor s that minimizes the mean squared error between target and resulting nearest-neighbour distribution.

3.4 OSC DEVICE SIMULATION

OSC devices are simulated using the kMC method discussed in section 2.6 with the LIGHTFORGE (LF)[34] package developed by Symalla et al. [34] and improved throughout this work.

In the LF package, the OSC is modelled as a network of sites representing molecules. Each site is vacant or occupied by a hole, electron or exciton. The state of the system is defined by the exact particle configuration. Particle movement, injection, extraction or exciton events transition the system into a new state. After each transition, the rates are recalculated according the new state of the system. The dynamic electrostatic potential is reevaluated after each charge movement, injection or extraction, including all charges in the system and image charges due to metallic boundary conditions if the device is bound by electrodes. Charge transport is modelled as a polaron hopping from site i to a connected site f with the Marcus-rate (eq. 2.4). The energy difference ΔE entering the Marcus-rate includes the dynamic Coulomb interaction between all charge carriers in the system

$$\phi_i^{\mathrm{dyn}} = \frac{e}{4\pi\epsilon_0\epsilon_r} \sum_j \frac{q_j}{r_{ij}}, \tag{3.8}$$

where r_{ij} is the distance between the site i and a polaron j with charge q_j inside the device. The electronic coupling J_{if} contains both the direct electronic coupling and the superexchange coupling via any of the N neighbouring sites j using first-order perturbation theory

$$J_{if} \approx J_{if,0} + \sum_{\substack{j\neq i \\ j\neq f}}^{N} \frac{J_{ij,0}J_{jf,0}}{E_{\mathrm{virt}} - E_{\mathrm{T}}} \tag{3.9}$$

with the direct electronic coupling $J_{if,0}$, E_{virt} the energy of the system in its virtual state with the charge occupying site j and the transition

state energy E_T [34]. Connectivity of a given pair of sites with distance d is determined by the probability of a pair of molecules with a center of mass (COM) distance d having a nearest atom distance of less than 7 Å. Hopping transport is possible between all connected pairs with both direct and superexchange coupling taken into account.

Depending on the simulated system, charges are either initially placed into the system or injected from the electrode. Charge injection into the system is modelled as a charge carrier hopping from a bath of charge carriers a fixed distance away from the device onto a site close to the interface. This approach assumes a smooth electrode surface, neglecting spatial inhomogeneities e.g. from the vapour deposition of the top electrode onto the OSC. The injection barrier for an electron hopping from cathode c to site i over a distance in field-direction x

$$\Delta E_{ic}^{\mathrm{IB}} = W_c - E_i - \phi_i^{\mathrm{scr}} - \phi_i^{\mathrm{dyn}} - eFx_i \tag{3.10}$$

depends on the difference between workfunction W_c and site energy E_i, modified by the electronic screening $\phi_i^{\mathrm{scr}} = -e^2(16\pi\epsilon_0\epsilon_r x_i)^{-1}$ due to the electrostatic boundary conditions at the electrode, dynamic electrostatic potentials from other charges in the system ϕ_i^{dyn} and the applied field F. Electron injection and extraction rates for a hop from cathode c to site i and vice versa are computed with the MA rate eq. 2.1

$$k_{ic} = \frac{\pi}{2\hbar k_{\mathrm{B}} T} |J_{ic}|^2 \begin{cases} \exp\left(-\frac{\Delta E_{ic}^{\mathrm{IB}}}{k_{\mathrm{B}} T}\right), & \text{for } \Delta E_{ic}^{\mathrm{IB}} > 0 \\ 1, & \text{otherwise}, \end{cases} \tag{3.11}$$

with the prefactor approximated as $\omega_0 = {}^{\pi}/_{2k_{\mathrm{B}}T}$ [91] and the injection barrier ΔE_{ij} given by eq. 3.10. Compared to the Marcus-rate eq. 2.4, the MA rate doesn't incur a penalty for hops downward in energy, factoring in the ability of the metal to dissipate continuous amounts of energy. The hole injection barrier and hole injection and extraction at the anode is treated analogously.

Exciton formation via charge recombination is modelled as a charge carrier hopping onto a site occupied by a charge carrier of opposite sign with a rate according to eq. 2.4. In case of a hole hopping from site i to a site f occupied by an electron, the energy difference is

$$\begin{aligned} \Delta E_{if}^{\mathrm{rec}} &= \Delta E_i + \Delta E_f + \Delta E_{\mathrm{coul}} \\ &= \left|E_f^{\mathrm{EA}}\right| - \left|E_i^{\mathrm{IP}}\right| + \left|E_f^*\right| + \Delta E_{\mathrm{ext}} + \Delta E_{\mathrm{coul}} \end{aligned} \tag{3.12}$$

obtained by separating the energy difference into the total energy differences of each site $\Delta E_{i/f}$ and the coulomb interaction of the separated electron hole pair ΔE_{coul}, where E_i^{IP} is the IP of site i, E_f^{EA} the EA of site f, E_f^* is the excitation binding energy of site f and ΔE_{ext} the change in energy due to the applied field. Upon formation, multiplicity is assigned stochastically, i.e. 25 % of created excitons are singlets, 75 % triplets.

Exciton separation is treated as the reverse process of charge recombination (eq. 3.12) with

$$\Delta E_{if}^{\text{sep}} = -\Delta E_{fi}^{\text{rec}}\,, \tag{3.13}$$

i.e. exciton separation is possible if the energy gain of the charges localized on sites i and f, compared to the exciton localized on molecule i or f, is large enough to overcome the exciton binding energy.

Exciton transport is modelled via Förster and Dexter electron transfer discussed in section 2.3. Both Förster and Dexter rates can be computed from QP calculations based on Marcus-theory (eq. 2.4) with couplings computed according to eq. 2.12 and eq. 3.4, respectively [39].

Exciton quenching is modelled as either an exciton transfer to a site occupied by an exciton or a polaron transfer to a site occupied by an exciton and vice-versa. As with the exciton transfer, the exciton quenching rates can be computed from QP calculations [39]. Due to their longer lifetime, quenching processes involving triplets are the predominant quenching processes. The rate for a triplet energy transfer from site i to a site f excited with a triplet, i.e. a triplet–triplet annihilation (TTA) process,

$$k_{if}^{\text{TTA}} = \sum_{n=1} k_{if}\left(\Delta E_n^{\text{TTA}}\right) \tag{3.14}$$

is a sum over all TTA acceptor states T_n on site f computed above with the energy difference

$$\Delta E_n^{\text{TTA}} = \left(E_f^{\mathrm{T}_n} - E_f^{\mathrm{T}_1}\right) - \left(E_i^{\mathrm{S}_0} - E_i^{\mathrm{T}_1}\right). \tag{3.15}$$

Energy transfer to a polaron is split into a process based on Förster-transfer (triplet–polaron quenching (TPQ)) with a rate analogous to eq. 3.14 with

$$\Delta E_n^{\text{TPQ}} = \left(E_f^{\mathrm{D}_n} - E_f^{\mathrm{D}_0}\right) - \left(E_i^{\mathrm{S}_0} - E_i^{\mathrm{T}_1}\right). \tag{3.16}$$

and a process based on charge transfer (polaron–triplet quenching (PTQ)) with a rate approximated by the charge transfer rate (eq. 2.4). Quenching rates involving singlets are computed accordingly.

Radiative and thermal decay are modelled as stochastic decay with given rates for singlets and triplets. Energy transfer from exciton to another particle leads to the quenching of the exciton and excitation of the particle. In case of Dexter transfer this can also lead to triplet–triplet fusion (TTF), promoting the triplet to a singlet. The excited particle is assumed to decay fast into the ground state compared to other processes in the system.

Doping activation is treated as charge transfer from the dopant to the host. Activation of a dopant site is modelled as an S_0-exciton on the dopant site i separating according to eq. 3.13 with $\Delta E_{if}^{\text{act}} = \Delta E_{if}^{\text{sep}}(E^* = 0\,\text{eV})$.

4

MODELLING CHARGE AND EXCITON TRANSPORT THROUGH OSC LAYERS AND DEVICES

As discussed in the previous chapters, performance of OSC devices is determined by an entangled interplay of a multitude of microscopic processes, ranging from charge injection over charge transport to exciton formation, radiative decay and quenching processes. Many of these processes are either directly or indirectly impacted by the charge carrier balance within the device, e.g. the transport rates, which are modified by the Coulomb interaction altering the energy landscape or polaron-quenching enabled simply by the presence of charges in the vicinity of excitons. Tuning charge carrier balance can therefore have a large influence on device performance. Since charge carrier balance is determined mainly by the transport properties of the OSC materials, finding improved materials via molecular design poses a viable option for optimizing charge carrier balance and thereby device performance.

Molecular design is currently mostly lead by intuition and trial and error, turning into a time- and resource-intensive endeavour if pursued via experiment alone. Computer simulations can aid experimental research and development (R&D) towards balanced devices via molecular design, enabling the comparatively efficient identification of materials for a specific purpose, or rational design of novel compounds with targeted properties, and thus hold the potential to boost OLED development [29, 102, 103].

However, for computer simulations to be of relevance for molecular design, it is crucial to have accurate models that predict charge transport properties of OSCs from first principles. The *de novo* workflow discussed in chapter 3 has been used successfully as an accurate model for charge transport of OSCs in specific applications, e.g. for the computation of charge carrier mobility using a closed analytic expression [104] or the kMC model in a single mixed system [34].

This chapter builds on prior work to provide improved methods for accurate computations of charge transport in a broad range of OSC devices. The computations of charge carrier mobility in section 4.1.1, charge transport in section 4.2 and device characteristics in section 4.3 using these improved methods serve two purposes: namely a) as isolated benchmarks of the charge transport model to provide a solid foundation for the simulation of full OLED stacks and b) to demonstrate that material properties can be accurately predicted for efficient screening of molecular candidates in the design of compounds with desired properties, to focus experimental efforts to validate performance of most promising candidates. Additionally, section 4.1.2 uses the multiscale workflow to develop a simple scheme for improving electron mobility, allowing in turn to tune charge carrier balance within the device, which is currently awaiting experimental validation.

4.1 MODELLING AND TUNING CHARGE CARRIER MOBILITY

The study presented in this section was published as [A6, A7] and presented as [P2].

One limiting property of amorphous OSCs is the charge carrier mobility, which is several orders of magnitude below values for inorganic semiconductors [104]. The fundamental reason for this shortcoming, as discussed in section 2.2, is the localization of electrons on individual molecules in the amorphous films due to the disorder of molecular electronic states. In the past three decades, intense research focused on developing materials with improved properties, including increased mobility. This research, however, was mainly lead by chemical intuition and experimental synthesis and device fabrication, limiting the progress in the exploration of the vast molecular space. On the other hand, improvements in theoretical and computational methods in OSCs have lead to these methods becoming an indispensable tool in material development and characterisation. A further increase of the accuracy, especially in mobility prediction methods, could boost virtual design, enabling researchers to focus experimental efforts in the material development process to promising candidates identified in computer simulations [29].

Seminal work by Bässler [44] quantitatively showed the crucial dependence of charge carrier mobility on the inter-molecular disorder of electronic states. Assuming a Gaussian distribution of electronic states with width σ, he found a strong dependence of the charge carrier mobility on σ of

$$\mu \propto exp\left[-\left(\frac{2}{3}\frac{\sigma}{k_B T}\right)^2\right]. \tag{4.1}$$

Consequently, any *de novo* mobility model requires information about the distribution of the polaron energy levels in the unique molecular environment in the amorphous film. While these quantities can only be accurately calculated in very small systems of $\mathcal{O}(100)$ molecules, the percolative nature of charge transport in OSCs demands a description on the $\mathcal{O}(100\,\mathrm{nm})$ scale comprising of $\mathcal{O}(1\,000\,000)$ molecules [83].

In prior work Friederich et al. [104] calculated charge carrier mobility with a closed analytic expression, derived by averaging over all intermolecular hops, assuming homogeneous charge transport and thus neglecting percolative effects [105]. In this work the zero-field mobility of hole transport for a set of materials commonly used in OSCs [104] was computed within approximately one order of magnitude agreement with experimental data. However, this approach is limited to pristine systems with a Gaussian distribution of states, does not take into account charge carrier interaction and is not suitable to predict the field-dependence of the mobility. Using the complete multiscale workflow discussed in section 3.4 improves the accuracy of the mobility prediction by explicitly modelling the charge transport process on a microscopic basis including charge carrier interactions, and therefore allows for a deeper insight into the charge transport characteristics of OSC devices.

Section 4.1.1 benchmarks this improved *de novo* multiscale workflow by computing the charge carrier mobility of 16 materials commonly used in OSCs solely on the basis of their molecular structure. The computed zero-field and field-dependent mobilities are in good agreement with experimental data, proving this approach to be an effective virtual design tool for OSC materials and devices.

Section 4.1.2 presents a design approach to tune the electron mobility of electron transport materials by targeted modification of the electrostatic environment in OSC thin films, by mixing a transport material with a

secondary material which is inert to electron transport. This approach is shown to be capable of increasing electron mobility in the prototypical electron transport material 1,3,5-tris(*N*-phenylbenzimidazol-2-yl)benzene (TPBi) by one order of magnitude.

4.1.1 *Computing charge carrier mobility*

While closed analytic expressions can yield good estimates of the zero-field mobilities [104], they take the amorphous morphology of the OSC into account only via molecule-specific parameters. Coarse grained approaches [32, 37, 86], on the other hand, use mesoscale representations of organic thin films to model charge transport. Solving the Pauli Master-equation for charge carriers in the system allows the calculation of the mobility, takes electron–electron interaction into account on a mean-field level and allows for arbitrary distributions of states. This method has been effectively applied to study behaviour of charge carrier mobility in realistic OSC materials [37, 38]. This approach does not take into account many-particle effects beyond the mean-field, limiting its accuracy [106–109]. This section uses the kMC model to compute the charge transport at the mesoscopic scale, based entirely on *ab initio* input. This method is numerically demanding, but can be extended to simulate mixed films, interfaces or devices with ohmic injection at small applied voltages or medium to large charge carrier concentrations [34, 107, 109].

Apart from the choice of the model to solve the transport problem, the prediction quality of the computed mobility strongly depends on the accuracy of the computed material properties, like disorder, which are highly sensitive to both details of the protocol to compute electronic structure of molecules in thin films and the underlying morphology. In contrast to the previous approach by Friederich et al. [104], this study uses a protocol mimicking physical vapour deposition to generate morphologies with atomistic resolution (section 3.1). As the systems which are generated in this way are too small to be used in the kMC transport model [83], the stochastic expansion scheme (section 3.3) is used to generate mesoscopic structures.

Clearly the complex interplay of these methods calls for a thorough benchmark of the method. This benchmark is all the more important,

because bottom-up device calculations based on *ab initio* input cannot be performed with continuum models, but are – ideally – conducted by kMC calculations. Such calculations would fail if the electronic structure of the individual materials are not correctly represented. To ensure the quality of the single materials model, this workflow is used to compute both zero-field and field-dependent mobility without the need for experimental input for a wide range of materials commonly applied in electron or hole transport layers or as host materials in emission layers. With only the molecular structure as input, the computed zero-field and field-dependent mobilities show a significantly improved agreement between simulation and experiment.

To compute the charge-carrier mobility *de novo*, the multiscale approach detailed in chapter 3 is used. All DFT calculations are performed using the TURBOMOLE [110] DFT package with the B3LYP functional and def2-SVP bases unless noted otherwise.

To obtain representative atomistic models of the amorphous thin-film for each material, 2000 molecules are deposited into a simulation box of 90 Å × 90 Å × 360 Å with 32 parallel SA cycles starting at an artificially high temperature (4000 K) and cooling to room temperature (300 K) in 130 000 MC steps, providing sufficient sampling for the molecules studied here [94]. Intermolecular interactions during the deposition process are modelled using the LJ parameters of the DEPOSIT standard force field (parameters listed in table A.1) and Coulomb potentials based on ESP charges.

Orbital energy differences ΔE_{ij}, electronic couplings J_{ij} and reorganization energies λ are calculated for a subset of molecules in their converged unique electrostatic environments in the thin-film morphologies. Using the equilibrated orbital energies of the innermost 200 molecules, the energy disorder σ is calculated from the standard deviation of energy differences ΔE_{ij} of all pairs of neighbouring molecules i and j. In the converged system, the electronic couplings J_{ij} of a molecule i to its respective neighbour j are calculated for pairs of the innermost 150 molecules with an atom–atom distance of less than 7 Å. Dimer DFT calculations are performed using the BP86 functional and def2-SVP basis set. Reorganization energies λ_i are calculated for eleven core molecules in their unique environment. The geometry of the charged and uncharged molecules are optimized within constraints imposed by their

environments. Constraints are implemented by placing effective core potentials (ECP) at the position of atoms of neighbouring molecules.

To accurately model charge transport in these amorphous OSCs, the deposited thin films are expanded into an amorphous structure of 40 nm × 40 nm × 40 nm. In this expanded amorphous structure, on-site energies are drawn following the Gaussian distributions of ΔE_{ij} obtained from the electronic structure calculations. Electronic coupling elements J_{ij} for site i and one of its neighbours j are drawn from the microscopic distribution $J(r)$ within the small interval dr around the distance r_{ij} between both sites. Reorganization energies are taken to follow a Gaussian distribution.

To model mobility measurements in the bulk of an OSC, charge transport is simulated with a charge carrier density of 1×10^{-3} per site in an amorphous system of 40 nm × 40 nm × 40 nm with periodic boundary conditions in x-, y- and z-direction. To account for stochastics in morphology expansion and site energy distribution, 10 different configurations are sampled per applied field. Connectivity of a given pair of sites with distance d is determined by the probability of a pair of molecules with a COM distance d having a nearest atom distance of less than 7 Å . Hopping transport is possible between all connected pairs with both direct and superexchange coupling taken into account. Coulomb interactions with the nearest periodic copy of all other charges are treated explicitly, resulting in an effective cutoff of half the system size. Convergence is reached if the current density is constant over two thirds of the simulation. Charge carrier mobility is computed from the average drift velocity of charge carriers in the converged part of the simulation.

I apply the presented workflow to calculate the mobilities of the materials shown in fig. 4.1, namely the hole-transport materials *N*,*N*′-di(biphenyl-3-yl)-*N*,*N*′-diphenyl-[1,1′-biphenyl]-4,4′-diamine (*m*-BPD), *N*,*N*′-di(biphenyl-2-yl)-*N*,*N*′-diphenyl-[1,1′-biphenyl]-4,4′-diamine (*o*-BPD), *N*,*N*′-di(biphenyl-4-yl)-*N*,*N*′-diphenyl-[1,1′-biphenyl]-4,4′-diamine (*p*-BPD), 1,1-bis-(4,4′-diethylaminophenyl)-4,4-diphenyl-1,3-butadiene (DEPB), *N*,*N*′-bis(1-naphthalenyl)-*N*,*N*′-diphenyl-4,4′-phenyldiamine (NNP), *N*,*N*′-di(1-naphthyl)-*N*,*N*′-diphenylbenzidine (NPB), 2,2′,7,7′-tetrakis(*N*,*N*-diphenylamine)-9,9′-spirobifluorene (spiroTAD), di-[4--(*N*,*N*-ditolyl-amino)phenyl]cyclohexane (TAPC), 4,4′,4′′-tris(*N*-carbazolyl)triphenylamine (TCTA), *N*,*N*′-Diphenyl-*N*,*N*′-di(3-tolyl)benzi-

dine (TPD), and 5,10,15-triphenyl-5*H*-diindolo[3,2-a:3′,2′-c]carbazole (TPDI), electron-transport materials 2,9-Dimethyl-4,7-diphenyl-1,10-phenanthroline (BCP), 2-(4-biphenylyl)-5-(4-tert-butylphenyl)-1,3,4-oxadiazole (BPBD), TPBi and 1,3,5-tri(*p*-pyrid-3-yl-phenyl)benzene (TpPyPB) and both hole- and electron transport material tris(8-hydroxyquinoline)-aluminum (Alq3) at low fields. From these field-dependent mobilities the zero-field mobilities are extrapolated.

To compare the field dependence of computed and measured mobilities, experimental works featuring field-dependent mobilities are considered as references. For materials with more than one reference, mobilities measured using the time-of-flight (ToF) technique[111, 112] are preferred over mobilities fitted to the space-charge limited current (SCLC)[113, 114] due to issues in fabrication, measurement and analysis reported by Blakesley et al. [115]. If multiple ToF measurements are available, the ones featuring the highest mobility are used, as these are expected to be the most well-prepared films with least impurities. Following this selection process, measured field-dependent mobilities reported by Naka et al. [116] ($Alq3_p$), Liu et al. [117] ($Alq3_n$ and BCP), Hung et al. [118] (TPBi), Kawabe et al. [119] (BPBD), Mori et al. [120] (DEPB and TPD), Okumoto et al. [121] (*m*-, *o*- and *p*-BPD), Borsenberger et al. [122] (NNP), Bach et al. [123] (spiroTAD), Noh et al. [124] (TCTA), Naka et al. [125] (NPB), Su et al. [126] (TpPyPB), Huh et al. [127] (TPDI) and Borsenberger et al. [128] (TAPC) are taken as reference for simulated mobilities. The mobility of BPBD was fitted to the emission response from a bilayer TPD–BPBD stack, the mobility of TPDI was fitted to the SCLC. All other mobilities were measured in pure devices using the ToF technique. Mobilities predicted by theoretical multiscale models reported by Friederich et al. [104] ($Alq3_p$, DEPB, *m*-BPD, NNP, NPB, TPD), Kordt et al. [32] (BCP and NPB, Massé et al. [37] (TCTA and NPB), Kotadiya et al. [38] (spiroTAD, TCTA and NPB), Evans et al. [129] (*m*-, *o*- and *p*-BPD, TCTA, NPB and TPD), Fuchs et al. [130] ($Alq3_p$ and $Alq3_n$; field-dependent) and Aydin et al. [131] (NPB, TPD and TAPC; field-dependent) are used to assess the presented workflow. Where required, zero-field mobilities are extrapolated from field-dependent mobilities.

The disorder width σ, $\langle J^2 r^2 \rangle$ and λ are measures for the disorder, electronic couplings and the reorganization energy respectively, which mainly determine the transport properties. Table 4.1 lists these values for each molecule calculated with our multiscale workflow along with

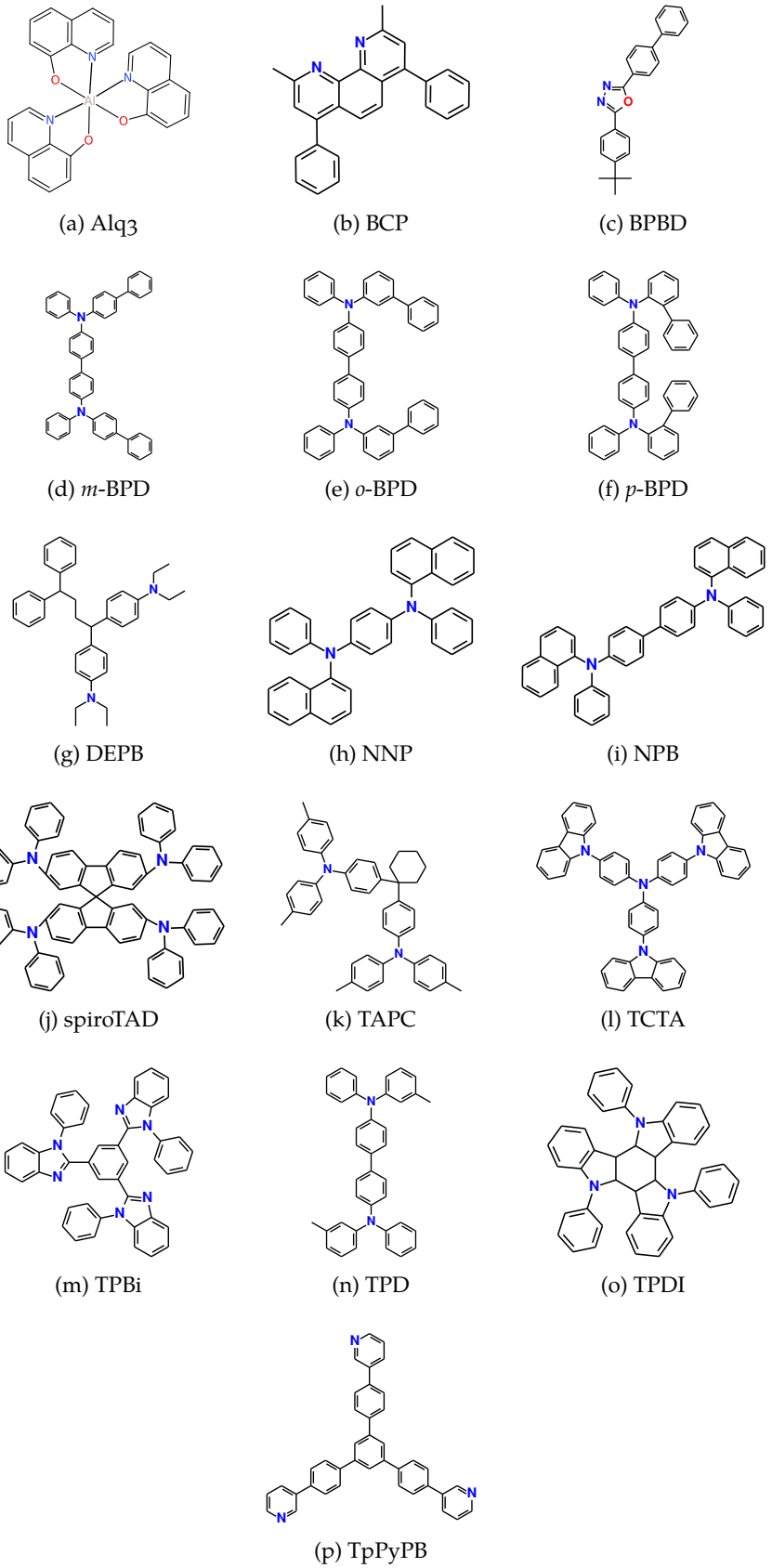

(a) Alq3 (b) BCP (c) BPBD

(d) *m*-BPD (e) *o*-BPD (f) *p*-BPD

(g) DEPB (h) NNP (i) NPB

(j) spiroTAD (k) TAPC (l) TCTA

(m) TPBi (n) TPD (o) TPDI

(p) TpPyPB

Figure 4.1: Structures of the molecules characterized in this section.

zero-field mobilities extrapolated from field-dependent mobilities simulated with our kMC model and reported from experiment and theory. The distribution of energy differences ΔE_{ij}, depicted in fig. 4.2 along with the fitted Gaussian distribution of width σ for two molecules, namely *m*-BPD and TPD (see fig. A.1 for the remaining molecules), strongly influences the mobility. With comparable $\langle J^2 r^2 \rangle$ and λ, but a 38 % higher σ, the simulated zero-field mobility of *m*-BPD lies a factor of 65 below that of TPD. The distribution of electronic couplings for two molecules, namely *m*-BPD and Alq3 (see fig. A.2 for the remaining molecules), are shown in fig. 4.3 for comparison. Alq3, without any dihedral angles, is rigid in our deposition scheme, resulting in densely packed structures and a narrow distribution of J_{ij} which decays fast with the neighbour distance, while more extended and flexible molecules, e.g. *m*-BPD, show a broader distribution of electronic couplings which decay slower with the neighbour distance. These differences are reflected in the values of $\langle J^2 r^2 \rangle$ which for these molecules differ by almost one order of magnitude between both molecules. With the electronic couplings J_{ij} only entering as a prefactor in the Marcus-rate (eq. 2.4) and σ in the exponent, differences in σ have a far larger impact on the mobility than differences in electronic couplings J_{ij}, as is evident e.g. by comparing Alq3 and TPBi electron mobilities or both *p*-BPD and TAPC mobilities ranking among the highest three despite their average electronic couplings ranking among the lowest. The environment inhibits the full structure relaxation of a molecule after charge transfer, leading to λ well between *in vacuo* calculations with calculations in the solid phase with constrained dihedral angles to inhibit large-scale conformational changes (frozen dihedral approximation) [104].

Figure 4.4 shows the zero-field mobility obtained with the kMC model compared to data from experiment and prior work by Friederich et al. [104]. As can be seen, the kMC zero-field mobilities are in very good agreement with the experimental data. With the exception of Alq3, all mobilities lie within 50 % of the experimental data and fully reproduce the experimental trends. Going beyond the Gaussian disorder model to a more accurate description of the local distribution of energy levels, as described below, not only recovers the order of mobility for BCP and NNP, but also reproduces experimental mobility within a few percent for both materials. The systematic overestimation of Alq3 hole and electron mobility can be attributed to our approximation that the Al-complex stays rigid during deposition, which leads to an underestimation of the disorder. The zero-field mobilities obtained in prior

Table 4.1: Electronic properties, namely energetic disorder, mean electronic coupling and reorganization energy, computed with the QuantumPatch method and zero-field mobilities simulated with our kMC model. Experimental zero-fields mobilities reported in literature are listed for comparison.

Molecule	σ/meV	$\langle J^2 r^2 \rangle$/eV^2 Å^2	λ/meV	μ_0/cm^2 V^{-1} s^{-1}	
				kMC	Experiment
$Alq3_p$	199	1.0×10^{-2}	195	2.6×10^{-9}	5.7×10^{-10} [a]
$Alq3_n$	182	8.6×10^{-3}	215	1.7×10^{-7}	7.4×10^{-8} [b]
$TPBi_n$	157	2.5×10^{-3}	317	4.3×10^{-7}	4.7×10^{-7} [c]
$BPBD_n$	182	5.2×10^{-3}	291	3.6×10^{-6}	1.3×10^{-6} [d]
$DEPB_p$	133	2.4×10^{-3}	316	6.0×10^{-6}	1.2×10^{-5} [e]
m-BPD_p	132	1.6×10^{-3}	210	8.8×10^{-6}	1.5×10^{-5} [f]
BCP_n	136	3.2×10^{-3}	314	1.4×10^{-5}	3.1×10^{-5} [b]
NNP_p	124	1.6×10^{-3}	281	1.2×10^{-5}	3.9×10^{-5} [g]
$spiroTAD_p$	105	1.7×10^{-3}	139	8.7×10^{-5}	1.5×10^{-4} [h]
$TCTA_p$	107	1.7×10^{-3}	206	1.3×10^{-4}	1.8×10^{-4} [i]
NPB_p	104	1.4×10^{-3}	205	1.8×10^{-4}	2.9×10^{-4} [j]
o-BPD_p	96	1.8×10^{-3}	213	3.2×10^{-4}	4.4×10^{-4} [f]
$TpPyPB_n$	123	6.4×10^{-3}	200	3.0×10^{-4}	6.5×10^{-4} [k]
TPD_p	93	1.7×10^{-3}	208	7.9×10^{-4}	6.7×10^{-4} [e]
p-BPD_p	94	1.3×10^{-3}	173	7.0×10^{-4}	7.2×10^{-4} [f]
$TPDI_p$	82	4.8×10^{-3}	145	1.0×10^{-3}	2.3×10^{-3} [l]
$TAPC_p$	74	1.4×10^{-3}	89	4.6×10^{-3}	5.6×10^{-3} [m]

[a] Naka et al. [116]
[b] Liu et al. [117]
[c] Hung et al. [118]
[d] Kawabe et al. [119]
[e] Mori et al. [120]
[f] Okumoto et al. [121]
[g] Borsenberger et al. [122]
[h] Bach et al. [123]
[i] Noh et al. [124]
[j] Naka et al. [125]
[k] Su et al. [126]
[l] Huh et al. [127]
[m] Borsenberger et al. [128]

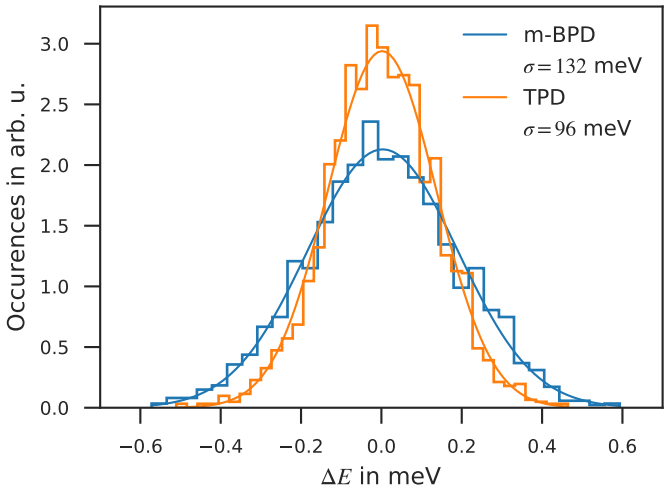

Figure 4.2: Distribution of ionization potential energy differences computed with the QuantumPatch method for *m*-BPD and TPD along with the fitted Gaussian distribution yielding the energetic disorder σ.

work, lie within two orders of magnitude above and one order of magnitude below the experimental zero-field mobilities with a slight trend of overestimating the experimental data.

While zero-field mobility is a readily accessible descriptor when optimizing or searching for new candidate molecules [29], the performance of the material in a device is determined by the charge carrier mobility at fields relevant for the specific application. Figure 4.5 shows field-dependent mobilities computed with our kMC model for a subset of materials (see figs. 4.8 and A.3 for the other materials) and experimental mobilities reported in literature [116–118, 121, 124–126, 128] for comparison. As can be seen, the field-dependence predicted by the kMC model matches the experimental data over a wide range of fields. Considering only charge carrier mobility at zero field BCP is a far better electron conductor than TPBi, while the mobilities get closer at relevant fields due to the strong field-dependence of TPBi, with the mobility of TPBi eventually surpassing that of BCP at large fields. Alq3, as a hole-transport material, shows an equally strong field-dependence, stronger than that of e.g. TAPC, TPD or TCTA, the five orders of magnitude difference in their zero-field mobilities still lead to Alq3 being the inferior hole-transport material at relevant fields. It is interesting to note that our model successfully captures differences in charge carrier mobility due to small molecular modifications as with the three isomers

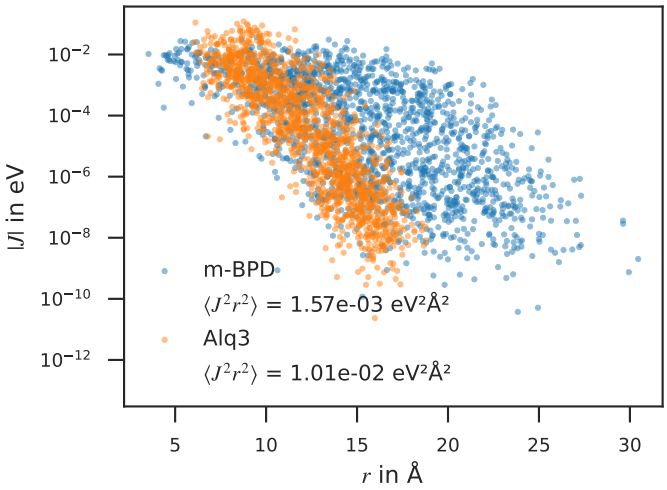

Figure 4.3: Distribution of electronic couplings J of *m*-BPD and Alq3 computed with the QuantumPatch method.

m-, *o*- and *p*-BPD (fig. 4.6, top panel). While the simulation slightly underestimates the field-dependence of *m*-BPD and overestimates the difference between *o*- and *p*-BPD in this field range, it captures both the general trends and individual ordering of the three isomers.

Figure 4.7 shows a comparison of field-dependent mobilities computed with *ab initio* multiscale workflows reported here and in literature [130, 131] along with experimental data [116, 125, 128]. Field-dependent mobilities of TAPC, TPD and NPB simulated with our kMC model show a better agreement with experiment than the model by Aydin et al. [131] despite both works using a kMC model for charge-transport simulations with comparable values for energetic disorder (table 4.2). The Master-equation model by Fuchs et al. [130] underestimates the Alq3 mobility by approximately the same factor our kMC model overestimates it.

The coarse graining approach applied to generate mesoscale systems draws random site energies from a Gaussian density of states. This approach neglects local effects of the electronic structure, i.e. the shift of energy levels induced by the relative position and orientation of neighbouring molecules. To estimate the impact of this approximation, specific energy level shifts of all molecules in the atomistic morphology are computed based on partial charges of their neighbouring molecules derived from DFT. Expanded morphologies are then generated by periodic expansion of the deposited morphologies in x- and y-direction,

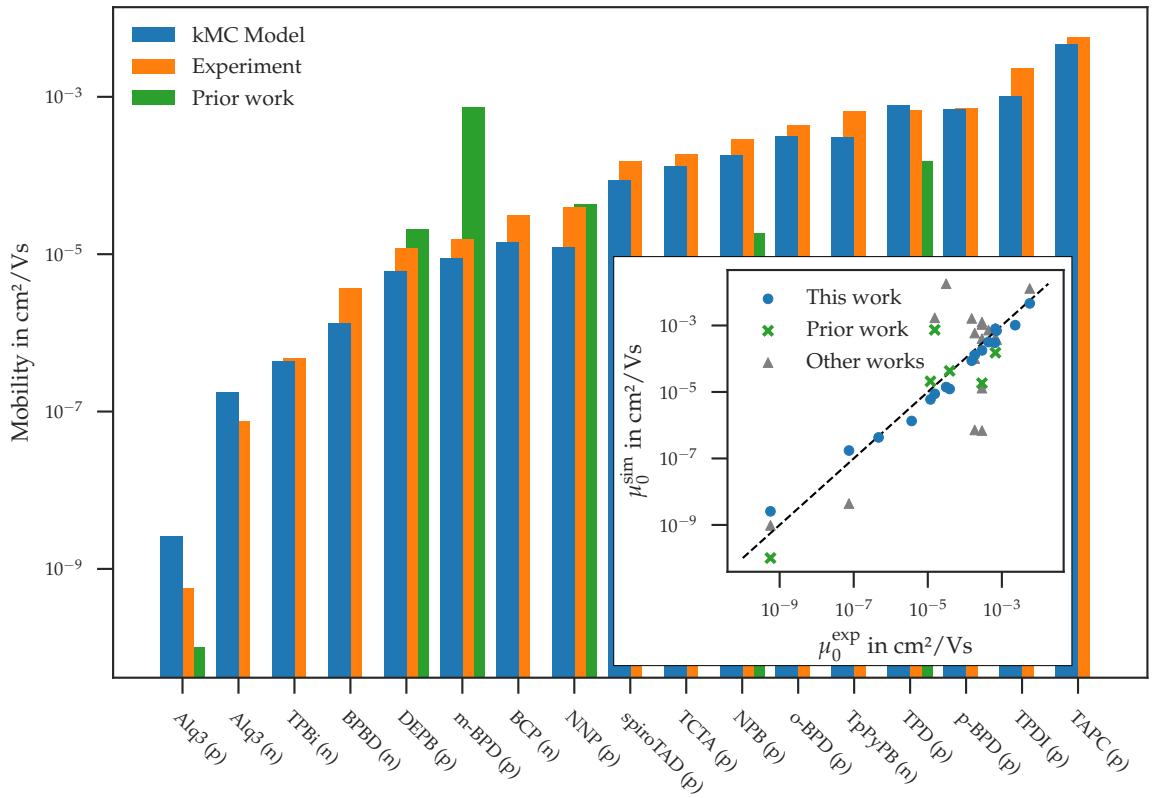

Figure 4.4: Zero-field mobilities of both hole- and electron transport materials calculated with the presented kMC model compared to experimental data [116–118, 121, 124–126, 128] and prior work by Friederich et al. [104] where available. Inset: Comparison of zero-field mobilities computed in this work (blue circle), prior work (green cross) and reported in literature [32, 37, 38, 129] (grey triangle) with experimental data. Linear relationship between simulation and experiment is shown by the black dashed line.

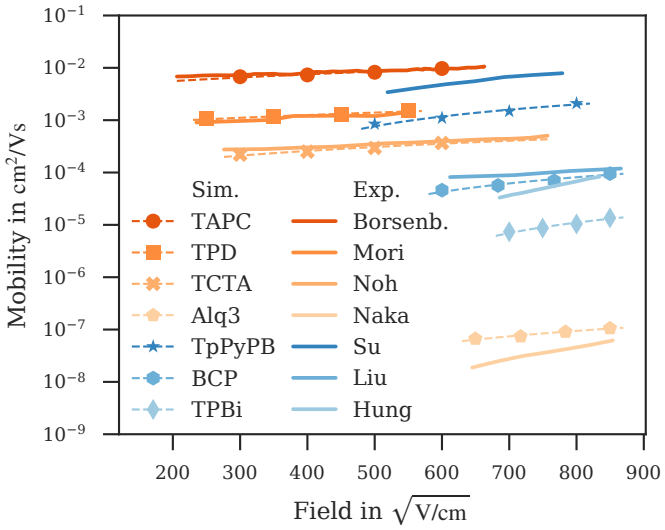

Figure 4.5: Computed field-dependent hole mobilities (orange) of TAPC [128], TPD [120], TCTA [124] and Alq3 [116] and electron mobilities (blue) of TpPyPB [126], BCP [117] and TPBi [118] compared to experimental data reported in literature. Both the magnitude and field-dependence of the simulated mobilities agree well with experimental data. Dashed lines are fitted to Poole–Frenkel behaviour $\ln(\mu) \propto \gamma E^{1/2}$ [132, 133], simulation errors are of the order of symbol size.

Table 4.2: Electronic properties and field-dependent mobilities computed with *ab initio* multiscale workflows reported here and in literature.

Molecule	σ/meV	λ/meV	μ/cm^2 V^{-1} s^{-1}	μ_0/cm^2 V^{-1} s^{-1}	Source
$Alq3_p$	199	195	6.3×10^{-8} m*	2.6×10^{-9}	SK
	201	467	1.2×10^{-8} m	9.7×10^{-10}	AF
$Alq3_n$	182	215	2.3×10^{-6} h*	1.7×10^{-7}	SK
	178	501	5.5×10^{-6} h	4.4×10^{-9}	AF
NPB_p	104	205	3.3×10^{-4} l	1.8×10^{-4}	SK
	107	286	4.4×10^{-3} l*	4.0×10^{-3}	GA
TPD_p	96	208	9.3×10^{-4} l	5.7×10^{-4}	SK
	103	273	5.6×10^{-3} l*	5.4×10^{-3}	GA
$TAPC_p$	74	89	7.3×10^{-3} l	4.6×10^{-3}	SK
	70	174	1.3×10^{-2} l*	1.3×10^{-2}	GA

SK This work AF A. Fuchs et al. [130] GA G. Aydin et al. [131] l at 400 $\sqrt{\text{V/cm}}$
m at 632 $\sqrt{\text{V/cm}}$ h at 895 $\sqrt{\text{V/cm}}$ * interpolated

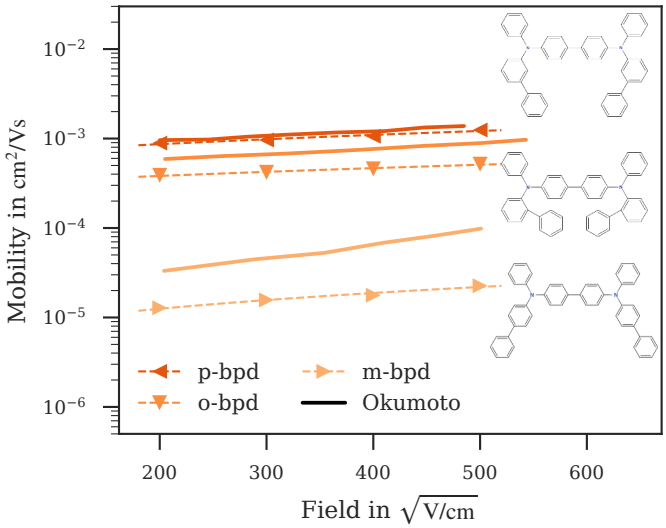

Figure 4.6: Computed field-dependent mobilities for the *m*-, *o*- and *p*-BPD isomers compared to experimental data reported by Okumoto et al. [121]. The presented workflow captures the difference in mobility due to the small modifications in the three isomers (the inset shows their respective structures). Dashed lines are fitted to Poole–Frenkel behaviour, simulation errors are of the order of symbol size.

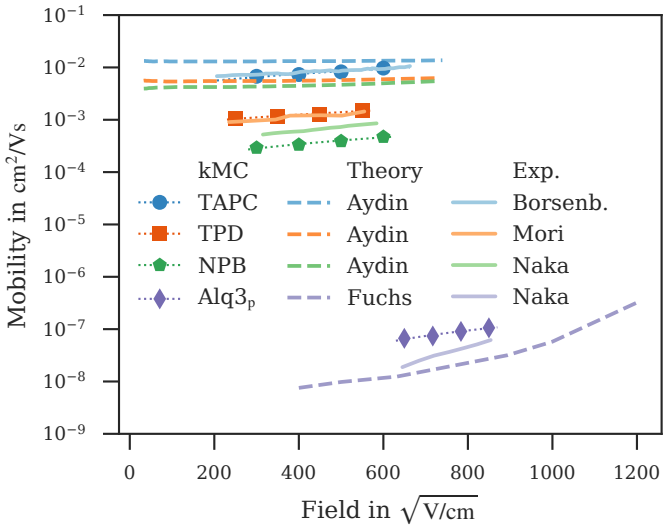

Figure 4.7: Comparison of field-dependent mobilities computed with *ab initio* multiscale models reported in this work (symbol) and literature [130, 131] (dashed line) with experiment [116, 125, 128] (solid line). Dotted lines are fitted to Poole–Frenkel behaviour, simulation errors are of the order of symbol size.

resulting in cubic structures with approx. 20 000 sites. Charge carrier density is kept constant at approx. 1×10^{-3} per site for comparability.

Field-dependent mobilities obtained with both the Gaussian disorder and this energy landscape derived explicitly from local electrostatics compared with experiment are displayed in fig. 4.8 for NPB, NNP and BCP, for which simulations using the Gaussian disorder model lead to an underestimation of charge carrier mobility. These results indicate that taking into account the local electrostatic effects within the atomistic morphology can have a strong impact on charge carrier mobility. In the case of NPB, NNP and BCP, it lead to an improved fit to experiment. Notably, a similar improvement is not observed for all materials. The advanced approach to include local effects in the electronic structure limits the system size to the size of the atomistic morphologies. This statistical limitation may lead to a large fluctuation of mobility between deposited samples due to percolation, and is therefore no general substitute to the Gaussian disorder on expanded morphologies. The mobilities displayed in fig. 4.8, however, indicate that including local electrostatic effects in the energy landscape may improve prediction quality of charge carrier simulations.

Low charge carrier mobility in OSC materials limits the potential of OSC devices including OLEDs. Computational methods can speed up characterization of new material candidates, helping explore the vast molecular space and boost virtual design. A computational method for mobility prediction requires an accurate representation of the thin-film morphology and material properties, e.g. the disorder of polaron energies. Computation of these material properties in turn requires precise quantum chemistry methods that take into account the unique environment of each molecule in the amorphous morphology.

This section used the *ab initio* multiscale workflow to compute material properties and simulate charge transport and benchmark computed mobilities in 17 organic thin films. This parameter-free approach achieved good agreement to experimental data for computed zero-field and field-dependent mobilities of a wide range of molecules frequently used in OLED stacks.

This multiscale model to predict charge carrier mobility can aid experimental R&D towards the design of efficient OLED materials and devices in three ways: First, without the need to parametrize this model,

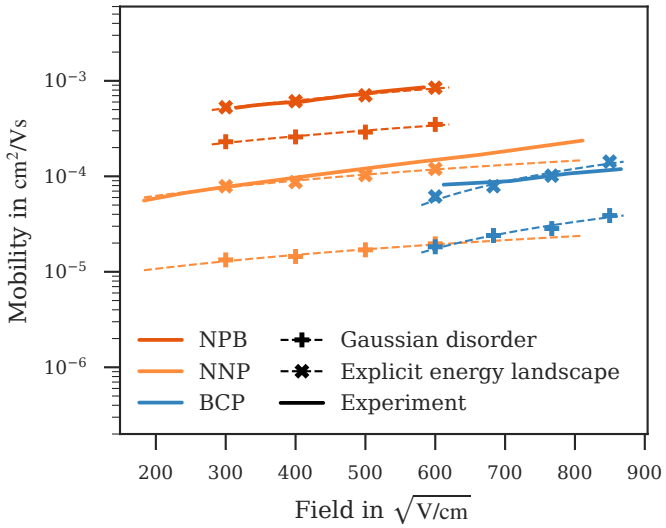

Figure 4.8: Mobilities calculated with regular Gaussian disorder (+) or the energy landscape derived explicitly from local electrostatics (×). Taking into account the local electrostatics improves the fit to experiment for NPB [122], NNP [125] and BCP [117] and properly resolves the difference in NNP and BCP mobility observed in experiment. Dashed lines are fitted to Poole–Frenkel behaviour, simulation errors are of the order of symbol size.

e.g. with experiment, computation of charge carrier mobility enables full virtual screening of materials, thereby allowing to focus experimental efforts to most promising candidates. Second, by bridging the gap between fundamental chemistry and mesoscopic material properties, the presented workflow can aid in gaining systematic understanding on the structure–function-relationship of molecular properties and device performance, as well as derivation of design rules for new materials. Third, this *de novo* workflow can be linked seamlessly to the continuum scale, i.e. drift-diffusion, models which are widely used in OLED development. This link between the micro- and the macro-scale opens the prospect of a higher level of automation in OLED design.

In the pristine systems studied here charge transport is primarily determined by the width of the Gaussian DOS. An accurate description of a mixed system additionally requires knowledge about the position of the mean values of the Gaussian DOS, i.e. mean IP and EA, for the different molecular species. This additional quantum chemical challenge is addressed by recent developments for accurate predictions of IPs and EAs by [134], which can be integrated in this workflow to

facilitate accurate *de novo* mobility predictions in mixed systems, as demonstrated in sections 4.2 and 5.2 and chapter 6.

Ultimately, approaches to include simulation of exciton dynamics and predict device efficiency of multilayer OLEDs, e.g. the studies discussed in chapter 6, based on first principles depend on an accurate description of charge carrier balance, and therefore a reliable model for simulating charge transport through each layer. This study is thus a fundamental step towards full virtual design in OLED technology.

4.1.2 *Tuning electron mobility by disorder passivation*

Reducing exciton quenching persists to be a major challenge in OLED devices. In order to minimize loss processes that limit efficiency and cause degradation, it is essential to balance the charge and exciton density in the device. One promising path towards balanced OLEDs is to tune charge carrier mobility in HTL and ETL [135]. However, especially ETLs often suffer from low mobility due to a large energy disorder induced by the large polarity of the materials [126, 136, 137]. Low ETL mobility not only makes it difficult to create a balanced stack, it also increases driving voltage of the device [138].

One approach to increase mobility is to reduce electrostatic disorder by reducing the polarity of the compounds via molecular design. Chemical modifications, however, often change other key molecular properties such as the HOMO and LUMO energies [29, 139, 140].

This section investigates an alternative approach and analyses the impact of mixing ETL materials with guest materials with low polarity and a LUMO which makes it inert for electron transport. Reducing local energy disorder increases mobility, while a decrease in connectivity limits percolation pathways. As charge mobility in disordered organic semiconductors scales as $\mu \propto exp(-\sigma^2)$ (eq. 4.1) the reduction of the disorder due to the additional material should overcompensate for the worse percolation [105].

To disentangle the opposed effects of disorder and percolation when introducing non-electron-trapping guest material, further termed (disorder-)*passivator*, into polar ETLs, the seamless bottom-up multiscale

modelling approach is used. Concentration dependent charge carrier mobilities are computed for TPBi doped with NPB, which exhibits significantly lower electrostatic disorder than pure TPBi, based solely on first principles. This simple approach can enhance electron mobility in TPBi by one order of magnitude, and the workflow is able to identify the (material-specific) sweet spot in the parameter space.

Following the workflow described in chapter 3 digital twins of TPBi, doped with NPB acting as passivator material (by reducing electrostatic disorder), are constructed. To investigate the effect of the passivator concentration on the electron mobility, thin-films of 2000 molecules with passivator concentrations of 0 %, 25 %, 40 %, 45 %, 55 % and 70 % are deposited into a simulation box of 90 Å × 90 Å × 360 Å with 32 parallel SA cycles starting at an artificially high temperature (4000 K) and cooling to room temperature (300 K) in 130 000 MC steps. Intermolecular interactions during the deposition process are modelled using the LJ parameters of the DEPOSIT standard force field (parameters listed in table A.1) and Coulomb potentials based on ESP charges.

Subsequently, the electronic structure of each resulting thin film morphology with atomistic resolution is analysed using QP. The electronic couplings J_{ij} of a molecule i to its respective neighbour j are calculated for pairs of the innermost 200 molecules with an atom–atom distance of less than 7 Å. Dimer DFT calculations are performed using the BP86 functional and def2-SVP basis set, all other DFT computations are performed using the B3LYP functional and def2-SVP basis set. Using the equilibrated orbital energies of the innermost 200 molecules, the energy disorder σ is calculated from the standard deviation of energy differences ΔE_{ij} of all pairs of neighbouring molecules i and j. For the morphologies at different concentrations in the order stated above, the LUMO disorders are computed to be 169 meV, 146 meV, 134 meV, 132 meV, 129 meV and 119 meV respectively.

Based on the morphologies from DEPOSIT, energy disorder and distributions of electronic couplings, kMC simulations for all systems are performed using the kMC package LF. Accurate, extended systems for transport simulations are obtained, as discussed in section 4.1.1, by periodic extension and subsequent calculation of the electrostatic potential on the extended system. For a parameter sweep systems with the – less accurate but more flexible – corresponding Gaussian distribution of LUMO energies with width σ are used on geometrically extended sys-

tems of 40 nm × 40 nm × 40 nm. In either system, electronic coupling elements J_{ij} for site i and one of its neighbours j are drawn from the microscopic distribution $J(r)$ within the small interval dr around the distance r_{ij} between both sites. EA levels of TPBi and passivator are set to 2.25 eV and 1.9 eV respectively, asserting that charge transport occurs only on TPBi. Reorganization energies are set to 200 meV. To consider bulk mobility (i.e. to neglect injection effects at electrodes) no electrodes are attached to the sample. Instead, 20 electrons, corresponding to an electron density of $3.125 \times 10^{-4}\,\mathrm{nm}^{-3}$, are distributed randomly in a periodic sample and the electron mobility is computed as in section 4.1.1 by measuring drift velocity under an applied voltage in 15 independent simulations.

For the pristine TPBi layer, mobility is computed at various applied fields. Figure 4.9 shows the simulated mobility vs. experimental data from Zhang et al. [136]. Field-dependent mobilities obtained with the energy landscape derived explicitly from local electrostatics (orange) match the experimental data very well, whereas the Gaussian disorder model (blue) underestimates the mobility by a factor of four while reproducing the experimental trend.

Passivator concentration dependent mobilities are computed at a field of $0.03\,\mathrm{V\,nm}^{-1}$ and displayed in fig. 4.10 (left y-axis), along with the energy disorder (right y-axis). These computations show a significant disorder decrease of 35 meV between pristine TPBi and TPBi doped with 40 % passivator, leading to an increase in mobility by a factor of 10. Upon further increase of the passivator concentration, mobility decreases despite a further decrease of energy disorder. This decrease is concluded to arise from diminished connectivity between TPBi molecules at lower concentrations.

To disentangle the impact of connectivity and disorder, mobility simulations are conducted at various passivator concentrations, while keeping disorder constant at various values. The results are depicted in fig. 4.11. As expected, there is a continuous decrease of mobility, when passivator concentration is increased (if disorder is kept constant).

Ultimately, intermolecular hopping is analysed in the transport simulations at different passivator concentrations. fig. 4.12 shows a projection of net-bond hops per molecule on the x–y plane, where x is the transport direction. These analysis show a qualitative thinning of con-

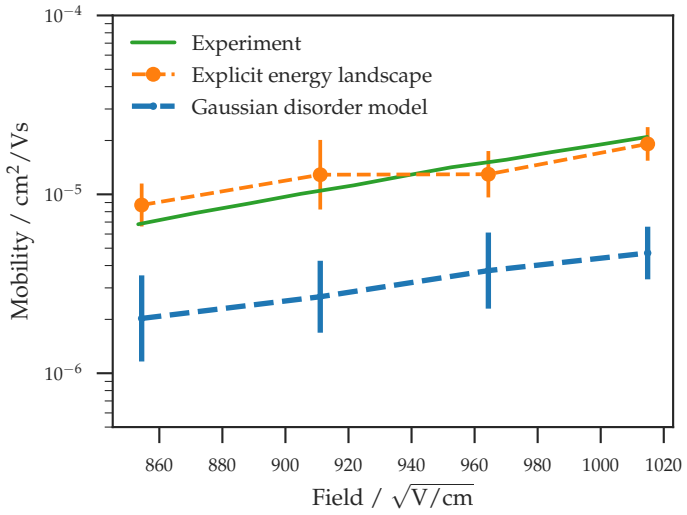

Figure 4.9: Mobility simulated using a Gaussian disorder model (blue) and the energy landscape derived explicitly from local electrostatics (orange) compared with experimental data from Zhang et al. [136] (green). The atomistic electrostatics model shows a very good match between simulation and experiment. Simulations using the Gaussian disorder model underestimate mobilities by a factor of four.

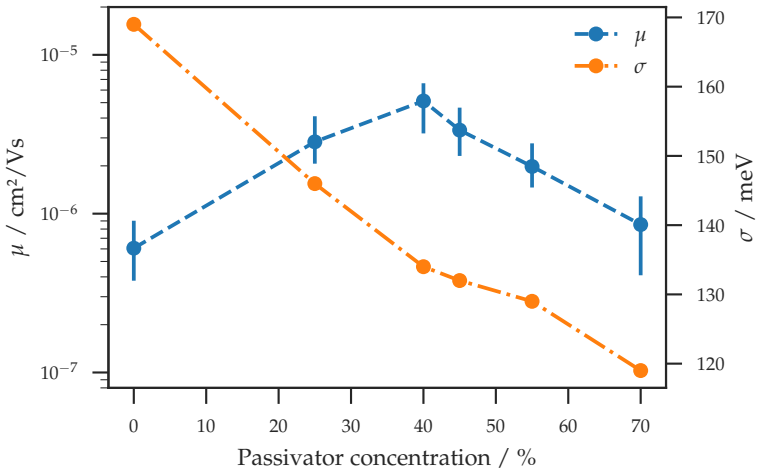

Figure 4.10: Energy disorder (orange) and charge carrier mobility (Gaussian model) (blue) in dependence of the passivator concentration. The decrease in disorder with increasing passivator concentration improves mobility, while the reduced connectivity between TPBi molecules worsens mobility, leading to an optimal passivator concentration of 40 %.

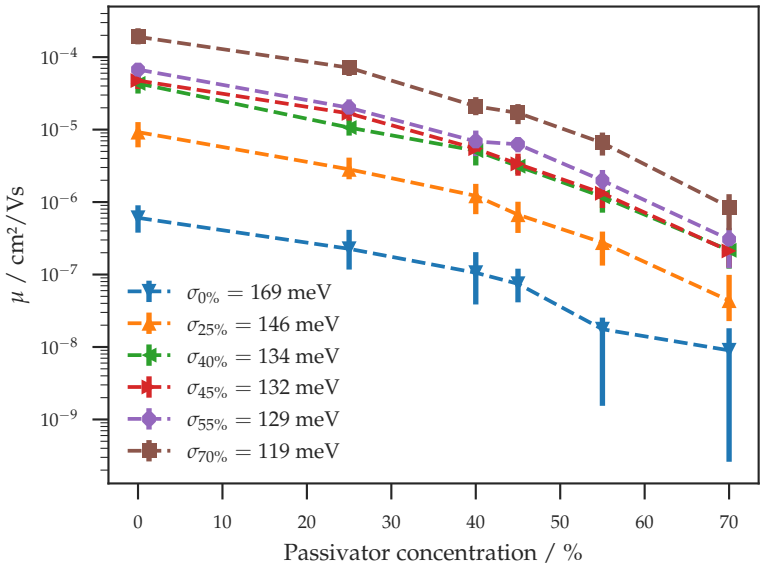

Figure 4.11: Mobilities (Gaussian model) in dependence of passivator concentrations for different disorders (kept constant) show an expected decrease of mobility with increased passivator concentration for all disorders due to limited connectivity.

duction paths with increasing passivator concentration, which can be attribute to the reduced number of connections between TPBi molecules in the diluted samples. Although there appear to be less conduction paths in the system with 25 % passivator concentration compared to the system without passivator, mobility is increased due to decreased disorder in the conduction path (analogous to traffic on many gravel roads vs one highway).

In organic electronics (OE) applications a high degree of control of material parameters such as transport levels and charge carrier mobilities is required to build balanced devices. This work used computer simulations to tune mobility in ETLs by adding transport inert guest molecules with low polarity. By systematically varying individual material parameters, which are not accessible individually in experiment, this work disentangled the impact of two microscopic mechanisms with opposing effects on electron mobility. As shown, an optimal guest concentration for a given mobility target can be found by balancing the disorder and connectivity reduction with increased passivator concentrations. Tuning the passivator concentration allows for targeted design of OLED layers.

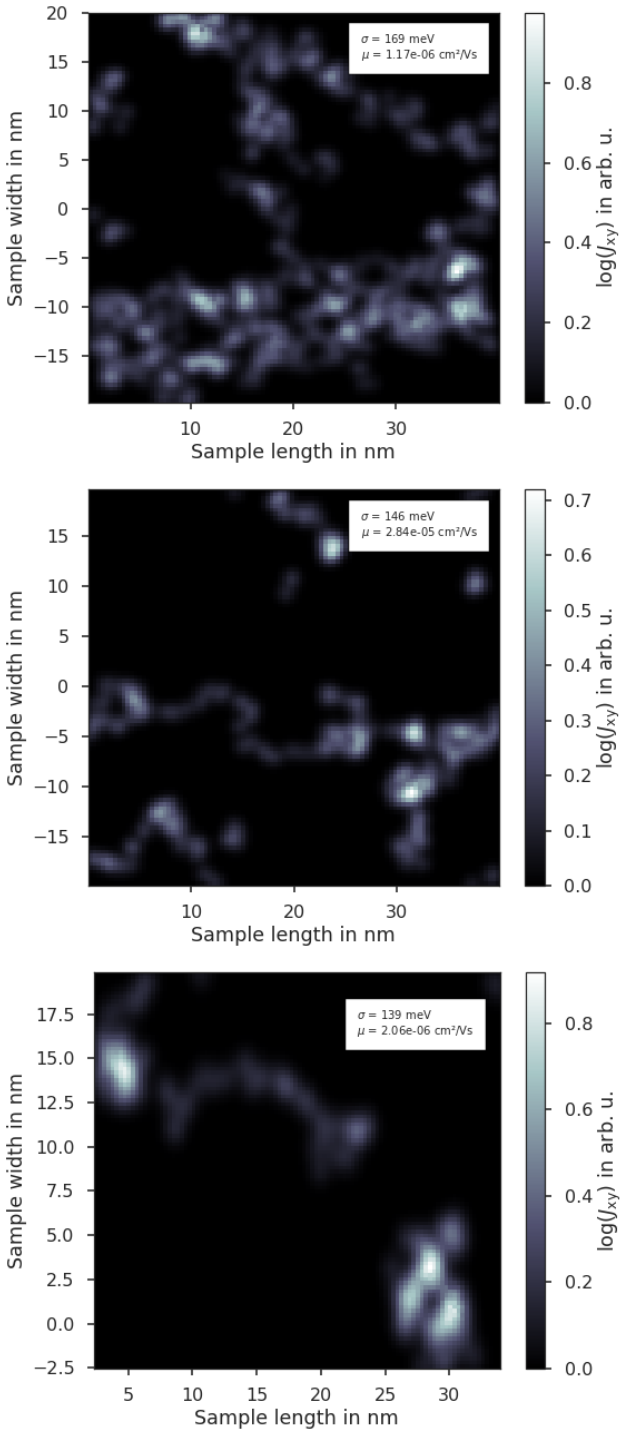

Figure 4.12: Projection of net bond-hops per molecule on the x–y plane (field applied in x-direction), for TPBi with 0 % (top panel), 25 % (middle panel) and 70 % (bottom panel) passivator concentration. Insets show the disorder of the LUMO energies and electron mobilities. The middle panel exhibits the highest mobility of the shown system, although less paths are contributing to the transport.

As the ratio of disorder and connectivity reduction for any passivator concentration are material specific, the experimental screening for both good passivator molecules and their optimal concentrations would be overly time-consuming and costly in the design of novel materials. This study therefore demonstrates how parameter-free computer simulations from first principles can aid experimental R&D of OLED materials and devices by efficient screening of materials and device parameters. Furthermore, by connecting fundamental chemistry and device design, these multiscale simulations provide fundamental understanding of how entangled microscopic properties impact device performance. This approach therefore enables material and device designers to investigate the impact of specific molecular properties on layer and device performance and to derive structure-function relationships between chemical structure and the performance in the device, leading to design rules for organic materials and devices.

4.2 SIMULATING CHARGE TRANSPORT IN SINGLE CARRIER DEVICES

The study presented in this section was published as [A5].

Modern OLEDs are composed of multiple thin layers of small organic molecules, each of which must be carefully optimized to play its integral role in the device performance. Holes and electrons are injected into HTL and ETL directly from the electrode or indirectly via a DILs and traverse the system in opposite directions to recombine in one or more EMLs. For efficient device operation, it is crucial that charges are injected and transported efficiently in both the HTL and ETL, providing both types of charge carriers to the EML at a high and balanced rate.

The injection into the HTL and ETL is governed by the IP and EA, respectively, of the molecules in the thin films with respect to the electrode work function, as well as the disorder of polaron energy levels σ [141]. The transport properties are governed by the charge-carrier mobility, which mainly depends on σ, the electronic couplings and the presence of deep traps [32, 44]. In the case of efficient charge injection, i.e. with ohmic contacts, the current through a device will be space-charge limited, the magnitude of which depends on the temperature-, field- and density-dependency of the mobility [113]. While the IP of the ETL and

the EA of the HTL are not relevant for charge transport to the EML, they are important for confinement of charges and excitons inside the EML.

Traditionally, experimental techniques are used to develop materials with appropriate IP and EA for optimizing injection and energy-level matching with the EML. While gas-phase IP and EA of the molecules can be calculated straightforwardly and provide a first hint at their suitability, they deviate from the bulk values because of polarization effects which ultimately require experimental measurements to obtain reliable values. Among current methods for measuring IP and EA of a material are ultraviolet photoelectron spectroscopy (UPS)[142] and LEIPS. These methods account for the influence of the polarizable medium, but are limited to typical accuracies of about 200 meV [143] and 100 meV [144] for EA and IP, respectively. Deviations of this magnitude remain significant, since the injected current depends exponentially on the injection barrier [145].

Experimentally, the charge carrier mobility of an organic film can be extracted from the SCLC through a thin layer with ohmic contacts [146] or the ToF of induced charge carriers in a micrometer-thick sample [111]. In SCLC measurements injecting contacts have to be carefully optimized to eliminate injection barriers, while ToF measurements require trap-free and non-dispersive charge transport for a reliable evaluation of the transient mobility.

Each step in the device fabrication – from synthesizing the molecules, depositing pristine layers, fabricating devices to measuring relevant parameters – is both challenging and time-consuming. Even with all the parameters measured, the exact behaviour of the OLED is difficult to predict, requiring fabrication of multiple samples with different configurations to develop an efficient OLED. *Ab initio* multiscale workflows can help screen molecules and device configurations for the desired properties [A9, 32, 35].

This section demonstrates *de novo* simulations of two unipolar single-layer devices featuring ohmic charge injecting electrodes using the multiscale workflow (chapter 3). To this end, material properties of *N*,*N*′-di(1-naphthyl)-*N*,*N*′-diphenylbenzidine (α-NPD) and TPBi are characterized, two molecules commonly used as hole- and electron-transport material in OLEDs, respectively. Based on these properties, the kMC model is used to simulate charge transport in devices and calculate

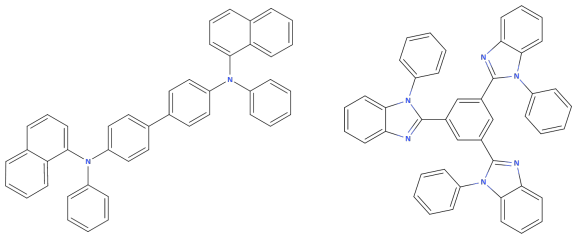

Figure 4.13: Single carrier devices investigated in this section compose of α-NPD (left) and TPBi (right).

experimentally validated current density–voltage (*J*–*V*) characteristics. The charge transport model fully accounts for the amorphous structure of the materials and the many-body interaction of charge carriers – in contrast to previous works [35, 38] – which can lead to significant errors in the regime of ohmic injection [107, 109]. With only the molecular structure and electrode work functions as input, the final current density–voltage characteristics show a very good agreement with experiment. Development of such a multiscale workflow paves the way for the in-depth study and computational design of multilayer OSC devices like OLEDs and organic solar cells (OPVs).

The devices were produced and measured by the group of Prof. Blom at the Max Planck Institute for Polymer Research in Mainz.

Hole-only devices were fabricated by sandwiching a thermally evaporated layer of α-NPD (100 nm) between a hole-extracting bottom electrode consisting of poly(2,3-dihydro-thieno-1,4-dioxin):poly(styrenesulfonate) (PEDOT:PSS)-covered indium-tin oxide (ITO) and an ohmic hole-injecting top electrode consisting of a 5 nm TCTA interlayer, a 10 nm MoO_3 layer, and a 100 nm Al layer consecutively evaporated on top of the α-NPD layer. The TCTA tunnelling interlayer prevents the formation of a hole-injection barrier [38], providing ohmic hole injection from the top electrode. Electron-only devices consist of a thermally evaporated layer of TPBi (115 nm) sandwiched between an electron extracting Al (30 nm) bottom electrode and an electron-injecting Ba(5 nm)/Al(100 nm) top electrode. The current density–voltage characteristics were measured under N_2 atmosphere with a computer-controlled Keithley 2400 source meter at various temperatures.

To calculate the current density–voltage characteristics for the different devices, the multiscale workflow discussed in chapter 3 (fig. 4.14) is

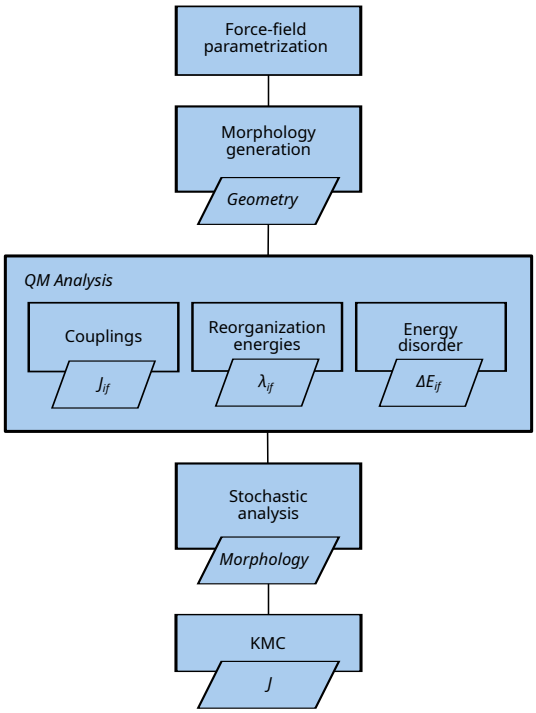

Figure 4.14: Multiscale workflow used to bridge length- and timescales required for the device simulations. Classical force fields are parametrized with the molecular structure using DFT. The DEPOSIT protocol uses these force fields to deposit an amorphous morphology. DFT calculations with the QUANTUMPATCH method provide parameters for the Marcus Rate. The stochastic expansion method generates an amorphous device structure from the deposited morphology and data from the QM Analysis. Charge transport in the device is simulated with the kMC device model.

used. All DFT calculations are performed using the DFT package TURBOMOLE with the B3LYP functional and def2-SVP basis set unless noted otherwise.

To obtain representative atomistic models of the amorphous thin-film for each material, 1000 molecules are deposited using the DEPOSIT protocol mimicking the physical vapour deposition process. The molecules are sequentially added to a simulation box of 80 Å × 80 Å × 300 Å with PBC in x- and y-direction. In each SA cycle, the molecule samples the morphology surface starting from an artificially high temperature (4000 K) to room temperature (300 K) in 150 000 MC steps, providing sufficient sampling for the organic molecules studied here [94]. To improve sampling, 32 SA cycles are run in parallel with the final candidate selected

based on the Metropolis-criterion. Intermolecular interactions are modelled using Coulomb potentials based on ESP charges and LJ potentials derived using the DEPOSIT standard force field (parameters listed in table A.1).

In these morphologies IP and EA, reorganization energies, λ_i, distribution of HOMO and LUMO energies as well as electronic couplings, J_{if}, of a subset of molecules in their unique environment are calculated using the QP method. IP and EA are calculated as the total energy difference of single molecules in the charged and uncharged state for 10 molecules within each morphology. The reorganization energies λ_i are calculated based on Nelsen's four point procedure for the previous 10 molecules. The geometry of each molecule is optimized in the charged and uncharged state with the constraints imposed by the environment modelled with ECP at the positions of surrounding atoms. The conformational response of the environment is neglected. The disorder σ is calculated from the distribution of $\Delta E_{\mathrm{HOMO/LUMO}}$ from the orbital energies of the innermost 200 molecules. Electronic coupling elements are calculated from the hopping-matrix elements of dimers for charged–uncharged-pairs following the Löwdin orthogonalization procedure using the BP86 functional. Pairs are selected with an atom–atom-distance cutoff of 7 Å, a value much larger than the typical π–π-stacking distance where the electronic coupling is already insignificantly small, as can be seen in fig. 4.15. Each calculation is done in the converged electrostatic environment of arbitrary molecules near the centre of the morphology.

To accurately model charge transport in these devices, the morphologies are stochastically expanded to a base of 20 nm × 20 nm and the height of the device. The IP and EA of each site in the resulting amorphous structure is drawn from the Gaussian distribution with width σ and centre at the microscopic IPs and EAs. Electronic coupling elements J_{if} for each site i and connected sites f with a pair distance of r_{if} are drawn from the microscopic distribution of electronic couplings J' within a small interval dr around r_{if}. Connectivity of a given pair is determined by the probability of a COM distance r_{if} relating to an atom–atom-distance below the cutoff in the electronic structure calculation. Reorganisation energies are taken to be constant.

To model current density measurements in the device, electrodes with fixed work functions W are attached in transport direction, resulting in

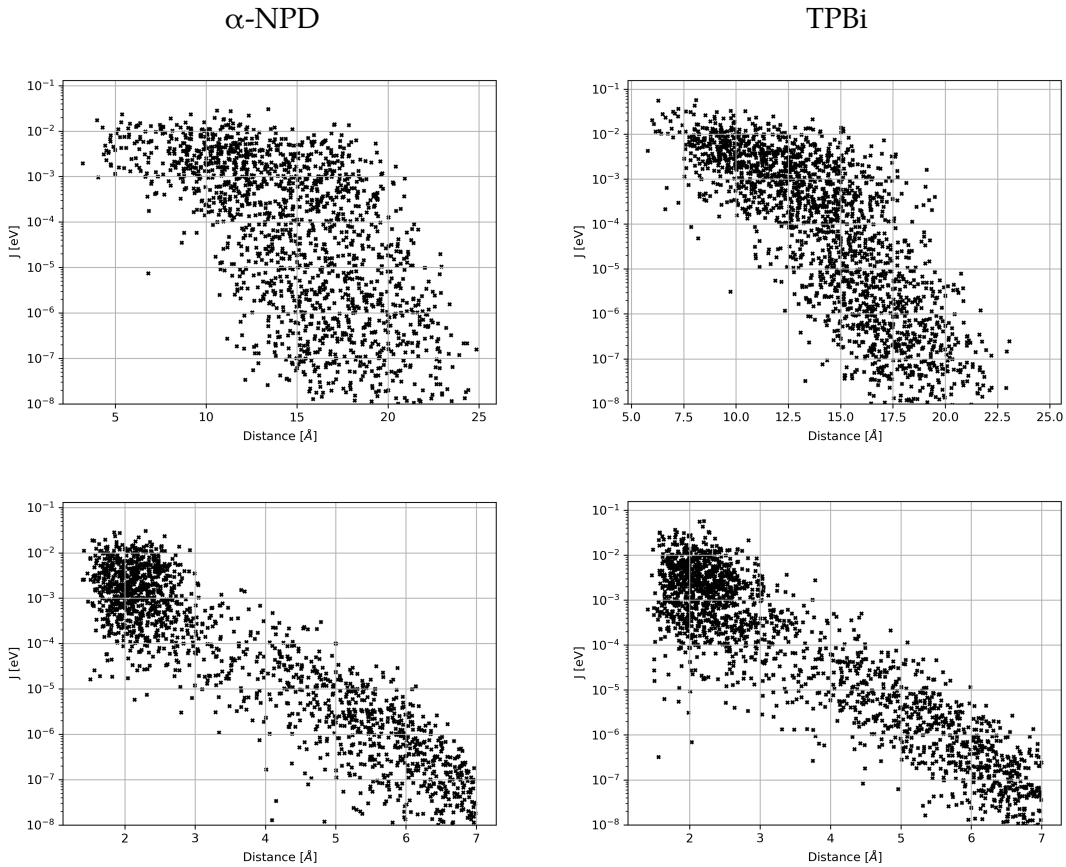

Figure 4.15: Distribution of electronic couplings J computed with the QP method for the two molecules studied in this section α-NPD (left) and TPBi (right). Top: COM distance; bottom: nearest atom–atom distance.

an injection barrier $\Delta E_{ij}^{\mathrm{IB}}$ given by eq. 3.10. The barrier at the extracting contact is defined analogously. The dynamic electrostatic potential is reevaluated after each charge movement by calculating the electrostatic Ewald Sum [147] including all charges in the system and an infinite series of image charges due to the metallic boundary conditions at the electrodes.

Periodic boundary conditions are applied perpendicular to the transport direction, i.e. in y- and z-direction. To account for stochastics in morphology expansion and site energy distribution, 10 different configurations are sampled per applied field. Connectivity of a given pair of sites with distance d is determined by the probability of a pair of molecules with a COM distance d having a nearest atom distance of less

Table 4.3: Microscopic input parameters for the charge transport simulations of the α-NPD and TPBi device calculated with the QP. Namely ionization potential (IP), electron affinity (EA), disorder (σ), reorganization energy (λ) and average electronic couplings ($\langle J^2 r^2 \rangle$) along with references to literature values where available.

Molecule	IP/eV	EA/eV	σ/meV	λ/meV	$\langle J^2 r^2 \rangle$/eV^2 Å^2
α-NPD	5.48[a,b]	1.93[a]	96[c]	216	1.57×10^{-3}
TPBi	6.79[d]	2.07[d]	162	237	2.33×10^{-3}

Literature references: [a] [148, 149] [b] [150] [c] [151, 152] [d] [153]
The uncertainty of IP and EA are 31 meV and 51 meV for α-NPD and TPBi, respectively, both well below the accuracy of the computational method. The standard deviation of λ is less than 10 %. The statistical error in σ due to limited sample size of $\Delta E_{\mathrm{HOMO/LUMO}}$ is below 5 %.

than 7 Å . Hopping transport is possible between all connected pairs with both direct and superexchange coupling taken into account. Convergence is reached when the current density is constant over two thirds of the simulation. Current density is computed from the average drift velocity of the charge carriers in the converged part of the simulation.

The presented multiscale workflow is used to calculate material properties for α-NPD and TPBi, two materials commonly employed in hole or electron transport layers of modern OLEDs, respectively. Subsequently, device characteristics of unipolar single-layer devices composed of these materials are simulated at different driving voltages and temperatures. Both the material properties (table 4.3) and device characteristics (fig. 4.17) are in good agreement with experimental data.

The nearest-neighbour distributions of extended structures, depicted in fig. 4.16, closely match that of the deposited morphology with a slight trend to underestimate the distribution at small distances and overestimate the peaks of the distribution. These small deviations, however, have only little impact in the charge transport through the devices. Figure 4.17 shows the simulated current densities compared to experimental measurements. With decreasing voltage the probability for a charge carrier to overcome the attractive potential of its image charge decreases, leading to an increasing part of the simulation time being spent on charge injection, extraction and hops along the electrode–HTL interface, requiring a trade-off between level of detail and simulation time. Simulations are therefore limited to current densities

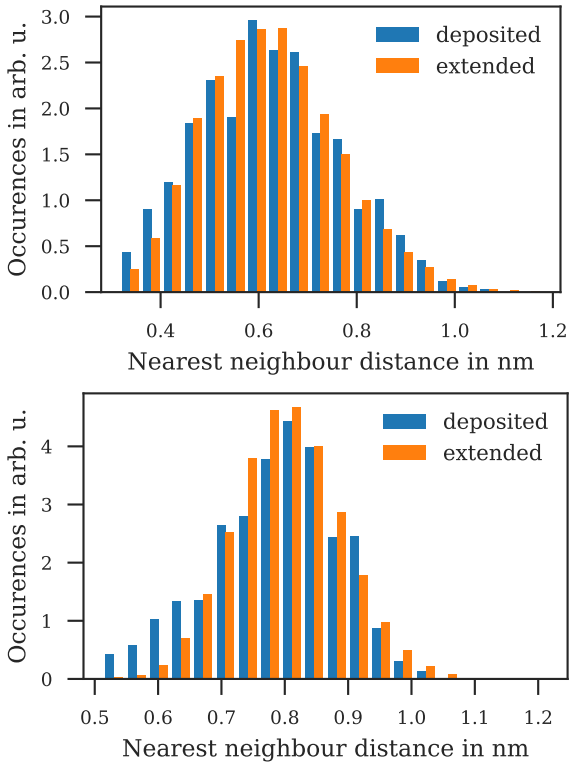

Figure 4.16: Nearest-neighbour distribution of the deposited morphology (blue) and expanded structure (orange) of α-NPD (top) and TPBi (bottom).

above 100 A m^{-2} for α-NPD and 10 A m^{-2} for TPBi. As can be seen, the simulated current densities agree well with the experimental current densities over a broad range of voltages and temperatures. Both devices feature ohmic contacts, even accounting for the differences in built-in voltages, however, the TPBi device shows lower current densities at comparable applied voltages than the α-NPD device, mainly caused by larger ΔE_{ij} in the exponent of eq. 2.4 due to the larger disorder in the TPBi device.

Charge carriers inject from the ohmic contacts, shifting the vacuum level until the edge of the transport level aligns with the electrode work function. The resulting space-charge effectively shields the interface region from the external electric field, leading to flat transport levels in the vicinity of the injecting electrode and in turn amplifying the external field far away from this electrode. Both effects are evident in the distribution of site energies, i. e. IP or EA with the external field

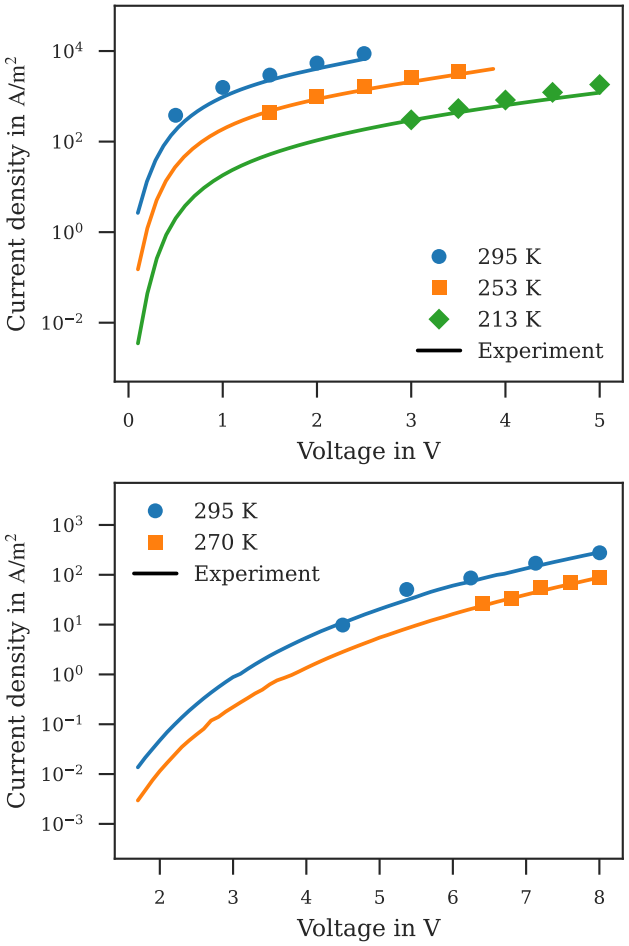

Figure 4.17: Simulated current density–voltage (J–V) characteristic of α-NPD (top) and TPBi (bottom) at different operating temperatures compared with experiment. Simulation errors are of the order of symbol size.

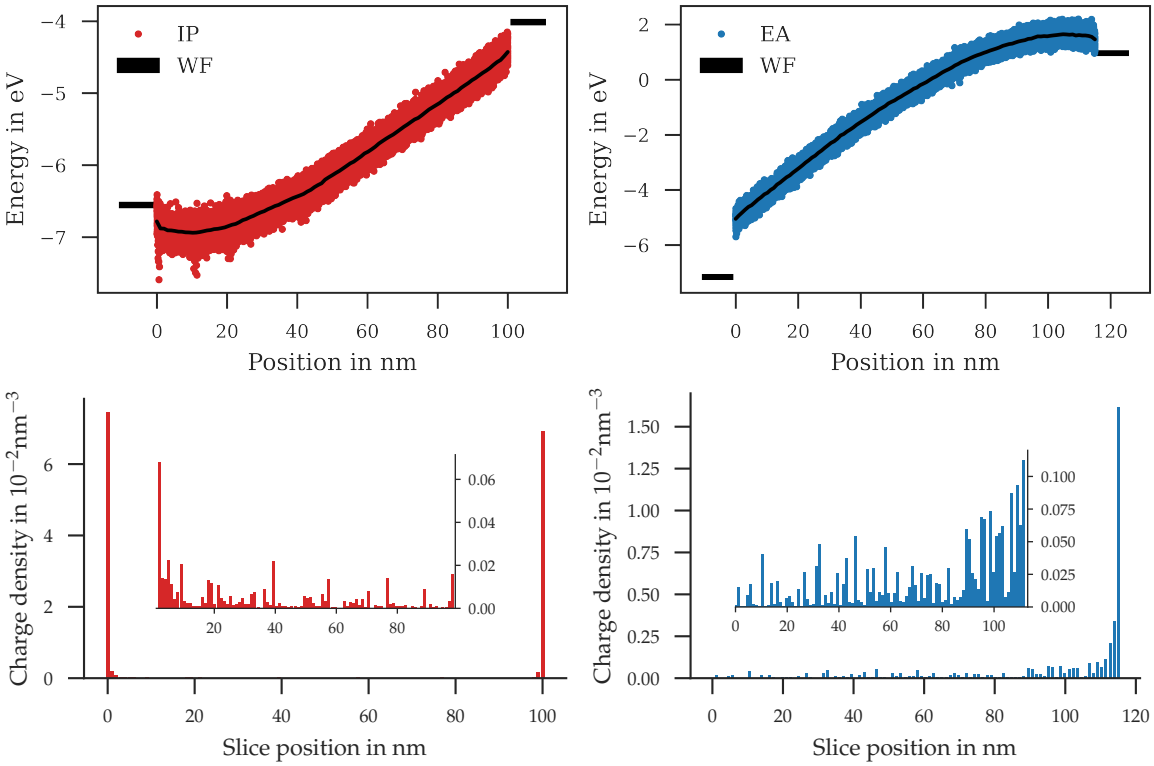

Figure 4.18: Insight into the α-NPD (left) and TPBi (right) devices with a Voltage of 2.5 V and 8 V applied respectively. Top panels: Energy diagram depicting each site energy including applied field and dynamic coulomb potential of all charges in the system averaged over 1000 kMC steps. Outliers are artefacts when sites are partially occupied during the short averaging window. Bottom panels: Charge density in slices of 1 nm in transport direction averaged over half of the simulation.

applied and the dynamic coulomb potential of the charges in the system, depicted in fig. 4.18 (top panel). Figure 4.18 (bottom panel) shows the charge densities in slices of 1 nm in transport direction averaged over the second half of the simulation. As can be seen, most charge carriers are situated in the space-charge region or, in the α-NPD device, next to the extracting electrode. The exact charge density at the electrodes depends on the injection barrier, leading to large charge-carrier densities at the ohmic injecting electrodes, slightly lower hole-density at the extracting electrode of the α-NPD device with a small initial barrier of 0.2 eV and a negligible electron-density at the extracting electrode of the TPBi device with a large initial barrier of 1.7 eV. Small features in the average charge densities far away from the electrodes are caused by shallow

traps leading to longer occupation times. Due to the larger disorder, traps are more likely to occur in the TPBi device, resulting in stronger fluctuations of the average charge density in the bulk of this device than in the α-NPD device. In the simulations, the probability of a charge carrier escaping the space-charge region is small, with the subsequent propagation through the bulk of the device being fast compared to the escape time. The exact ratio determines the current density J and depends on the applied voltage V and charge-carrier mobility in the device μ, recovering the Mott–Gurney equation [113] $J \sim \mu V^2$ in the space-charge-limited regime.

This section uses the multiscale workflow to determine both material properties and the charge transport characteristics in single-carrier devices made from these materials without experimental input. This approach shows good agreement to experimental data for single-carrier devices comprising α-NPD and TPBi, two prototypical materials in hole and electron transport materials, respectively. Demonstrating that a multiscale approach is now capable to characterize complex electronic devices *de novo* without experimental input. As shown in section 4.3, this multiscale workflow can be easily extended to model multilayer devices enabling in-depth studies of multilayer devices like OLEDs and OPVs. The bottleneck here is solely the computational cost of the kMC calculations, which is being improved, e.g. with the method presented in section 6.4.

Broadening the emission zones can reduce exciton quenching processes, which are among the prime reasons for OLED degradation [83]. The width of the emission zone depends on the penetration depth of charge carriers into the EML. An excess of electrons or holes leads to excess exciton formation close to the HTL– or ETL–EML interfaces, respectively. Tuning the transport properties of both HTL and ETL to increase carrier balance in the EML can thus increase both efficiency and lifetime of OLED devices [83]. The developed workflow enables future studies to investigate transport properties in detail and thus aid in optimizing OLED devices.

4.3 SIMULATING A MODEL OLED STACK

The study presented in this section was published in collaboration with Symalla et al. [A10] and presented in collaboration with Symalla et al. [P6].

While computer simulations are widely used in organic electronics to support experimental R&D, established methods such as DD are based on parametric models and simulations rely on experimental input for parameters such as energy levels or charge carrier mobilities. This hinders the design of novel materials and optimization of devices fully in the computer. Therefore, industrial R&D relies on time consuming and costly trial and error approaches.

This barrier can be overcome with a bottom-up multiscale modelling approach starting on the quantum mechanical level that maps single molecule properties to the device scale without the use of external parameters, e.g. from experiment. To this end, the multiscale model used to simulate charge transport in single-layer devices in section 4.2 needs to be extended to model exciton dynamics, as discussed in section 3.4, enabling the simulation of a multi-layer OLED. By including relevant effects and processes on the microscopic scale, this approach a) generates insight on information that is not accessible by experiments (artificial microscope) and b) allows researchers to analyse the impact of specific microscopic effects on device performance. This enables a straightforward and systematic identification of bottlenecks and allows the targeted development of compounds tailored for specific purposes and the optimization of layer architectures, fully in the computer.

The multiscale simulation workflow follows the one in section 4.2. Thin-films are deposited with 600 molecules in a box of 80 Å × 80 Å × 160 Å with PBC in x- and y-direction in 32 parallel SA cycles from 4000 K to 300 K in 30 000 MC steps. Within these amorphous morphologies, IP, EA and reorganization energies λ_i are computed for 10 arbitrary molecules in the centre of the morphology. The disorder σ is computed from the distribution of HOMO and LUMO energies of the innermost 150.

Electronic couplings J_{ij} for all pairs of molecule species are calculated from the hopping–matrix elements of dimers for charged–uncharged-pairs using the BP86 functional in a combined morphology with 500 mo-

lecules of 9,10-diphenylanthracene (ADP) followed by 500 molecules of ADP with two carbon atoms substituted for nitrogen (ADP(N)) deposited into a box of 120 Å × 120 Å × 240 Å and all other parameters as above.

For the kMC simulation of charge and exciton transport, the pure amorphous thin-films are expanded to 20 nm × 20 nm × 20 nm each and attached to electrodes on both ends in transport direction. Workfunctions are chosen to obtain an injection barrier of 0.3 eV, i.e. $W_{\text{anode}} = 4.4\,\text{eV}$ and $W_{\text{cathode}} = 3.3\,\text{eV}$. PBC are applied in directions perpendicular to transport.

Rates for the individual processes are computed according to Marcus theory (eq. 2.4) based on the electronic structure calculations. Energy levels and hopping rates are continuously reevaluated to account for changes in the local coulomb potential. Recombination and exciton separation rates for electrons and holes are calculated based on local ionization energy, local electron affinity, local coulomb potential, optical gap and intermolecular coupling and spacing. Thus, changes of e.g. interface charge densities during operation will influence recombination rates.

Förster transfer rates are computed using the phenomenological expression [65]

$$k_{\text{Förster}} = \frac{1}{\tau_{\text{D}}} \left(\frac{r_0}{r_{\text{DA}}} \right)^6 \tag{4.2}$$

with both the fluorescent lifetime of the donor τ_{D} and the Förster radius r_0, derived from experiment. Rates for Dexter transfer are based on *ab initio* computations. TTA is treated heuristically, such that a transfer of an exciton to an excited molecule will quench the original exciton. TPQ and PTQ are treated equivalently: energy transfer on a charged molecule quenches the exciton, as does charge transfer on an exciton. The IQE is computed based on the exciton events of all samples as the fraction of exciton decays which resulted in the creation of a photon.

Taking into account relevant excitonic and charge transport processes, these simulations allow the detailed analysis of microscopic bottlenecks in device performance.

To demonstrate how the OLED workflow can be applied to design OLED stacks from scratch, solely on the basis of single molecule information,

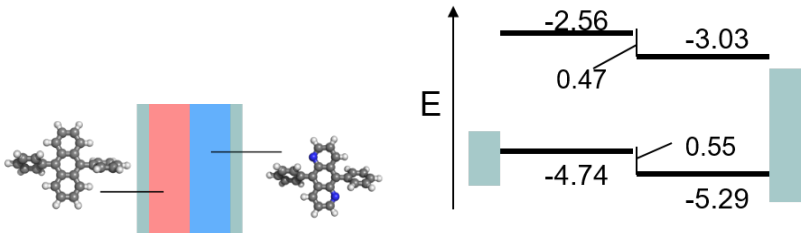

Figure 4.19: Left: Setup of the minimal working example for OLED design from scratch: One layer consists of ADP, the other layer of ADP where nitrogen is substituted for two carbon atoms. This shifts the energy level to create an interface for exciton generation. Right: Computed energy levels of the bilayer system.

this section constructs a minimal working example on the basis of the molecule ADP. To create an interface for exciton generation, i.e. a shift in energy levels, a second layer consisting of ADP is introduced, in which nitrogen is substituted for two carbon atoms. The device setup is displayed in fig. 4.19.

Following the OLED workflow described in chapter 3, atomistic morphologies are generated and energy levels (fig. 4.19, right), energy disorder and electronic couplings are computed for pristine layers of ADP and ADP(N) as well as for an interface of both materials. Using these results, microscopic rates for charge transport are computed and applied in a kMC simulation to compute field dependent *J*–*V* characteristics and IQE. IQE is computed by counting photons emitted and dividing by the number of charges injected into the system at the electrodes over the course of the simulation. *J*–*V* and IQE are displayed in fig. 4.20. To investigate the reason for the IQE roll-off, spatial distributions of charge carriers, exciton generation, photon emission and exciton quenching are analysed at two different voltages in fig. 4.21.

The kMC simulations, solely based on quantum mechanical information, provide a smooth *J*–*V* curve, as well as the drop in IQE for higher voltages (roll-off) that is typically observed in OLED devices. The fundamental reason for the roll-off can be explained by the distributions in fig. 4.21: At low voltages, excitons are created mostly in the interface region, while charge at the interface can be depleted. At higher voltages, however, the increased interface charge cannot be depleted quick enough, leading both to higher charge concentration and penetration of the blocking layer. The generally higher charge density in areas where ex-

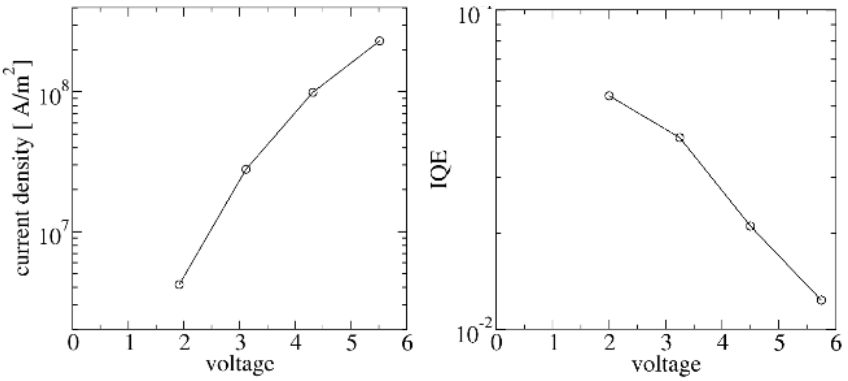

Figure 4.20: Device characteristics of the bilayer stack, namely current density–voltage (J–V) (left) and internal quantum efficiency (IQE) (right).

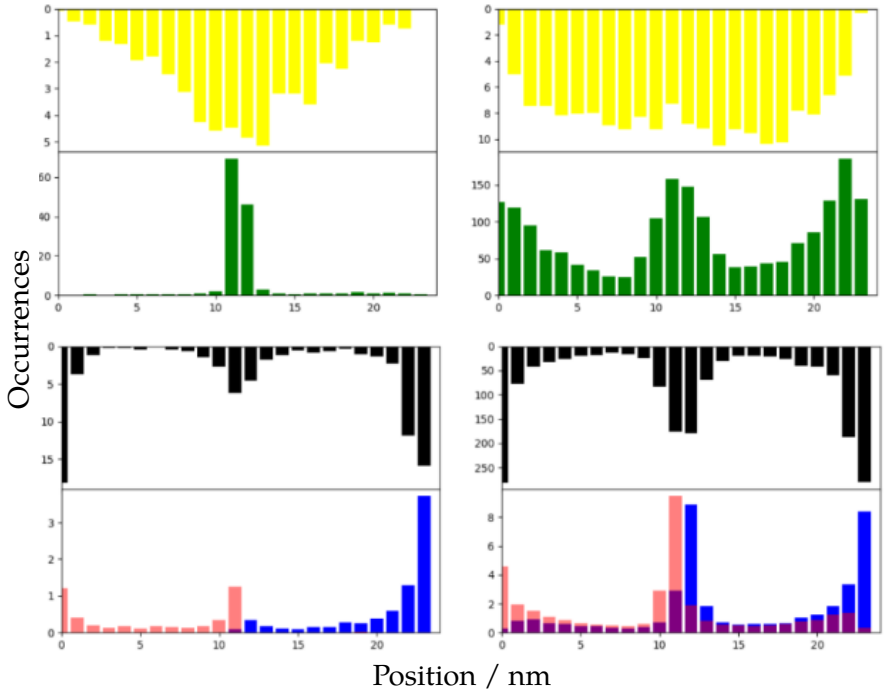

Figure 4.21: Photon generation (yellow), exciton generation (green), exciton quenching (black) and charge carrier density–distribution throughout the device, for $V = 2.0\,\mathrm{V}$ (left) and $V = 5.75\,\mathrm{V}$ (right). At larger voltages, charge density at the interface is higher and the interface efficacy in blocking holes and electrons is reduced, leading to an increase in exciton quenching processes with electrons or holes as well as higher leakage current, and therefore a decrease in device efficiency (roll-off).

citons are formed lead to exciton quenching. Due to the penetration of the interface, there is significant exciton generation also within the layers and at the electrodes, i.e. in regions of high charge density. The overlap of charge density and exciton creation density leads to an increased number of exciton quenching processes, thereby decreasing IQE. Furthermore, at high voltages, single charge carriers reach the opposite electrodes without generating excitons.

Starting from the initial idea of a simple bilayer OLED device, the conducted simulations give clear strategies for device improvement: a) blocking layers prevent charges to travel beyond the emissive zone and b) emissive layers with guest–host systems can be introduced to confine excitons to a defined emissive zone, minimizing quenching processes and therefore improving roll-off. While these are in fact no novel insights in OLED design, this work nonetheless exemplifies how parameter-free computer simulations can be applied to iteratively design OLED devices bottom-up starting on the molecular level. The workflow is easily extended to state-of-the-art multilayer stacks , as demonstrated in chapter 6, to either screen device parameters such as compounds, guest–host-combinations, doping, layer thicknesses, etc., or to systematically gain insight on microscopic processes that is hard to access in experiment (or not at all) and determine fundamental bottlenecks in device performance.

This section demonstrates the ability of the workflow to compute OLED device properties seamlessly based on *ab initio* calculations. In contrast to other methods, no parametrization, e.g. from experiment, is required, enabling full virtual design of materials and devices. To demonstrate the workflow as a tool to stack design from scratch, a bilayer system is simulated and microscopic processes are analysed in order to identify the bottlenecks in device performance and derive strategies for efficiency improvement.

5

MODELLING DOPED INJECTION LAYERS

In the model OLED simulated in section 4.3, charge carriers are injected directly into the ETL and HTL, while efficient modern OLEDs feature DILs to lower injection barriers and generate free charge carriers, increasing conductivity of injection layers [16–18]. A major challenge is the material dependence of the performance of DIL which complicates the optimization of material combinations and doping concentrations for a specific OLED stack. Specifically, it is not understood how microscopic molecular properties of dopant and host material determine device performance, and custom-tailored development of host–dopant material combination and optimization of doping concentration for a specific purpose via trial and error fabrication, production and characterization remains a time-consuming and costly process.

This section demonstrates the capability of the kMC model to simulate DILs and its potential use in screening host–dopant combinations and optimization of DIL parameters for a given host and dopant. First, the work presented in section 5.1 investigates the effect of various parameters on doping efficiency and charge transport. Secondly, section 5.2 derives a method to compute charge transfer (CT) states, having a large influence on doping activation [154, 155], and other parameters relevant for doping completely from first principles. Finally, the model is validated against experimental data measured by Gao et al. [156] and used to find optimal doping parameters in section 5.2.

5.1 PARAMETRIC STUDY OF DOPED INJECTION LAYERS

The study presented in this section was published in collaboration with Özdemir† et al. [A4].

To help improve understanding of doping effects, this section studies the effect of doped HILs on the injection barrier in dependence on material and layer properties by using the kMC model, focussing on a) the Fermi level alignment of the DIL and b) how the p-doping influences the conductivity of the device. This study confirms that the kMC model is able to perform device and material simulations to systematically investigate the influence of doping concentration, material properties and layer thickness on Fermi level alignment and device conductivity.

To investigate the behaviour of DILs, simulations are performed on systems represented by simple cubic latices [44, 81] for each organic layer with a lattice constant of $d = 1\,\text{nm}$ [36]. Electronic properties like the IP of the host material, EA of the dopants or energetic disorder are treated as parameters. The electronic couplings J_{ij} for charge transport, injection and extraction are parametrized [157]

$$J_{ij} \approx j_0 \exp\left(2\alpha r\right) \tag{5.1}$$

as a base electronic coupling j_0 and an exponentially decaying exchange coupling with α describing the spatial extent of the wave function. The values for j_0 and α are listed in table A.2.

Doping activation and charge transport are simulated in systems with a base area of $15\,\text{nm} \times 15\,\text{nm}$ and PBC perpendicular to the transport direction. Electrodes are attached at both ends of the device in transport direction at a distance of 0.8 nm from the first and last layer, i.e. 0.2 nm closer than the lattice spacing d. The workfunctions of both electrodes are taken as 4.5 eV. After each kMC-step, the dynamic Coulomb interaction, which is of particular importance in modelling doping activation [158], is recomputed by performing an Ewald-summation [147]. To account for stochastics in dopant and site energy distribution, 7 different configurations are sampled for each configuration.

The DIL consists of host (H) and dopant (D) sites arranged in a cubic grid with the dopant sites randomly distributed on the lattice. For p-doping, the dopant extracts an electron from a host site, leading to an ionized host and negatively charged dopant molecule

$$H + D \rightarrow H^+ + D^- \,. \tag{5.2}$$

5.1.1 *Effect of a doped injection layer on the voltage drop across the device*

The first part of this study investigates the effect of the doping concentration on the hole injection barrier between the anode and the DIL. The schematic structure of the simulated device is shown in fig. 5.1a. It consists of two organic layers where the first one is the DIL and the second one serves as hole blocking layer, with a layer thickness of 15 nm each. Both electrodes have the same workfunction $W = 4.5\,\mathrm{eV}$ and no external voltage is applied. After activation of the host–dopant pairs free holes are extracted at the anode, leaving a negative net charge in the organic layer, causing an upwards shift of the energy levels. This process takes place until the tail states of the organic layer align with the Fermi level of the anode. Figure 5.1b shows the energy levels of the device after Fermi level alignment. As the energy barrier between the DIL and insulating layer is constant, the Fermi level alignment causes a voltage drop in the insulating layer, which is observed in a slope of the energy levels. Reduction of the injection barrier ΔE_{IB} is computed as the difference in average site energies of the first and last 1 nm–slice of the insulating layer.

Depending on the initial injection barrier, a low doping concentration may be sufficient to reach Fermi level alignment. Therefore, this part studies ΔE_{IB} in the insulating layer at different initial injection barriers and doping concentrations. This study is performed on the device displayed in fig. 5.1 at different doping concentrations and energy levels of the host and dopant sites. The difference between IP and EA is kept constant at 0.5 eV to ensure equal doping efficiencies between the simulations. The simulation is performed with $\lambda = 0.2\,\mathrm{eV}$ for all three site types and $\sigma^{\mathrm{IP}}_{\mathrm{H/D}} = \sigma^{\mathrm{EA}}_{\mathrm{H/D}} = 0.15\,\mathrm{eV}$ for the host and dopant sites. The parameters for electronic couplings and the reorganization energies for charge transfer and doping activation are identical.

Doping concentration has substantial impact on ΔE_{IB} as a function of host IP (see fig. 5.2). The reduction of the injection barrier at a host IP of 5.0 eV with a doping concentration of 10 % is slightly below ΔE_{IB} for 1 % which can be explained by a doping induced broadening of the energy distribution in the DIL (increase in energetic disorder) and the resulting overlap between the tail states and the Fermi level of the electrode. For larger initial injection barriers (larger host IP), higher doping concentration leads to a significant increase of ΔE_{IB}. While at

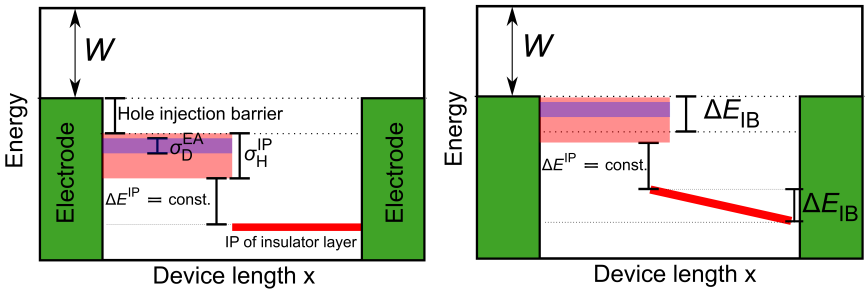

(a) Before activation of dopants (b) After activation of dopants

Figure 5.1: Schematic energy level diagram of the device to measure doping induced injection barrier reduction. The device consists of two identical electrodes with the workfunction $W = 4.5\,\text{eV}$ and two organic layers: the DIL and the hole blocking layer right to it. Figure 5.1a: The host IP E_H^{IP} is indicated by the light red beam with a width indicating the energetic disorder σ_H^{IP}. Analogously, the dopant EA with disorder σ_D^{EA} is shown by the blue beam. Figure 5.1b: After activation of the host–dopant pairs free charge carriers (here holes) are ejected from the DIL into the anode, leaving a negative net charge in the organic layer and causing an upward shift of the energy levels, reducing the injection barrier. The energy levels are shifted until the tail states of the host IP reach the Fermi level of the electrodes.

low doping concentrations there are not enough dopants and thus free charge carriers to achieve Fermi level alignment (ΔE_{IB} at $\approx 0.2\,\text{eV}$). High doping concentrations lead to a large reduction of the injection barrier and thus good Fermi level alignment even for large initial injection barriers.

Besides the doping concentration, this part investigates the effect of the layer thickness (with constant doping concentration) on the injection barrier. Figure 5.3 shows ΔE_{IB} at different doping concentrations plotted against the layer thickness. At lower doping concentrations (1 % to 3 %), the layer thickness leads to a significant increase in ΔE_{IB}. At a doping concentration of 1 %, a high layer thickness leads to ΔE_{IB} from 0.1 eV to almost 0.5 eV. With increasing doping concentration, this effect becomes steadily weaker to the point where it becomes negligible: at 7 % and 10 % the voltage drop does not increase with the layer thickness. At a layer thickness of 15 nm, the voltage drop is approximately 0.5 eV for all doping concentrations, with a clearly visible offset especially between the 10 % curve and the others. An explanation for the offset could be the

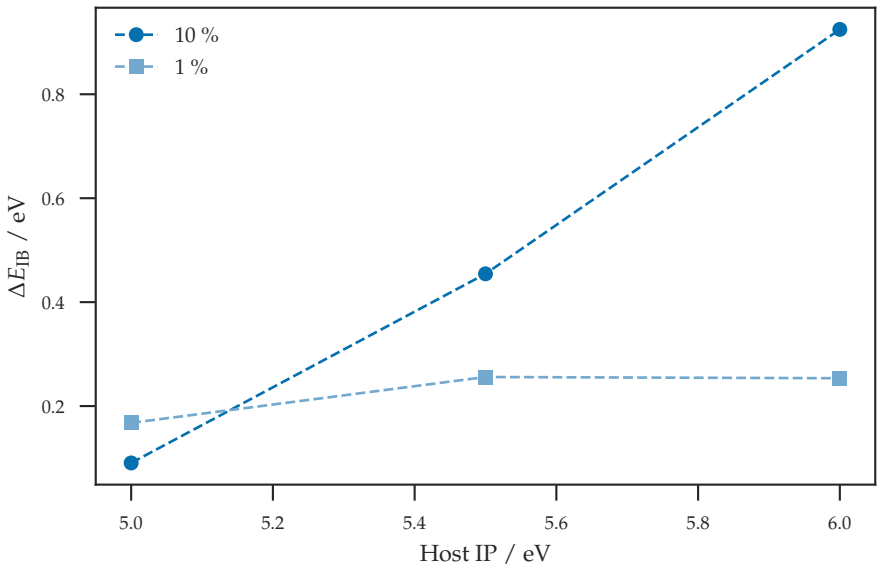

Figure 5.2: Injection barrier reduction at different host ionization potentials and doping concentrations. The reduction of the injection barrier ΔE_{IB} is plotted against the host IP. The squares (dots) depict a doping concentration of 1 % (10 %). At a host IP of 5.0 eV, the observed ΔE_{IB} for 10 % doping concentration is smaller than for 1 % which appears unexpected. However, this can be explained by considering the fact of a doping induced increase of the energetic disorder. For small initial injection barriers, the broadening of the energy levels leads to an overlap between the tail states and the electrode Fermi level, which in turn prevents further energy alignment. Nevertheless, the difference in ΔE_{IB} is relatively small. For larger host IPs, ΔE_{IB} remains almost constant at 1 % doping concentration which can be explained by the fact that not enough dopants and thus free charge carriers are available to foster Fermi level alignment. At 10 % doping concentration, a significant increase in ΔE_{IB} is observed, which is explained by the presence of sufficiently enough charge carriers.

finite size effect: the site energy levels follow a Gaussian distribution so that the probability for host sites with tail-state energies is lower for high doping concentrations. Thus, if the tail-states are truncated, a higher energy shift is required to achieve Fermi level alignment which results in larger voltage drops in the order of the energetic disorder. These results imply, that the tendency of the DIL to align with Fermi level depends on the number of intrinsically free charge carriers and thus on the number of dopants present. To increase the number of free charge carriers, there are two possibilities: increasing a) doping concentration or b) the layer thickness of the DIL.

5.1.2 *Study of the current density–voltage characteristic at different doping conditions*

The second part of this section investigates how DILs affect the transport properties in OLED devices. For this purpose a modified device is used, in which the hole blocking layer is replaced by a HTL with the same energy levels as the host material in the DIL and a small energetic disorder of $\sigma_{\mathrm{H}}^{\mathrm{IP}} = 0.07\,\mathrm{eV}$, a common value for good hole transport materials [131]. Figure 5.4 shows the energy diagram of this device with an applied electric field of $0.06\,\mathrm{V\,nm^{-1}}$ corresponding to an applied voltage of 2.4 V. With a doping concentration of 0.1 % (fig. 5.4, top panel), Fermi level alignment is not achieved, which can be seen from the large injection barrier of the anode and DIL. As already shown in figs. 5.2 and 5.3, larger doping concentrations (fig. 5.4, middle and bottom panel) allow the reduction of the injection barrier until Fermi level alignment is reached.

Without doping, the applied voltage drops evenly over the device. If the doping concentration is large enough, no voltage drop occurs in the injection layer, since the field is compensated for by the newly acquired free charge carriers. As a consequence, the applied voltage must drop in the neighbouring insulation layer. At a doping concentration of 0.1 %, the energy cross section in the DIL has a strong slope, indicating a voltage drop here (fig. 5.4, top panel). This slope is strongly reduced at 1 % doping concentration and the voltage drop in the HTL increases (fig. 5.4, middle panel). At a doping concentration of 10 % the energy levels in the DIL are flat and the entire voltage drops in the HTL (fig. 5.4,

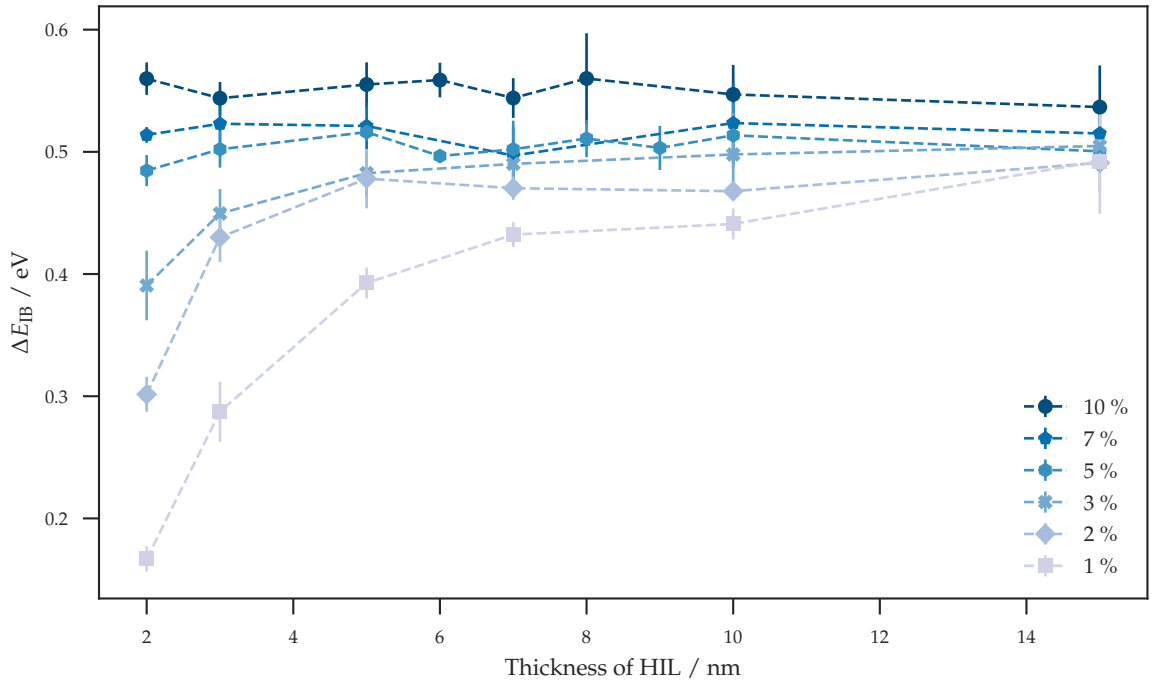

Figure 5.3: Effect of layer thickness on the ΔE_{IB}. At a given doping concentration, the thickness of the DIL controls ΔE_{IB}. While the effect of layer thickness is significant at low concentrations (1 %–3 %), ΔE_{IB} at large doping concentration remains almost constant with increasing layer thickness. The weak variation of ΔE_{IB} at doping concentrations of 5 %–10 % is due to the fact that sufficient dopants are already present at low layer thicknesses to provide enough charge carriers for Fermi level alignment. A direct implication of the dependence of ΔE_{IB} on the total number of dopants is that, in addition to the doping concentration, the layer thickness of the DIL can also be considered as a parameter for the reduction of the injection barrier. At maximum layer thickness, ΔE_{IB} converges to a value of about 0.5 eV, with an offset between the doping concentrations.

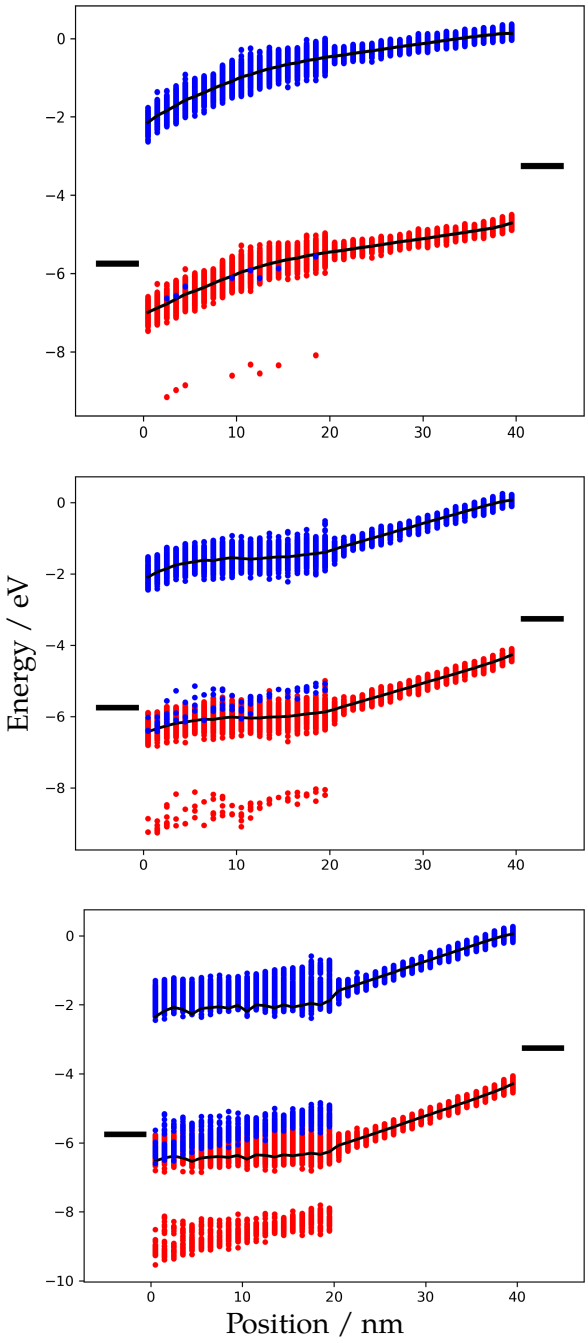

Figure 5.4: Energy diagrams of the test device for conductivity simulations. The black bars on both ends of the devices represent the Fermi level of the electrodes. Each red and blue dot illustrate the IP and EA, respectively, of a single site. Top: With a doping concentration of 0.1 % no Fermi level alignment is achieved. Middle: With a doping concentration of 1 %, the injection barrier is significantly smaller compared to the low doping case. Bottom: Fermi level alignment is accomplished at a large doping concentration of 10 %.

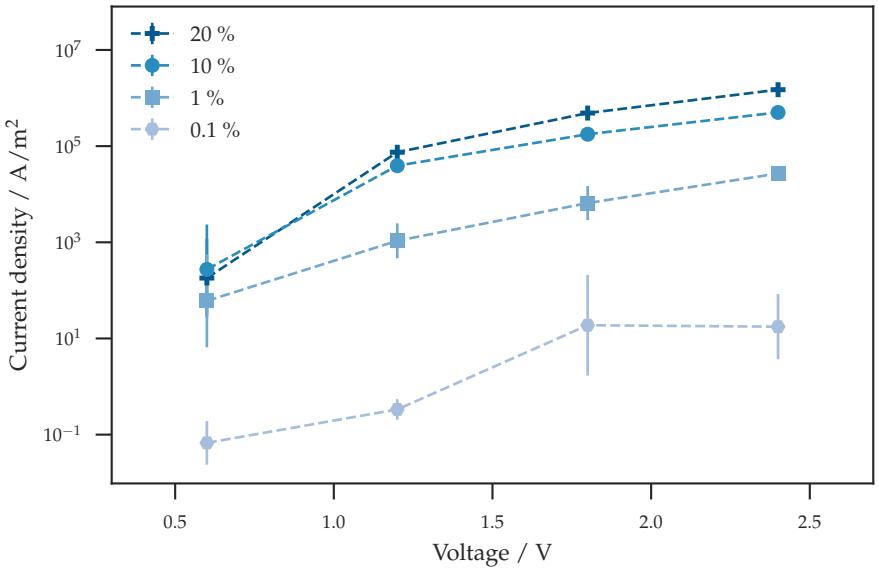

Figure 5.5: *J–V* characteristics at different doping concentrations. The current density is plotted against the applied voltage. At a low doping concentration of 0.1 % the current density is significantly smaller than for a doping concentration of 1 %. Higher doping concentrations (10 %) lead to a further increase of the current density, while the difference between 10 % and 20 % is relatively small, suggesting saturation of the doping effect on the conductivity. The results here are in line with the energy diagrams in fig. 5.4.

bottom panel). The main interested lies in the *J–V* characteristics and their dependence on the doping concentration.

Figure 5.5 shows the *J–V* curve at different doping concentrations. The current density increases by several orders of magnitude when increasing doping concentration from 0.1 % to 1 %. With doping concentrations of 1 % to 10 % the increase in current density is less strong. For 10 % to 20 %, there is only a minor increase which indicates a saturation of the doping induced impact on the current density.

Mesta et al. [36, 159] assumed complete Fermi level alignment and a sufficiently large number of free charge carriers in the doped layers, allowing treatment of the DILs implicitly as electrodes (referred to as *effective anode* in the following). To test the validity of this approximation, additional simulations with effective anodes are carried out by replacing the DIL with an effective anode with a workfunction equal to the IP of the host material. The resulting *J–V* curves are depicted in fig. 5.6. Even

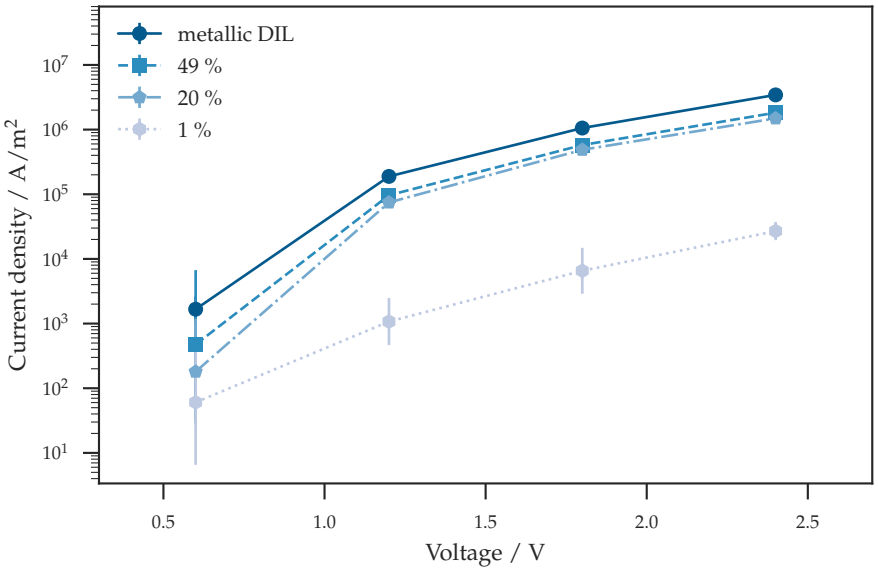

Figure 5.6: *J–V* characteristics of devices with explicit DIL and medium to large doping concentrations (1 %, 20 % and 49 %) and a device where the DIL is approximated by an electrode with appropriate work function (*effective anode*).

at very large doping concentrations of 49 %, replacing the DIL with an effective anode leads to an overestimation of the current density by a factor of 2 to 5. Going towards single-digit doping concentrations, more relevant for OLED stacks, the effective anode leads to an overestimation of the current density by a factor of 20 to 100 and an increasing deviation of the field-dependence.

As seen in fig. 5.2, a sufficiently large doping concentration can achieve Fermi level alignment even with large injection barriers. This part benchmarks the effect on device conductivity, a property of great interest in practical work. For a given electrode workfunction, the host IP determines the initial hole injection barrier before host–dopant ionization leads to Fermi level alignment. In fig. 5.7, the current density is plotted against the doping concentration at different host IPs. At a low doping concentration (0.1 %), the current density for host materials with smaller IP ($E_{\mathrm{H}}^{\mathrm{IP}} = 5.0\,\mathrm{eV}$ to $5.5\,\mathrm{eV}$) is 8 to 10 orders of magnitude larger than for the host with $E_{\mathrm{H}}^{\mathrm{IP}} = 6.0\,\mathrm{eV}$. At a doping concentration of 1 %, the very broad gap between the current densities narrows significantly. With a further increase of the doping concentration, the host IP no longer plays a role, since the initial injection barriers are almost completely

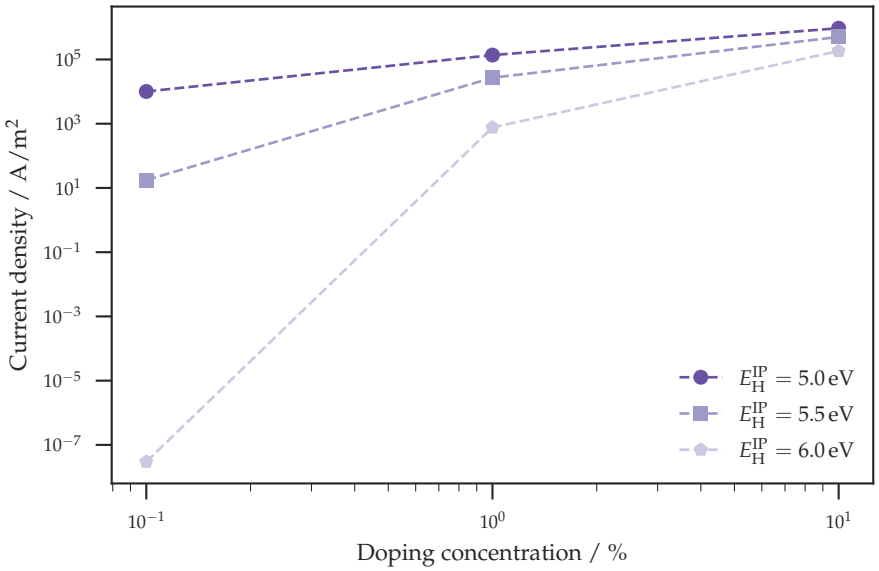

Figure 5.7: Current density as a function of the doping concentration and host IPs. The relation between the IP of the host materials and the anode workfunction determine the initial hole injection barrier. At small doping concentrations (0.1 %) the current density for the host material with $E_H^{IP} = 6.0\,eV$ is very small compared to the current densities of the devices with other host materials ($E_H^{IP} = 5.0\,eV$ to $5.5\,eV$). A doping concentration of 1 % increases the current density of the device with $E_H^{IP} = 6.0\,eV$ by 9 orders of magnitude. The current enhancing effect is much weaker for the devices with lower initial injection barriers. The host materials IP plays a minor role for a large doping concentration (10 %) due to achieved Fermi level alignment even for the $E_H^{IP} = 6.0\,eV$ host material.

eliminated for all three cases. It is worth pointing out, that for the host material with $E_H^{IP} = 6.0\,eV$ (large initial injection barrier 1.5 eV), the current density increases by approximately 12 orders of magnitude by increasing the doping concentration from 0.1 % to 10 %. At these large doping concentrations, high current densities are achieved regardless of the host material used. The significant impact on the current density stems from two effects: a) the increase of mobile charge carriers due to doping activation and b) the resulting reduction of the hole injection barrier.

5.1.3 *Discussion*

Using the parametric device allows varying a wide range of critical parameters, such as host IP or dopant concentration to provide insights into the interplay of material parameters and layer configurations. In fabricated devices, the injection barrier is determined by the selection of the host and electrode material. Even with these parameters predetermined, simulations can help find an ideal dopant material and optimize the doping concentration to achieve Fermi level alignment and charge balance in the EML.

This section shows that the kMC model is conceptually well suited to study the influence of DILs on the device properties. The results show that by increasing the doping concentration, Fermi level alignment can be achieved even with large injection barriers. In addition, an enlarged thickness of the DIL (with constant doping concentration) fosters Fermi level alignment. The effect of doping on current density is of particular practical interest. Properly optimized dopants and doping concentration can cause the current density to increase by several orders of magnitude and allow tuning the charge carrier balance in the device.

The approximation of cubic structures in this section is not severe, because the off-diagonal disorder is captured by the distribution of hopping matrix elements. When applied to novel materials, extending the systems from cubic lattice to realistic structures is straightforward. Accurate EAs and IPs can be obtained using *ab initio* calculations [134] and the Coulomb interaction of host–dopant pairs can be computed quantum-mechanically, as demonstrated in section 5.2. In combination with an *ab initio* parametrization, this work can help to accelerate the search for ideal host–dopant materials in DILs and optimal device architectures.

5.2 SIMULATING DOPED INJECTION LAYERS BASED ON MICROSCOPIC PROPERTIES

The study presented in this section was published in collaboration with Symalla et al. [A8] and presented in collaboration with Neumann et al. [P4] and Symalla et al. [P5].

To enable the analysis of microscopic processes, such as doping, on device performance based solely on quantities derived from first principles, this study utilizes the seamless bottom-up multiscale modelling approach discussed in chapter 3 to compute material properties for the kMC simulation, replacing the parametric model in section 5.1.

Prior studies by Fediai et al. [154, 155] have shown that doping efficiency is determined by the interplay between intrinsic and doping-induced material disorder, the position of the doping induced energy levels and Coulomb interaction. One shortcoming in these studies is the assumption of classical Coulomb interaction between the charged molecules and a homogeneous distribution of energy levels. This study expands this model by considering real material morphology and computing the distribution of the Coulomb interaction between dopant–host pairs as a function of their distance on a quantum-mechanical level.

This approach goes beyond recent works, where the host–dopant interaction has been only computed for a single host–dopant pair [18]. Instead, we explore the dependence of the host–dopant interaction for various intermolecular distances and orientations in the morphology. This step is crucial and far from trivial from a computational point of view: As the strength of the Coulomb interaction in the integer charge transfer complex determines the ionization probability and the number of mobile charge carriers (i.e. the doping efficiency [160]), the correct (molecule-specific) distribution of this quantity (depending on the host–dopant distance) is the critical parameter for *in-silico* design of the efficient dopant–host pairs.

The kMC model (section 3.4) is used to dynamically simulate the charge transfer between dopant and host (illustrated in fig. 5.8) and charge carrier dynamics for the analysis of the DIL consisting of α-NPD doped with 2,3,5,6-Tetrafluoro-7,7,8,8-tetracyanoquinodimethane (F4TCNQ). For each host–dopant pair, this charge transfer depends on the CT activ-

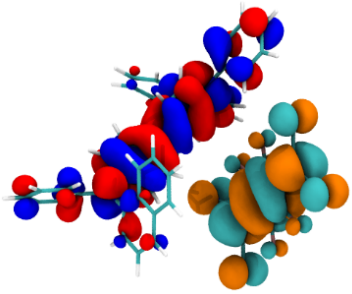

Figure 5.8: Orbitals of a host–dopant pair: An electron is transferred from the HOMO of the host (red/blue) to the LUMO of the dopant, creating a hole on the host.

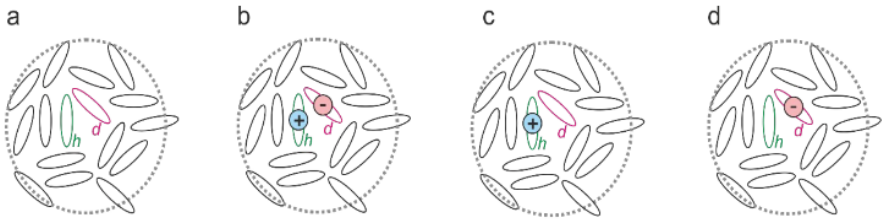

Figure 5.9: States of the host–dopant pair required to compute the binding energy of a dopant–host CT-state: (a) neutral host–dopant pair (b) activated host–dopant pair (c) charged host (d) charged dopant.

ation energy ΔE_{act}, the energy difference between activated (fig. 5.9b) and neutral (fig. 5.9a) host–dopant pair in an uncharged environment, and an additional dynamic contribution of the Coulomb interaction with charges in the vicinity. Due to systematic error in the computation of absolute energies with DFT, ΔE_{act} cannot be computed directly. Instead the Coulomb binding energy of host–dopant pairs

$$V_C = \Delta E_{\text{act}} - \left(E_{\text{IP}}^{\text{host}} - E_{\text{EA}}^{\text{dopant}} \right) \tag{5.3}$$

is computed, for which the systematic DFT error cancels out. IP of hosts (fig. 5.9c) and EA of dopants (fig. 5.9d), for which the same DFT error exists, but is to a large extend systematic, are corrected separately.

To compute distance dependent distributions of the coulomb binding energy $V_C(r)$, as well as distributions for host IP and dopant EA energies, a morphology of the DIL is generated virtually with atomistic resolution using the Deposit protocol. To create this mixed morphology, 1500 molecules (95 % α-NPD, 5 % F4TCNQ) are deposited into a box of 80 Å × 80 Å × 200 Å with PBC in x- and y-direction in 32 parallel SA

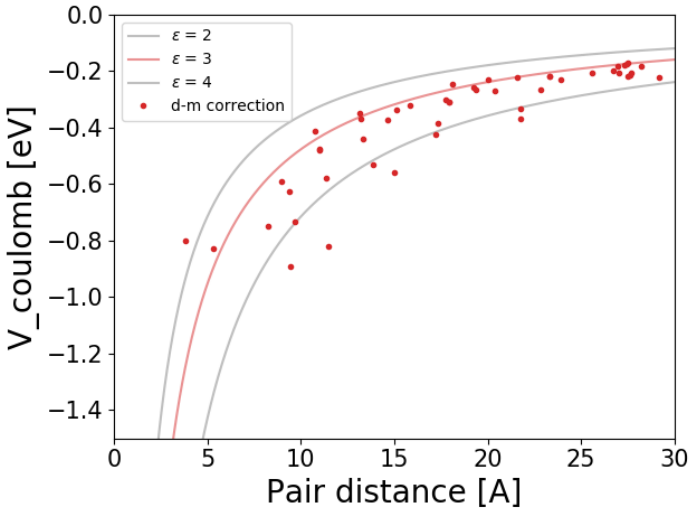

Figure 5.10: Coulomb binding computed for 50 host–dopant pairs in the morphology.

cycles starting at an artificially high temperature (4000 K) and cooling to room temperature (300 K) in 130 000 MC steps. Using QP, V_C, $E_{\mathrm{IP}}^{\mathrm{host}}$ and $E_{\mathrm{EA}}^{\mathrm{dopant}}$ are computed for 50 host–dopant pairs in the morphology while taking into account the response of molecules in the environment purely on a quantum-mechanical level.

In the kMC simulation, values of these distributions are drawn to compute the activation energy for each host–dopant pair of an extended morphology (25 nm × 25 nm × 25 nm) to dynamically simulate the charge transfer process and charge carrier dynamics in the DIL.

As explained above, QP is used to compute energy levels of host (IP) and dopants (EA) and a distribution of the coulomb binding energy. Averaged over 50 molecules, this resulted in $E_{\mathrm{IP}}^{\mathrm{host}} = 5.44\,\mathrm{eV}$ and $E_{\mathrm{EA}}^{\mathrm{dopant}} = 4.84\,\mathrm{eV}$. Note that the host IP is approx. 100 meV lower compared to the usual IP of α-NPD due to the presence of F4TCNQ in the thin film. The distance dependent distribution of the coulomb binding energy $V_C(r)$ computed for 50 host–dopant pairs with different relative orientation, is depicted in fig. 5.10.

The computations show that most electron hole pairs are bound by up to 0.9 eV, hindering CT-states dissociation. Notably, such energies at these distances correspond to a low permittivity of approximately 2.0 in a

classical model. This is in contrast to ϵ between 3 to 4 at larger distances usually assumed for bulk organic semiconductors. Further, a large spread of energies induced by different relative orientations of pairs is found. This spread underlines the approach of using a distribution in contrast to use single value per distance.

In addition to the Coulomb binding energy, the dissociation of an electron–hole pair after ionization of the dopant is determined by the transport levels (in the case of hole-doping the transport levels of holes (IP)) of the surrounding host molecules. Previous studies have shown that the presence of guest molecules in organic films can shift these transport levels by up to 0.5 eV [161].

To estimate the impact of this effect in doped systems, IP distributions of 50 molecules are computed in an α-NPD morphology doped with F4TCNQ in dependence of the distance to the nearest dopant using QP, i.e. taking into account the unique electrostatic environment of each molecule. The results are displayed in fig. 5.11. According to the linear fit, IP levels of host molecules near dopants are lower than the average value of −5.44 eV computed above. This indicates that dopants not only globally but especially locally lower the transport levels of host molecules. This is in line with the observed increase of energy disorder in α-NPD from approximately 100 meV to 150 meV when doped. As holes tend to go up in energy, this effect partially compensates Coulomb binding energy, improving charge separation.

Using the distribution of the coulomb interaction of fig. 5.10 along with computed energy levels dynamic kMC simulations are conducted to compute the fraction of activated dopants, Fermi level, conductivity activation energy, number of free charge carriers and conductivity in the DIL. To extract the conductivity activation energy $E_{\mathrm{act,c}}$, the temperature dependence of the conductivity is simulated. For activated transport an exponential increase of conductivity can be observed with increasing temperature, as charge is thermally propelled from a bound state to the charge transport level.

$$J \propto \exp\left(\frac{E_{\mathrm{act,c}}}{k_{\mathrm{B}}T}\right) . \tag{5.4}$$

Measuring the slope of the conductivity versus the inverse temperature allows determination of this conductivity activation energy.

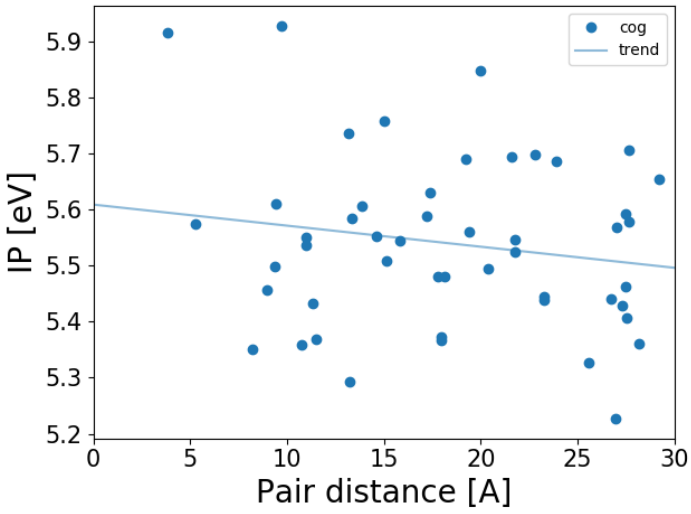

Figure 5.11: Distribution of host IP levels in dependence of the distance to the nearest dopant.

For disordered materials, the hole transport level $E_{\text{transport}}$ is the energy around which a transport percolation path can be established and can be defined as the difference between Fermi level and transport activation energy:

$$E_{\text{transport}} = E_F - E_{\text{act,c}} \tag{5.5}$$

Temperature dependent conductivity in the α-NPD:F4TCNQ sample is depicted in fig. 5.12. From the slope a transport activation energy of 180 meV is derived. The fraction of activated host–dopant pairs (pairs for which a charge is transferred from dopant to host) is 91 %.

The Fermi energy is determined by extracting the energy at which hole and electron occupation probability is equal [154]. For the doped system, the hole levels are given by the IP distribution of the neutral hosts in the dynamic environment of all charges and the electron affinity distribution of the host molecule cations labelled by EA_0^+, which corresponds to hole energies. Figure 5.13 shows the DOS of α-NPD molecules in the doped layer. From this a Fermi energy of

$$E_F = -4.46\,\text{eV}, \tag{5.6}$$

is derived, resulting in a charge transport energy of

$$E_{\text{transport}} = -4.65\,\text{eV}. \tag{5.7}$$

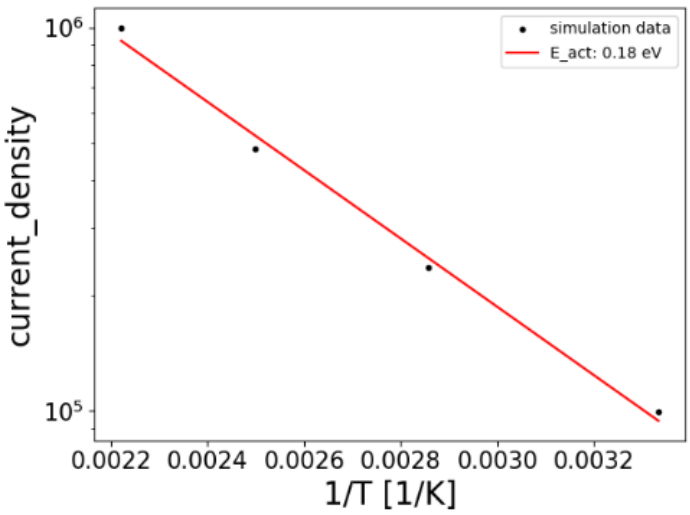

Figure 5.12: Temperature dependent computation of conductivity of α-NPD doped with 10 % F4TCNQ results in a conductivity activation energy of 180 meV.

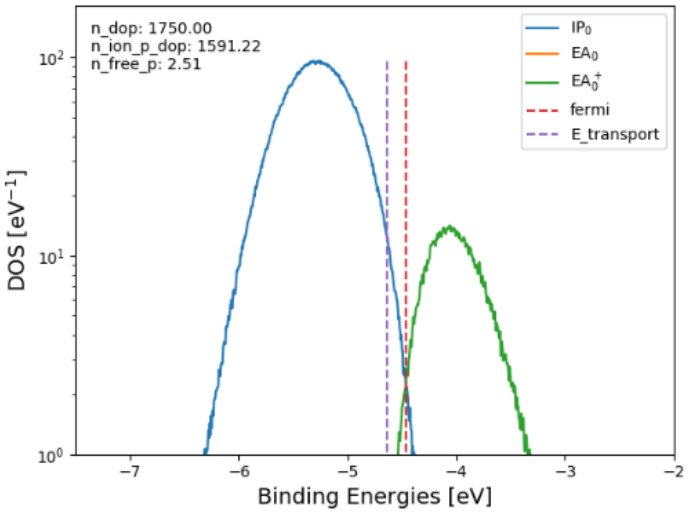

Figure 5.13: DOS of the HOMO levels of neutral host molecules (−IP) in their dynamic environment, and hole (EA_0^+) levels.

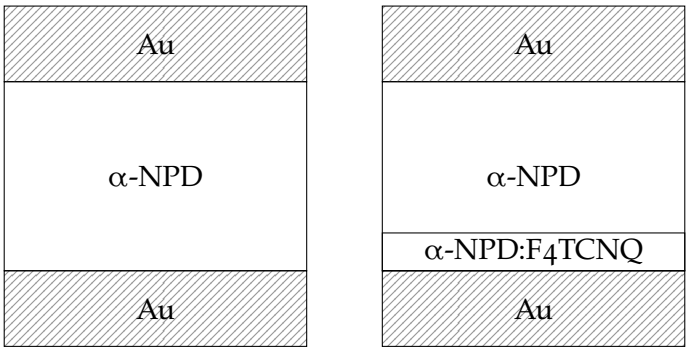

Figure 5.14: Schematic diagrams of the devices measured by Gao et al. [156]. Left the undoped device and right the same device with the first 8 nm of α-NPD doped with 1 % F4TCNQ.

To validate the model, this study uses the electronic properties of α-NPD and F4TCNQ computed in this section to simulate devices fabricated and measured by Gao et al. [156]. Specifically, an undoped device comprising of α-NPD and a device (labelled 'partially doped') with the first 8 nm of α-NPD doped with 1 % F4TCNQ (0.5 wt%), depicted in fig. 5.14 (left and right panel, respectively).

For the kMC simulation, the thin-film morphologies are expanded to amorphous structures with a base area of 25 nm × 25 nm. The electrode workfunction is set to $W = 4.4\,\text{eV}$ according to the injection barrier of $\Delta E_{\text{IB}} = 1\,\text{eV}$ [156]. Other parameters are set as computed in this section.

Each system is simulated with an applied bias of 13.6 V and 16 V. Computed *J*–*V*s in both systems (fig. 5.15) agree well with the data measured by Gao et al. [156]. The simulations slightly underestimate the *J*–*V* characteristics by roughly the same amount in both systems, reproducing the current density increase by adding F4TCNQ very well. These results highlight the high quality of both the kMC model and the electronic properties computed with the multiscale workflow.

Additionally, these simulations allow screening of relevant parameters via computation, e.g. varying doping concentrations to find the optimal doping concentration for charge transport. To conserve computing resources, amorphous structures similar to the partially doped device with a reduced HTL thickness of 32 nm are used for the screening. Structures are generated for doping concentrations d of 0.1 %, 0.3 %, 0.5 %,

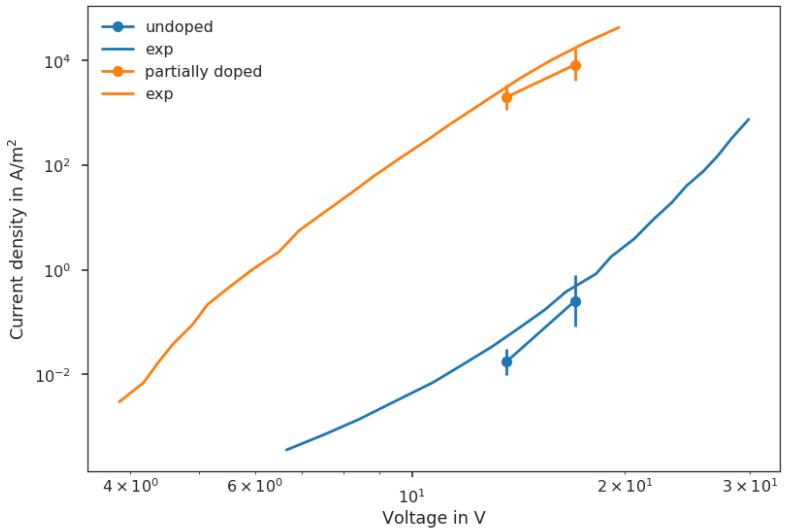

Figure 5.15: Simulated *J*–*V* characteristics of the undoped and partially doped devices compared with the measurements by Gao et al. [156].

0.8 %, 1 %, 1.2 %, 1.5 %, 2 %, 5 % and 8 %. *J*–*V*s are computed from simulations at an applied bias of 4 V. These *J*–*V*s (fig. 5.16) show a strong increase in current density at an increase of d from 0.1 % to 0.3 % and a decline around 2 %. The simulations therefore show an optimal doping concentration for efficient charge transport in this system around $d = (1.0 \pm 0.5)$ %.

The simulations can help gain insight into the devices and explain the cause of this plateau. The energy diagrams in fig. 5.17 show the energy levels at doping concentrations of 0.1 %, 0.8 % and 8 %. At 0.1 % the few dopants do not suffice bridge the injection barrier, leading to injection limited currents. A doping concentration of approx. 0.3 % suffices to align Fermi levels. With increased doping concentrations, the DOS in the HIL and at the HIL–HTL interface broaden, apparent in the bottom panel of fig. 5.17, building up an injection barrier from HIL to HTL which hinders transport. The combination of these effects leads to the plateau in current density apparent in fig. 5.16.

This section investigated doping in the system α-NPD:F4TCNQ using kMC device simulations with input derived solely from first principles using a multiscale modelling approach. By computing distributions of

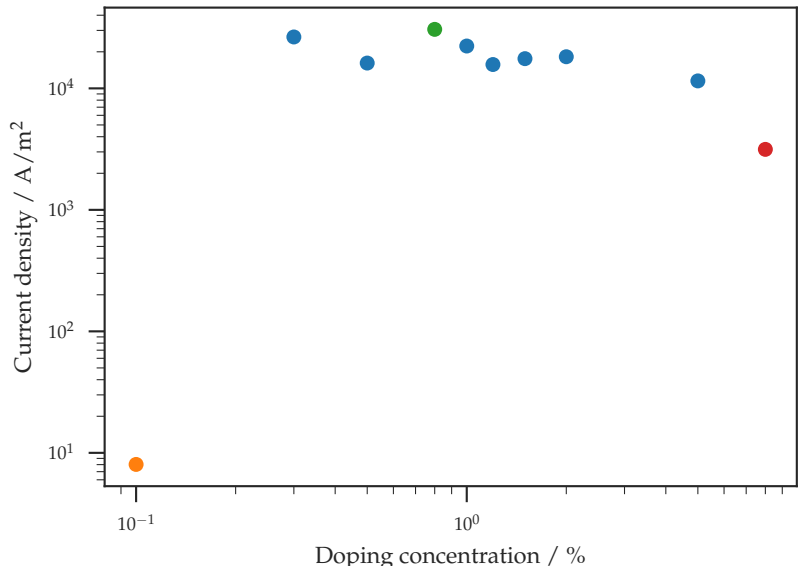

Figure 5.16: Current densities of the partially doped device with varied doping concentrations. As can be seen, the optimal doping concentration for this device lies in the range of 0.3 % to 2 %.

the Coulomb binding energy, host-IP and dopant-EA with the QUANTUMPATCH method on atomistic morphologies, the charge transfer processes between dopant and host molecules are modelled in a digital twin of the doped injection layer. Additionally, the fraction of activated dopants were derived. This computational approach can be used to complement experimental efforts in the design and optimization of organic molecules for doped injection layers, either by screening of potential candidates, or by providing microscopic insight to generate a fundamental understanding and establish structure–function-relationships. An example for this is the relationships between the structure of a given donor–acceptor pair and the Coulomb binding energy, which in turn affects the number of free charge carriers. Such structure–function-relationships can be used to derive design rules for material optimization.

Furthermore, this section illustrates how DILs impact device performance due to Fermi level alignment at the electrodes. These results reinforce the conclusion of the parametric studies in section 5.1, that it is essential to explicitly include DILs in full OLED device simulations in order to provide reliable results.

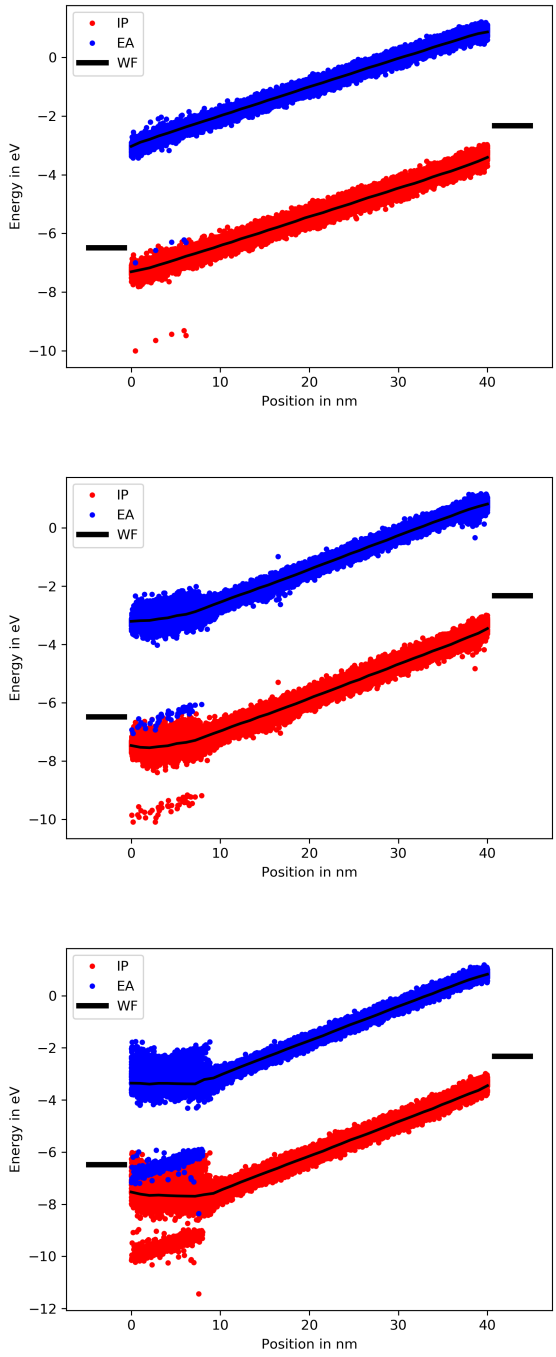

Figure 5.17: Energy cross sections with an applied bias of 4 V and doping concentrations of 0.1 % (top), 0.8 % (middle) and 8 % (bottom) marked in fig. 5.16. From top to bottom the DOS in the doped layer broadens, leading to an increasing injection barrier into the neighbouring hole-transport layer. As can be seen, the doping concentration of 0.1 % does not reduce the injection barrier significantly.

6

DEVICE SIMULATIONS OF FULL OLED STACKS

Despite their high level of technological readiness, the full potential of OLEDs cannot be exploited due to the lack of highly efficient, durable OLED devices emitting in the deep-blue colour range. There are multiple approaches to overcome this bottleneck e.g. with novel classes of materials, such as thermally activated delayed fluorescence (TADF) or phosphorescent blue emitters, or complex emission systems, e.g. hyperfluorescence and co-emission, which resulted in devices with improved efficiencies [22–26]. However, despite years of R&D, industrial devices including blue emission still suffer from limited efficiency and lifetime, especially at high luminance [22–25, 27, 28].

The design of performant and therefore enduring devices requires the fine calibration of a multitude of microscopic processes. As these processes are triggered and balanced by molecular properties in a quite entangled fashion, the prediction of how single molecular properties impact device performance is challenging, rendering the elimination of performance bottlenecks via experimental trial and error a time-consuming and costly task. The multiscale workflow presented in chapter 3 bridges the gap between fundamental chemistry and device design and allows the analysis how specific molecular properties impact device performance. Furthermore, the explicit simulation of microscopic processes enables the systematic investigation of microscopic performance bottlenecks to enable rational design of OLED materials and devices [A9, A10, 29, 30].

Specifically, full *ab initio* simulations, i.e. without parametrization with experiments, have been applied to address individual aspects of OLED design, such as charge transport[A5, A6, 34, 37, 38], doped injection layers [A4, A8] or excitonic quenching [39]. Beyond the investigation of such isolated aspects in OLEDs, the simulation of full OLED stacks is a promising approach towards design of balanced and performant devices. However, microscopic simulation of charge and exciton dy-

namics in complete OLED stacks to date was limited to models parametrized with experimental data [36, 40].

This chapter combines device simulations from chapter 4 with the DIL model from chapter 5 to simulate a modern multilayer OLED *de novo*, starting with the computation of microscopic parameters for all materials employed in a modern multilayer OLED in section 6.1. Section 6.2 discusses a limitation of the kMC model with large variations of hopping rates, rendering a simulation of the entire OLED stack infeasible. Two solutions are presented, which facilitate *de novo* simulations of OLED stacks: First, using computed material parameters, augmented with transport characteristics of individual layers computed with the kMC model, to parametrize a DD model to calculate device characteristics of the OLED stack on the continuum scale (section 6.3). Secondly, by developing a method to effectively decouple regions with frequent events from regions with the infrequent events of interest (section 6.4). Specifically, using this method, the DILs are decoupled from the inner part of the OLED to efficiently simulate exciton dynamics of the OLED (section 6.5).

6.1 MICROSCOPIC PARAMETRIZATION

The study presented in this section and section 6.5 is being prepared for publication [A1].

The red OLED stack studied here was fabricated and measured by the group of Tung-Huei Ke at the Interuniversity Microelectronics Centre (IMEC) within the EXTended Model of Organic Semiconductors (EXTMOS) project. At first, all material parameters are calculated *ab initio* using the multiscale workflow discussed in chapter 3. These data are later used to compute device characteristics using the semi-classical continuum DD model implemented in the technology computer-aided design (TCAD) software in section 6.3 and the mesoscale kMC device model in section 6.5.

The layout of the red OLED stack is depicted in fig. 6.1. The stack consists of an ITO anode, a 10 nm HIL of NPB doped with 5 % hexafluorotetracyanonaphthoquinodimethane (F6TCNNQ), a 70 nm HTL of NPB, a 20 nm EML of NPB doped with 10 % of the red phosphorescent emitter

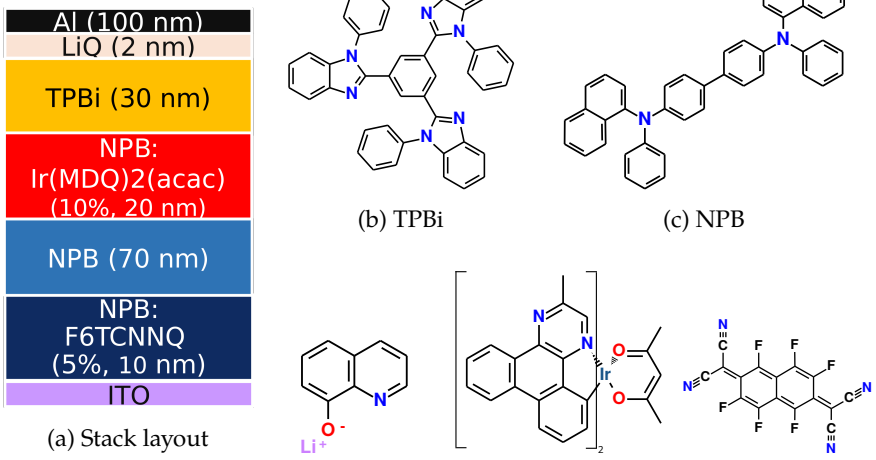

(a) Stack layout (b) TPBi (c) NPB

(d) LiQ (e) $Ir(MDQ)_2(acac)$ (f) F6TCNNQ

Figure 6.1: Layout of red OLED stack (variant *B*) simulated *de novo* in this work (fig. 6.1a) and the molecules comprising the stack (figs. 6.1b to 6.1f). Stack variant *A* resembles variant *B* with the thickness of the electron-transport layer reduced from 30 nm to 10 nm.

Bis(2-methyldibenzo[f,h]quinoxaline)(acetylacetonate)iridium(III) ($Ir(MDQ)_2(acac)$), a 30 nm ETL of TPBi with a 2 nm EIL (8-Hydroxyquinolinato)lithium (LiQ) and an Al cathode. For each layer 2000 molecules are deposited into a 90 Å × 90 Å × 300 Å box with PBC in x- and y direction. Each molecule samples the morphology surface in 130 000 MC steps starting from an artificially high temperature $T_{\text{initial}} = 4000\,\text{K}$ to room temperature $T_{\text{final}} = 300\,\text{K}$, parameters proven sufficient for sampling medium to large molecules [90, 94]. To improve sampling, 32 SA cycles are run in parallel.

The radial distribution function (RDF) of the amorphous morphology representing each layer in the device are depicted in fig. 6.2. As can be seen, the RDFs of NPB in the pure HTL and as host material in the DIL and EML share the same features without any significant differences. The RDF NPB features two distinct peaks and reaches the plateau at $r \approx 15\,\text{Å}$, while the RDF of TPBi peaks into a broad plateau and reaches unity at $r \approx 17\,\text{Å}$. The RDFs of both $Ir(MDQ)_2(acac)$ and F6TCNNQ fluctuate around $g(r) = 1$ in the range of $7\,\text{Å} \gtrsim r \gtrsim 20\,\text{Å}$, with RDF of F6TCNNQ fluctuating far stronger. The difference in molecule size is reflected in the onset $g(r') > 0$ of the RDFs. While F6TCNNQ is smaller and $Ir(MDQ)_2(acac)$ is comparable in size to NPB, $r'_{\text{NPB}} \ll r'_{\text{F6}} \approx r'_{\text{IrMDQ}}$ due to

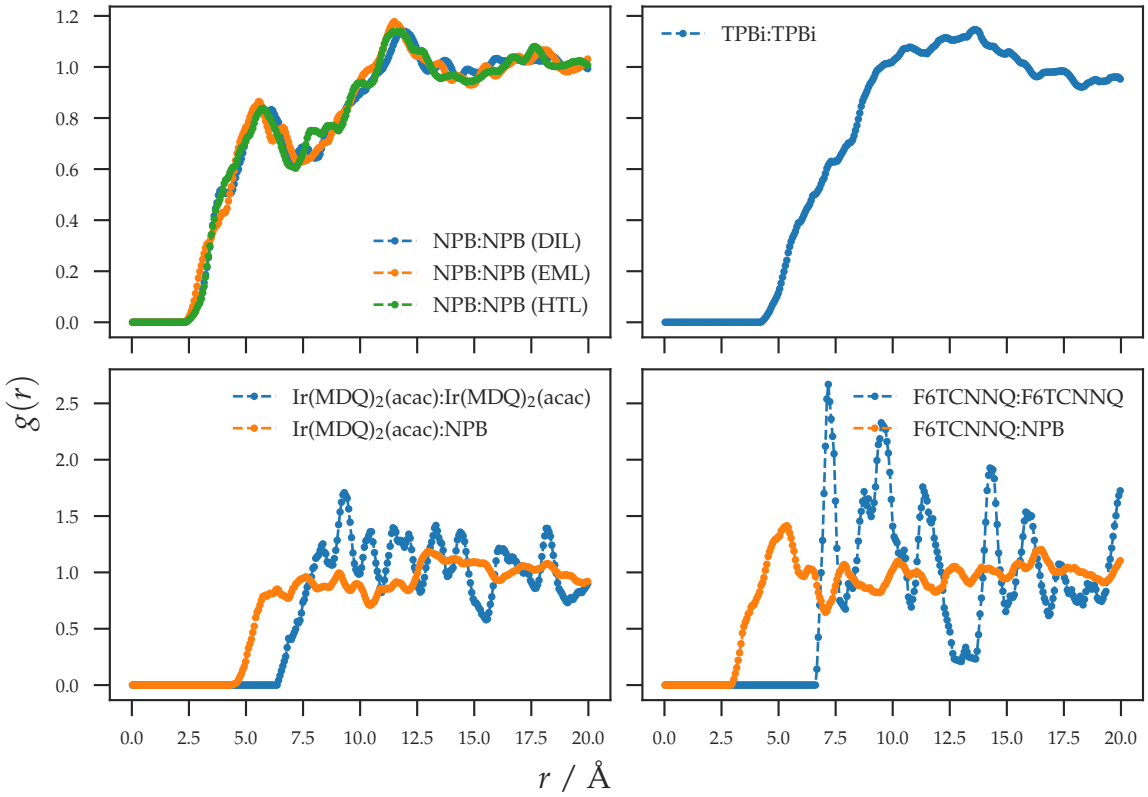

Figure 6.2: Radial distribution function of the molecular pairs present in the amorphous morphologies representing each layer deposited using the DEPOSIT protocol.

the low concentration of 5 % and 10 %, respectively. The mixed RDFs of each emitter and NPB as neighbour – to some degree – resolve the issue with low concentrations and show the expected $r'_{\text{F6:NPB}} < r'_{\text{IrMDQ:NPB}}$.

Electronic structure properties, namely energy disorder σ, electronic couplings J_{if}, reorganization energies λ_{ij}, IP E_{IP} and activation energy E_a, are computed for a subset of molecules in their converged unique electrostatic environments in the deposited thin-film morphologies using the QP method.

The energy disorder σ is computed from the equilibrated orbital energies of the innermost 200 molecules as the standard deviation of energy differences ΔE_{ij} of all pairs of neighbouring molecules i and j within each layer. The distributions of ΔE_{ij} for all materials are depicted in fig. 6.3, the resulting σ are listed in table 6.1. The HOMO disorder

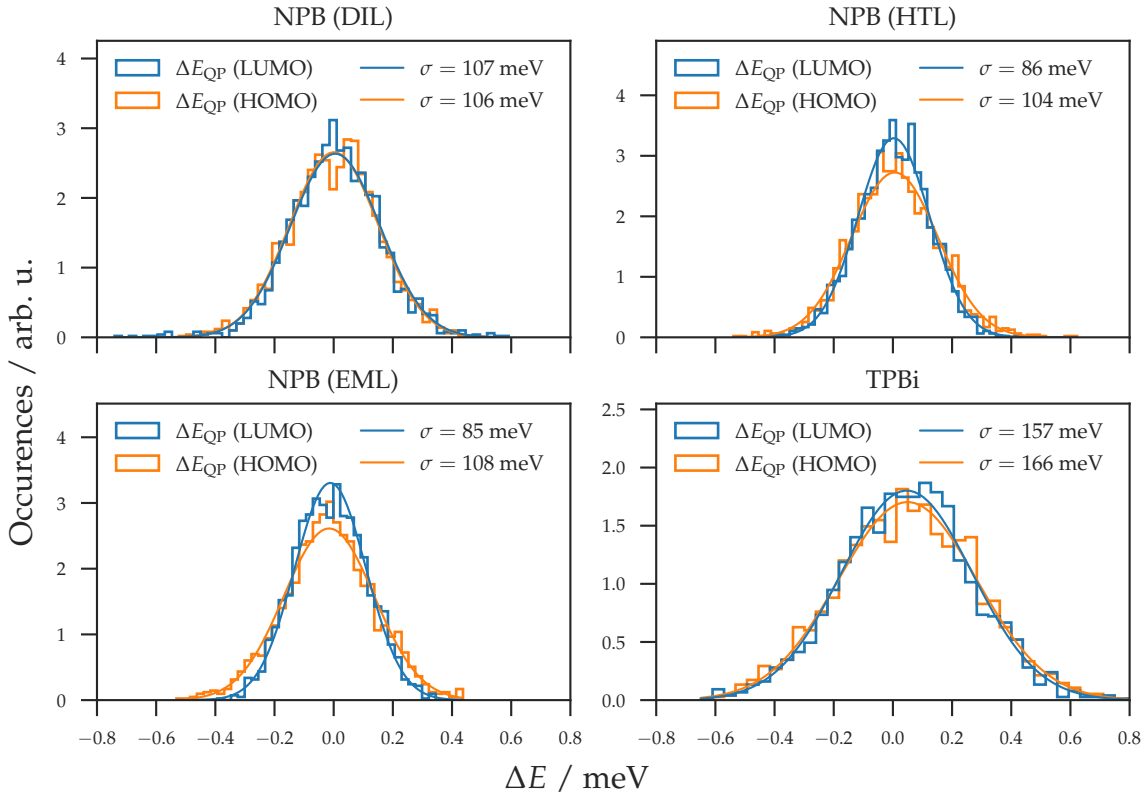

Figure 6.3: Distribution of ΔE_{ij} computed with the QUANTUMPATCH method, Gaussian fit and resulting disorder σ for the transport molecules in different layers of the OLED stack.

σ_{HOMO} of NPB in the pure and mixed morphologies is quite similar, while σ_{LUMO} varies strongly from 85 meV and 86 meV in the EML and HTL morphologies, respectively, and 107 meV in the DIL morphology. As can be seen, σ strongly depends on the guest material and concentration and thus the precise layer structure. Electronic couplings J_{ij} are computed using the Löwdin orthogonalization procedure [95] for HOMO, LUMO and Dexter transfer (eq. 3.4).

Sampling a sufficient number of guest–guest and guest–host pairs for an accurate distribution of electronic couplings in layers with small guest concentrations would require very large morphologies and infeasibly long QP calculations. To solve this problem, electronic couplings are computed in morphologies with an increased guest concentration. All other deposition parameters are set as above. The modified DIL consists of 2000 molecules with a ratio of ¼ F6TCNNQ and ¾ NPB deposited

Table 6.1: Microscopic input, namely the reorganization energy λ, energy disorder σ and transport levels E_{EA} and E_{IP}, for the charge transport simulation computed with the QUANTUMPATCH method.

Layer	Material	λ/meV		σ/meV		E_{EA}/eV	E_{IP}/eV
		elec.	hole	elec.	hole		
DIL	NPB	133[a]	206[a]	107	106	−1.94	5.31
	F6TCNNQ	223	139	127	132	−5.02	7.29
HTL	NPB	133[a]	206[a]	86[a]	104[a]	−1.94	5.33
EML	NPB	133[a]	206[a]	85	108	−1.94	5.23
	$Ir(MDQ)_2(acac)$	265	454	104	97	−2.57	5.53
ETL	TPBi	317[a]	160[a]	157[a]	166[a]	−1.97	6.44
EIL	LiQ	200[b]	200[b]	90[b]	90[b]	−1.35[c]	5.40[d]

[a] Values computed in section 4.1.1.
[b] Common values for small organic molecules.
[c] LEIPS measurement by Yoshida [144] shifted by 0.5 eV to account for LEIPS measuring the onset of the DOS.
[d] Irrelevant for charge transport in this stack.

into a box of 80 Å × 80 Å × 300 Å. Electronic couplings of F6TCNNQ and NPB are computed for pairs of the innermost 200 molecules with an atom–atom distance of less than 7 Å in this modified DIL. The rest of the device is mimicked by 500 molecules of TPBi deposited on top of 700 molecules of 20 % $Ir(MDQ)_2(acac)$ and 80 % NPB in a box of 80 Å × 80 Å × 240 Å. All other electronic couplings are computed for pairs of molecules with an atom–atom distance of less than 7 Å in the innermost 76 Å × 76 Å × 64 Å of this morphology. Dimer DFT calculations are performed using the BP86 functional. The distribution of $J_{ij}(r)$ is depicted in fig. A.6.

Reorganization energies λ_i are computed based on Nelsen's four point procedure [97]. For reorganization energies of NPB and TPBi, the values computed in section 4.1.1 are used. The reorganization energies of F6TCNNQ and $Ir(MDQ)_2(acac)$ are computed in vacuum with constrained dihedral rotations to approximate the effect of the matrix [104]. The λ_{ij} are listed in table 6.1.

IPs are computed as the total energy difference between charged and uncharged state in the relaxed environment for 10 host and 5 guest mo-

lecules within each layer. The values are listed in table 6.1. As is the case with σ, the specific environment influences the IP of NPB, which varies by 100 meV between the NPB in the HTL and EML. EAs are calculated for each material using the hybrid exchange-correlation functional with perturbative second-order correction (B2-PLYP)[162] functional in vacuum with an empirical correction for vacuum EAs $E_{\mathrm{EA}} = 0.8521 \cdot E_{\mathrm{EA}}^{\mathrm{vac}} - 1.91$ fitted to LEIPS measurements by Yoshida [144].

Following eq. 5.3, accurate charge transfer activation energies ΔE_{act} are computed as

$$\Delta E_{\mathrm{act}} = V_{\mathrm{C}} + \left(E_{\mathrm{IP}}^{\mathrm{host}} - E_{\mathrm{EA}}^{\mathrm{dopant}} \right). \tag{6.1}$$

The Coulomb binding energy V_{C}, $E_{\mathrm{IP}}^{\mathrm{host}}$ and $E_{\mathrm{EA}}^{\mathrm{dopant}}$ are calculated for 10 host–dopant pairs using the B2-PLYP functional. The values of E_{EA} are listed in table 6.1.

Singlet and Triplet energies, E_{S_1} and E_{T_1}, respectively, are computed for single molecules in vacuum using the hybrid exchange-correlation functional using the Coulomb-attenuating method (CAM-B3LYP)[163] functional. Triplet lifetimes τ_{T_1} are calculated using relativistic core potentials as implemented in the DALTON [164] DFT package. Dipole transition moments $\vec{d}$ of singlets are computed using time-dependent density-functional theory (TDDFT)[165] and the CAM-B3LYP functional, of triplets using the method of Jansson et al. [31] as implemented in DALTON with the B3LYP functional and Pople split valence basis-set (3-21G)[166–171]. The first 20 excitations from T_1 are computed as possible TTA acceptor states using TDDFT. Cation, anion and triplet excitation spectrum and cation, anion and triplet excitation transition dipole moments are computed for the optimized molecule in vacuum. The non-radiative decay rate is set to $k_{\mathrm{nr}} = 1 \times 10^5\,\mathrm{s}^{-1}$.

Due to the non-covalent bond of LiQ, depositing a realistic morphology is not possible with the presented workflow. As LiQ aids electron injection without taking part in electron transport [172], precise electronic properties for this material are not essential for the device simulation. To this end, $E_{\mathrm{EA}}^{\mathrm{LiQ}} = 1.35\,\mathrm{eV}$ is taken from the LEIPS measurement of Yoshida [144], shifted by 0.5 eV to account for this technique measuring the onset of the DOS. The IP of LiQ is irrelevant for charge transport, as the large hole injection barrier from EML to ETL effectively blocks all holes from leaving the EML. With a thickness of 2 nm and the EAs of TPBi and LiQ favouring electron injection directly into the ETL. As

LiQ does significantly take part in charge transport, energy disorder and reorganization energy are therefore approximated with common values for small molecules, $\sigma = 90\,\text{meV}$ and $\lambda = 200\,\text{meV}$, respectively. Electronic couplings of LiQ–LiQ and LiQ–TPBi pairs are approximated with those of TPBi–TPBi pairs.

6.2 LIMITATIONS IN FULL-STACK KMC SIMULATIONS

To benchmark the validity of the kMC model for a full-stack simulation, small test systems with a base are of 14 nm × 14 nm are generated using the microscopic data calculated in section 6.1. Figure 6.4 shows the charge and move distribution in one of these devices after 20 000 000 kMC steps, a sufficient number of steps to thoroughly sample the device characteristics in e.g. section 4.3. As can be seen, the simulation time is spent almost exclusively on charge movement in the DIL. Only few holes escape the DIL into the HTL and none of those holes travel far into the HTL. The main reason for the slow propagation of the system are the large number of free holes in the DIL with large hopping rates around the ionized dopants, greatly reducing the time evolution per kMC step and thus limiting the simulation to timescales far below those required to observe processes of interest, e.g. exciton creation and decay, without excessive use of computational resources. At this rate, device simulations are not feasible, even for these small test systems.

To overcome this limitation, Mesta et al. [36, 159] treated the DILs implicitly as electrodes, effectively decoupling the charge movement in the DILs from the simulation. As shown in fig. 5.6, this approximation can lead to a significant overestimation of the current density. Thus, simulation of full-stack OLEDs requires different approaches, which are developed and applied in the rest of this chapter: In section 6.3 the microscopic data of the OLED stack along with device and material properties computed with the kMC method are used to parametrize a DD model, avoiding the performance issues of the kMC model at the cost of detailed insight into the device operation at the mesoscopic scale. Section 6.4 presents a generalized method to decouple individual parts of the OLED stack in the kMC device simulation, which is used in section 6.5 to simulate the device completely with the kMC method.

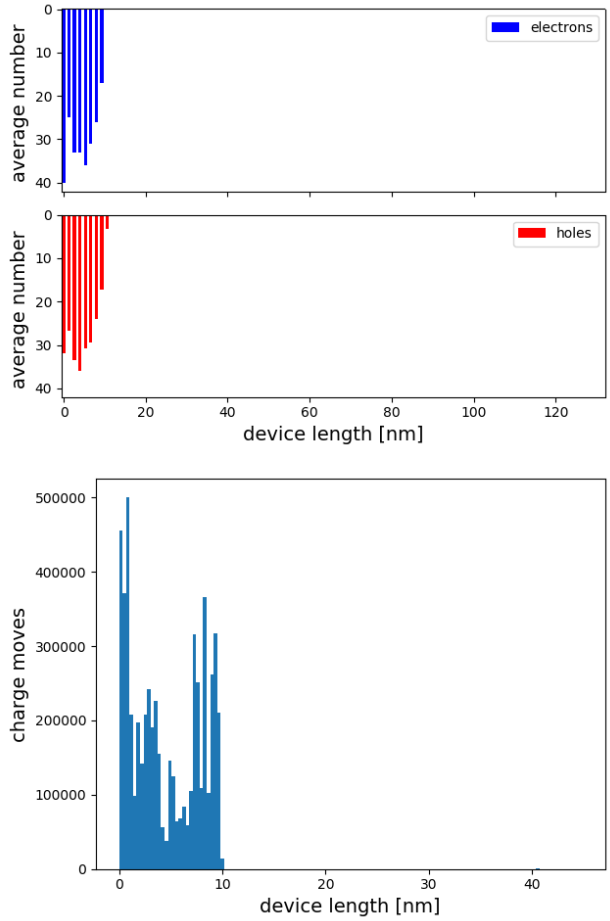

Figure 6.4: Charge and move distribution of the OLED stack after 2×10^7 kinetic Monte-Carlo steps with the doped injection layers treated explicitly. The charge distribution (top) shows that only a small fraction of holes escaped the doped injection layer. The move distribution (bottom) confirms that the simulation time was spent – almost exclusively – on charge movement in the doped injection layer.

6.3 BRIDGING ESTABLISHED CONTINUUM-SCALE WORKFLOWS

The study presented in this section was presented as [P1].

DD models are routinely employed in OLED stack development and optimization. The need for experimental parametrization, however, limits their usefulness and hinders their use in virtual design. To better utilize the potential of DD models, e.g. fast computation and widespread use in R&D, this study uses the microscopic parameters from section 6.1 to parametrize the DD model implemented in the TCAD software package from Silvaco Inc. Effectively bridging the gap between these microscopic- and continuum-scale models.

Using a Gaussian DOS

$$N(E) = \frac{N_0}{\sqrt{2\pi\sigma^2}} \exp\left[-\frac{\left(E - E_{\mathrm{EA/IP}}\right)^2}{2\sigma^2}\right], \tag{6.2}$$

the DD model discussed in section 2.2.3 requires the site densities N_0, transport energies $E_{\mathrm{EA/IP}}$, energy disorder $\sigma_{\mathrm{LUMO/HOMO}}$ and charge carrier mobility μ (eq. 2.5) of each material. Site densities N_0 are extracted from the atomistic morphologies deposited in section 6.1 and listed in table A.4 for reference. The charge carrier mobility is computed for each layer of the OLED stack with the protocol and parameters established in section 4.1.1. To better account for mixed layers, system size is increased to 60 nm × 60 nm × 60 nm with a charge carrier density of 4×10^{-4} per site to reduce the likelihood of trap filling. The other material parameters are taken from table 6.1. All *ab initio* parameters entering the DD model are plotted in fig. 6.5 along with the computational tool they are computed with.

With these parameters, the *J–V* characteristic of stack variant *B* is computed by Silvaco using the DD model implemented in their TCAD software package [173]. The electron–hole recombination rate R in the continuity equation (eq. 2.7) is taken to follow the Langevin form [174]

$$R = \frac{e}{\epsilon_r \epsilon_0}\left(\mu_n + \mu_p\right). \tag{6.3}$$

The *J–V* curve (fig. 6.6) computed from this parametrized DD model shows a good agreement with experiment. While the current density

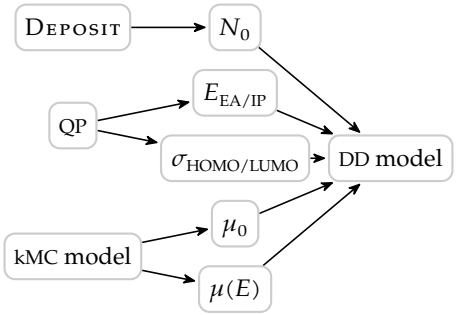

Figure 6.5: Microscopic input for the drift-diffusion (DD) device simulation. Site densities N_0 are computed based on the Deposit morphologies from section 6.1. IP and EA, as well as the energy disorder are taken from the values listed in table 6.1 computed using the QuantumPatch (QP) method. Computations of the field-dependent mobility $\mu(E)$ and zero-field mobility μ_0 are performed following the procedure presented in section 4.1.1 using the kinetic Monte-Carlo (kMC) model.

matches very well, especially in the medium to larger bias voltages, the field-dependence of the simulated current densities is slightly underestimated, leading to an overestimation of current density in the regime of low-voltages.

This work demonstrates the potential of the multiscale workflow to parametrize DD models, allowing these established models to work with a broader range of materials, e.g. ones designed completely *in-silico* or not (yet) characterized experimentally. Greatly speeding up development of novel materials and stack designs. As these DD simulations cannot provide insight into the device operation, this workflow, however, cannot replace kMC full-stack simulations, which are discussed in the following sections.

6.4 NOVEL METHOD TO DECOUPLE PARTS OF THE SYSTEM

To observe rare events, like electron–hole recombination, the simulation needs to span a large enough timescale. Since the time evolution per kMC step scales reciprocally with the total rate $\Delta t \propto \Gamma_{tot}^{-1}$ (eq. 2.15), additional events reduce the time evolved in a given number of simulation steps. As discussed in section 6.2, the addition of DILs to the OLED adds a large number of charge carriers with comparably large hopping rates

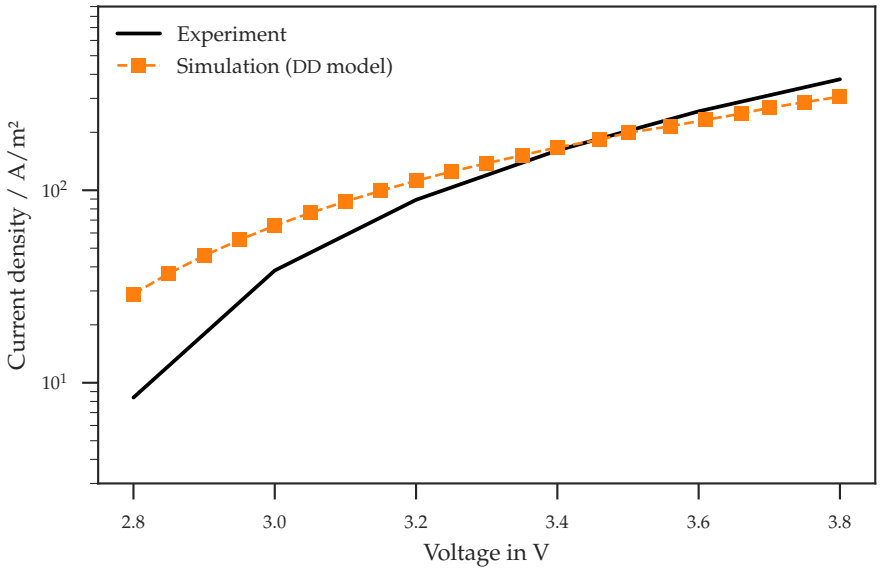

Figure 6.6: OLED stack variant *B* simulated with the drift-diffusion model implemented in the TCAD software package by Silvaco Inc. The simulations are performed by Silvaco based on the data computed in this chapter. The computed current density–voltage characteristic compares well with the experimental measurement. In the low-voltage regime, the drift-diffusion model underestimates the field-dependence, leading to an overestimation in current density.

around the ionized dopants, drastically reducing the achievable system timespans, rendering a complete kMC simulation of the entire stack unfeasible. Similar issues can arise when simulating regions with large barriers, e.g. at the electrode or at organic–organic interfaces.

While continuum models do not suffer from this issue, simply replacing the kMC model with continuum models, as demonstrated in the previous section, is not a general solution, as these models lack insight into the device operation. This section introduces a general method to solve the limitation largely diverging rates cause on the achievable time evolution of a system simulated with kMC models by decoupling regions with frequent events from the rest of the system, thus greatly speeding up calculations in the regions with rare events. To validate this method, this section simulates various test systems and compares the computed device characteristics to reference calculations.

To decouple individual parts of the system, the system is partitioned into slices with polaron transport across slice-interfaces modelled via

effective injection rates. By iteratively simulating the slices, the current densities in all slices are equilibrated, leading to charge carrier distributions similar to those in the real system. After equilibration, the simulation can be restricted to the region of interest, e.g. (part of) the HTL–EML–ETL layers in an OLED to improve sampling of excitonic processes.

The effective injection rate into a site f within slice B is computed by tracking occupation probabilities p_i of all connected sites i within slice A. According to the Pauli master equation the particle generation rate on site f

$$\Gamma_f = \sum_i p_i k_{if}(\Delta E_{if}) \tag{6.4}$$

is given by the probability p_i of a neighbouring site i being occupied, the probability of this charge carrier hopping to site f, given by the charge transfer rate k_{if}, and the site f being unoccupied, which is implicitly included in the energy difference in k_{if} via Coulomb repulsion. The Coulomb interaction of charge carriers in the vicinity of site i can have a large impact on ΔE_{if}. Individual configurations of charge carriers close to the slice interface C_n in slice A are therefore tracked explicitly. The effective injection rate into site f thus becomes

$$\Gamma_f = \sum_{n,i} P_n p_i^n k_{if}(\Delta E_{if}^n), \tag{6.5}$$

where P_n is the probability to find the particles in configuration C_n, p_i^n the probability of site i being occupied in C_n and ΔE_{if}^n the site energy differences with the contribution from differences in the Coulomb potential

$$\phi_{C_n} = \phi_B^{\text{dyn}} + \phi_{C_n}^{\text{dyn}} + \phi_A^{\text{avrg}} \tag{6.6}$$

split into the potential difference caused by the explicit charge carriers in slice B ϕ_B^{dyn} (eq. 3.8), the explicit charge carriers included in configuration C_n $\phi_{C_n}^{\text{dyn}}$ and the average charge densities ϕ_A^{avrg} for the charge carriers in slice A, which are further away from the interface.

Within each slice, in addition to regular processes, charge carriers can be injected into sites at the slice-boundary f with rates Γ_f given by eq. 6.5. Charge carriers hopping across slice-boundaries are removed from the system to restrict simulation on the active slice. Missing repulsive charge carriers in the neighbouring slice initially lead to an overestimation of

the charge density at the interfaces and thus an overestimation of the effective injection rates. Effective injection rates are therefore equilibrated iteratively until the current density in all slices converges.

One of the strengths of the explicit device model in the kMC simulation is the implicit inclusion of correlated particle moves missing in Master Equation (ME) and DD models. These are especially important in regions of large charge carrier concentrations, e.g. at organic–organic interfaces with large barriers or close to the DILs [107, 109]. To minimize the loss in detail due to loss of correlation across slice boundaries, these boundaries need to be located in regions with little average charge carrier concentrations.

The slicing algorithm is validated on four parametric test systems with increasing complexity as depicted in figs. 6.7, 6.10, 6.12 and 6.15. For each system, kMC simulations with slicing applied are performed and relevant device characteristics are compared to reference simulations without slicing.

Monolayer

The first test system is an organic monolayer in a 50 nm × 50 nm × 20 nm box acting as HTL with two electrodes attached. Hole injection from the anode is hindered by a small injection barrier of 0.2 eV, the workfunction of the cathode is chosen to facilitate hole extraction without a barrier. For simplicity, sites are placed on a cubic lattice with lattice spacing $a = 1\,\text{nm}$. For each site, the nearest 26 neighbours are considered as possible targets for direct hole transport. Site energies are drawn randomly according to a disorder of $\sigma = 90\,\text{meV}$, a typical value for a good hole transport material (see table 4.1). Hole densities in the slices, and thus effective injection rates, are equilibrated over four iterations with 100 000 steps in the first slice and 100 000 steps in the second slice. The reference system is simulated for 1 000 000 steps. The device layout and energy diagram are shown in fig. 6.7.

Figure 6.8 shows the *J*–*V* curve of the reference system and otherwise identical systems with a slicing boundary located at different distances d away from the anode. The *J*–*V* of the sliced devices generally agree well with the reference system. While current densities with slice boundaries

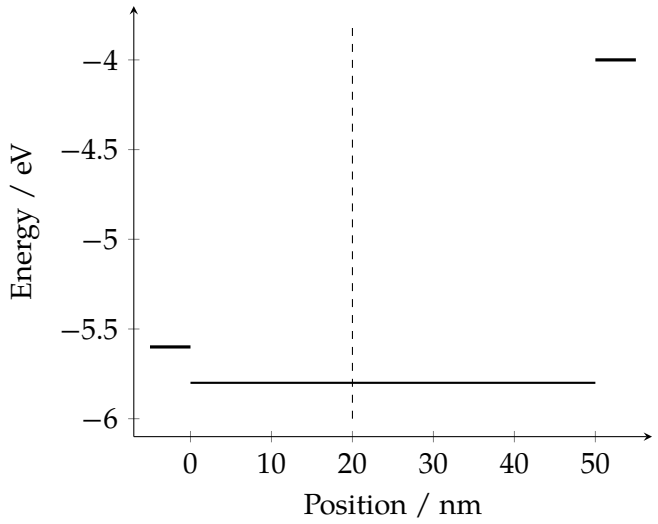

Figure 6.7: Energy levels of the parametric monolayer OSC. The slice boundary is indicated by the dashed line in the device diagram.

far away from the anode lead to very good agreement with the reference, current densities with slice boundaries close to the anode fluctuate around the reference. These deviations indicate inaccurate effective hole injection rates due to large hole densities close to the slice boundaries. As can be seen in fig. 6.9, the average hole density is quite large close to the anode and decreases up to 10 nm away from the anode. Few nm away from the anode, correlated charge moves play a role due to the large hole density, leading to inaccurate effective injection rates. Other quantities, such as the hole density shown in fig. 6.9, of the reference and $d = 20$ nm show a good match as well.

Bilayer

Starting from the monolayer, the system is split into two layers with the interface located at 25 nm and the IP of the second layer reduced by 0.2 eV to form a bilayer device with a small barrier between both layers, as can be seen in the energy diagram in fig. 6.10. To account for the large hole density close to the layer interface, the slice boundary is set ≥3 nm away from the layer interface.

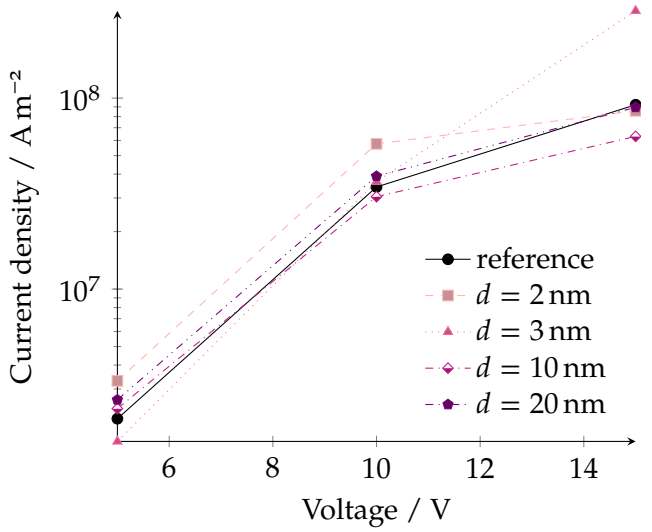

Figure 6.8: *J–V* curve of the monolayer test system shown in fig. 6.7 with (- - -) and without (—●—) slicing. Slice boundaries are situated a distance d of 2 nm, 3 nm, 10 nm and 20 nm away from the injecting electrode. While current densities of $d = 2\,\mathrm{nm}$ and $d = 3\,\mathrm{nm}$ deviate from the reference *J–V* due to the non-negligible hole density around the interface, as can be seen in fig. 6.9. Sliced simulations with the slice boundary further away from the area of large hole densities agree well with the reference.

As can be seen in fig. 6.11, the *J–V* of the sliced systems is in excellent agreement with that of the reference system. There appears to be little difference between the slice boundary located 3 nm and 5 nm away from the layer interface.

OLED

The sample OLED comprises a 20 nm HTL, 15 nm EML with 85 % host and 15 % emitter material, and 20 nm ETL sandwiched between two electrodes. Energy levels, depicted in fig. 6.12, are chosen to form a small injection barrier into HTL and ETL of 0.2 eV, a transport barrier out of the EML of 0.3 eV and no barrier for transport into the EML. Other parameters are chosen equal to the mono- and bilayer. Slice boundaries are set 5 nm from the HTL– and ETL–EML interfaces. The reference system is simulated for 5 000 000 steps, the sliced system is equilibrated in 4 iterations with 100 000 steps in the outer slices successively and

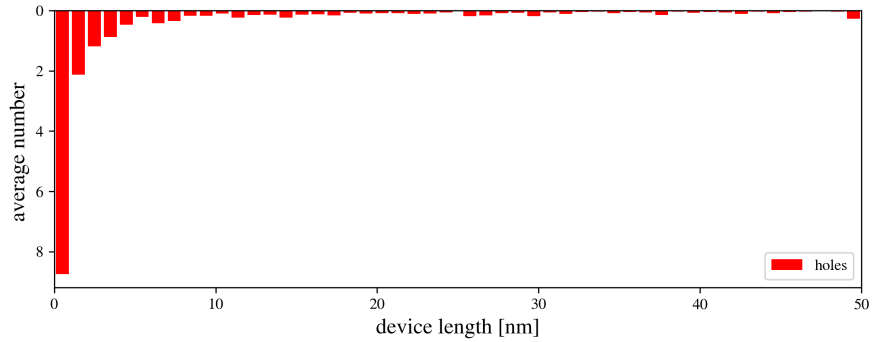

(a) Reference system

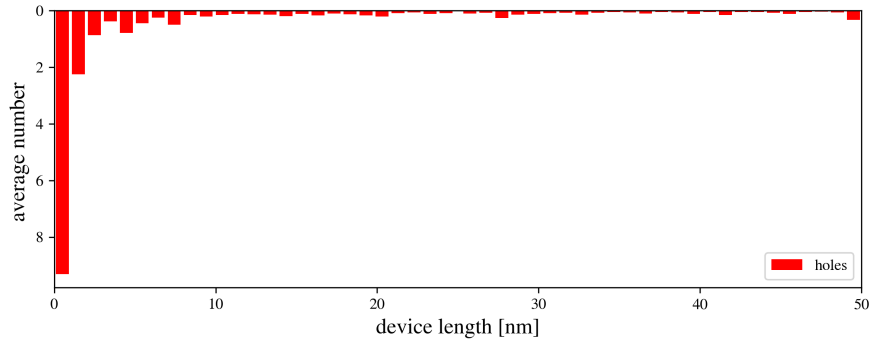

(b) With slicing applied

Figure 6.9: Average hole density of the reference system (top) and the sliced system with slice boundary 20 nm away from the anode (bottom). The average hole density in the sliced system agrees well with the reference density.

200 000 steps in the middle slice. Transport and device characteristics are evaluated in the last iteration of the middle slice.

In this device, again, the J–V computed from the sliced simulation and the reference system are in very good agreement (fig. 6.13). Charge carrier balance has a large influence on the efficiency of an OLED, rendering a close match in charge densities between sliced system and reference system crucial for the simulation with the slicing algorithm to properly predict key device characteristics. Figure 6.14 depicts hole and electron densities (bottom) and exciton quenching density (top) within the sliced- and reference system. As can be seen both charge densities and the resulting charge carrier balance agree well. In this system exciton–polaron interaction is the main contribution to quenching events in this

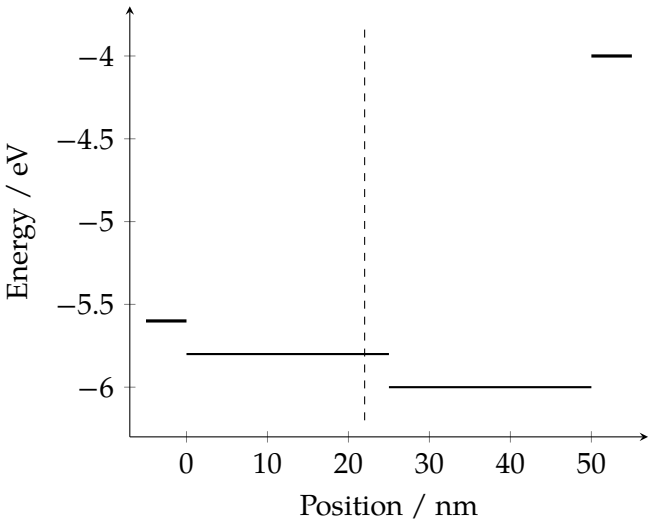

Figure 6.10: Energy levels of the parametric bilayer OSC. The slice boundary is indicated by the dashed line in the device diagram.

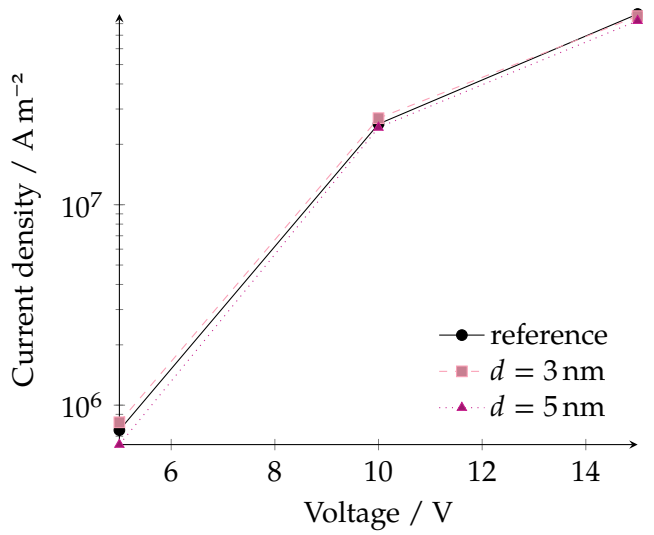

Figure 6.11: J–V of the bilayer test system shown in fig. 6.10 without (—●—) slicing and with slice boundaries located at $d = 3\,\mathrm{nm}$ (··■··) and $d = 5\,\mathrm{nm}$ (···▲···). Both simulations with slicing match the reference very well.

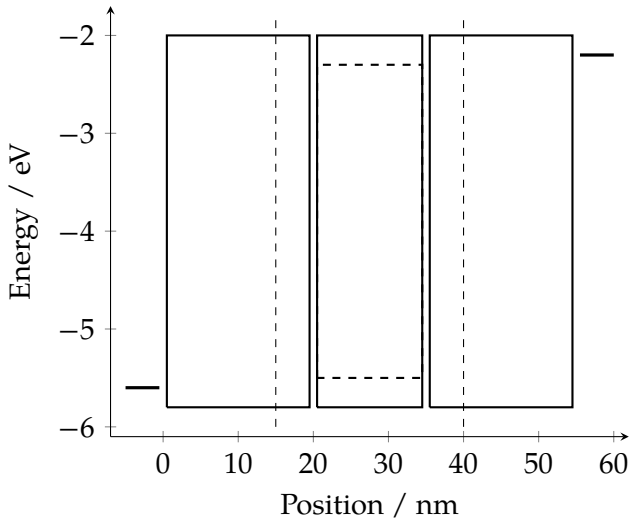

Figure 6.12: Energy levels of the parametric OLED. The slice boundaries are indicated by the vertical dashed lines in the device diagram.

system, making the quenching density highly sensitive to the charge carrier balance in the system. Minor deviations in the charge carrier balance therefore cause small deviations in the exciton quenching density visible in the quenching densities plotted in fig. 6.14.

Doped injection layer

As discussed in section 6.2, DILs, commonly employed to aid charge injection into OLED stacks, severely limit the time evolution in kMC simulations. While the other test systems are simple systems with little gain from slicing, separating the DILs from the rest of the system can result in a great speedup of the simulation. To validate the slicing algorithm in this context, charge transport through a 40 nm × 14 nm × 14 nm stack of 5 nm DIL and 35 nm HTL simulated with and without slicing is evaluated. The DIL is doped with 10 % of an ideal dopant. Host and dopant disorder is taken to be $\sigma_{\text{Host/Dopant}} = 150\,\text{meV}$, transport material disorder as $\sigma_{\text{HTL}} = 70\,\text{meV}$. The injection barrier into the host material is 1.0 eV. Other parameters are taken to be the same as in the previous systems. The reference stack is simulated for 10 000 000 steps. The sliced stack is equilibrated in 2 iterations. The doped slice is initially simulated for 4 000 000 steps to sample a sufficient number of particle configurations,

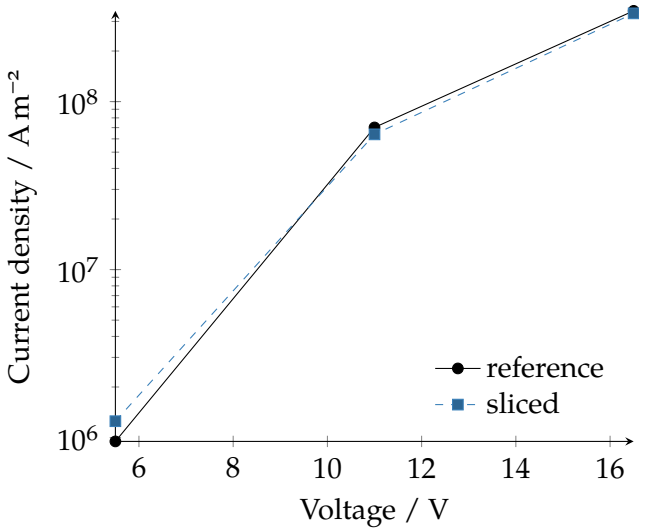

Figure 6.13: *J–V* of the OLED test system shown in fig. 6.12 with (- ■ -) and without (—●—) slicing match very well with a minor deviation towards smaller voltages at 5.5 V.

other slices are simulated for 1 000 000 steps each to equilibrate the charge density in the device, update the effective injection rates based on the equilibrated charge densities and collect charge transport characteristics.

The simulations with the slicing algorithm applied slightly overestimate the *J–V* of the reference system, as can be seen in fig. 6.16. The deviation is most prominent at small voltages as fewer holes leave the DIL in the same amount of kMC steps, leading to worse sampling of the effective injection rates at the slice boundary, and varies with the location of the slice boundary. Charge carrier concentration close to the electrode in the DIL is not as large as in the monolayer (fig. 6.7), allowing to chose a slice boundary close to the actual interface. In this case, $d = 5\,\mathrm{nm}$ leads to the closest match with the reference, apparently hitting a sweet-spot between more accurate effective injection rates due to lower charge concentrations away from the DIL–HTL interface and better sampling closer to the interface.

While the slice boundary located 5 nm away from the DIL–HTL interface shows a better agreement with the reference *J–V* at very low voltages, the difference between 3 nm and 5 nm is marginal, especially in the voltage regions relevant for OLED applications, while the potential speedup

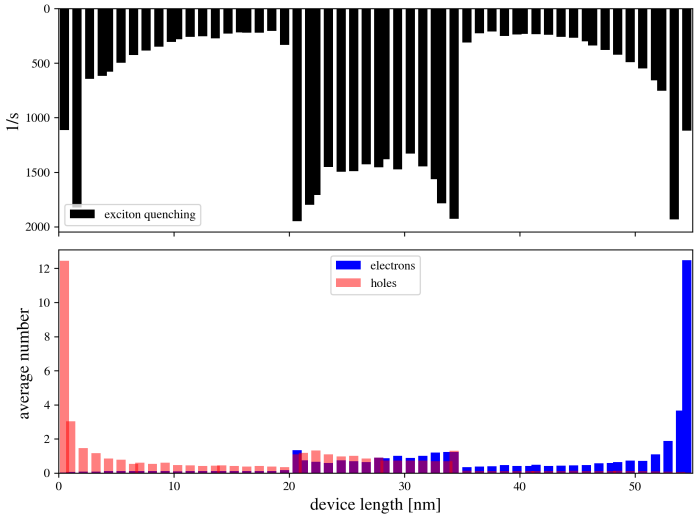

(a) Reference system

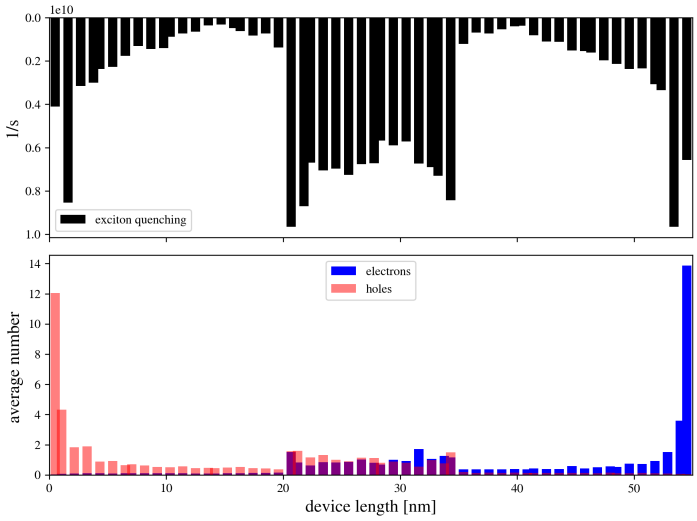

(b) With slicing applied

Figure 6.14: Average exciton quenching rate (black bars) and charge densities (blue and red bars) of the OLED test system with slicing (fig. 6.14b) agree well with the reference density (fig. 6.14a).

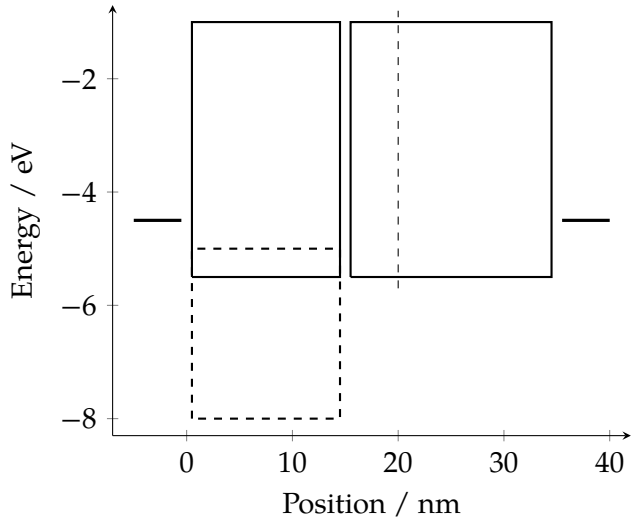

Figure 6.15: Energy levels of a monolayer OSC with a DIL added. The position of the slice boundary, indicated by the dashed line in the device diagram, has to strike a balance between a lower charge carrier density further away from the DIL–HTL interface, which leads to more accurate effective injection rates and better sampling due to more charge movement closer to the interface.

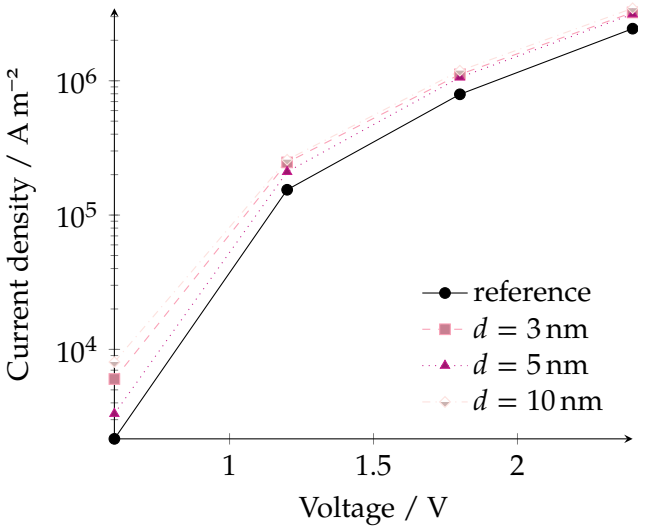

Figure 6.16: *J–V* of the doped injection layer test system shown in fig. 6.15 with (, ,) and without (—●—) slicing applied. While the different distances d away from the DIL–HTL interface perform equally well at medium to larger voltages, the slicing distances of 3 nm and 10 nm overestimate the current density at the low voltage.

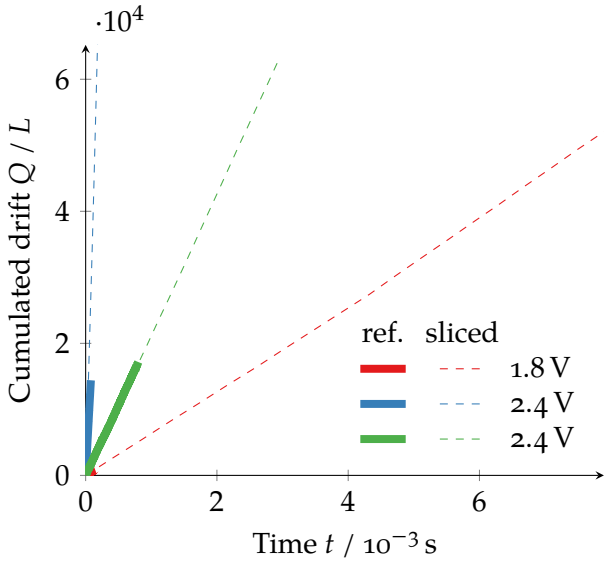

Figure 6.17: Cumulated drift Q in device lengths L of all charges in field direction over time for three sample simulations without (▬) and with slicing applied (- - -). Almost all charge carriers are located in the DIL and at the doped injection layer–hole-transport layer interface, resulting in most simulation time in the reference system being spent on charge movement in and close to the doped injection layer. Since the slicing method decouples charge movement in these regions of large charge carrier concentration and charge transport in the hole-transport layer, in the sliced systems far more charge movement in field direction is simulated in ⅒ the simulation steps compared to the reference calculations. The ratio of charge carrier drift and diffusive charge movement within the doped injection layer decreases with lower voltages, leading to larger potential speedups, as can be seen in the ratio of sliced and reference trajectories of the samples at 1.8 V and 2.4 V.

greatly increases with a slice boundary closer to the actual interface. To visualise the speedup, fig. 6.17 depicts the cumulated drift of all charge carriers in field direction Q in device-lengths L over the system time t for three individual simulations in the sliced ($d = 3\,\mathrm{nm}$) and reference system. Even in only ⅒ the kMC steps, the charge carriers in the sliced system propagate far greater lengths than in the reference system.

While charge injection into the DIL and charge transport across the DIL–HTL/–ETL interface are governed by the charge carrier balance in the DIL, the properties of interest in such systems are the J–V characteristic and resulting charge carrier balance in the bulk of the device. The slicing

method allows computation of these characteristics even for systems with large DIL or complete OLEDs, facilitating virtual screening of DILs and device composition to optimize e.g. charge carrier balance within the emissive region.

6.5 FULL-STACK KMC SIMULATION

The study presented in this section and section 6.1 is being prepared for publication [A1].

KMC simulation of charge and exciton dynamics in complete OLED stacks to date is limited to models parametrized with experimental data [36, 40]. Using the microscopic parameters calculated in section 6.1 as input for the kMC model along with the method to solve performance issues of full-stack simulations, presented in section 6.4, finally enables the *de novo* simulation of the complete OLED stack on the kMC scale.

Employing these methods, this section presents the first simulation of a full OLED stack including all relevant microscopic processes based on molecule-specific rates derived from first principles. Specifically, these simulations explicitly include DILs, a necessity in achieving accurate current densities in comparison with experimental data. These simulations demonstrate that the multiscale workflow – by translating molecular properties to the device scale – bridges the gap between fundamental chemistry and device design, and is able to predict device characteristics, specifically quantum efficiency, with high accuracy.

First, the deposited thin-films of each layer are stochastically expanded to a base area of 20 nm × 20 nm and the respective layer thickness to obtain an amorphous structure of the OLED stack. For this expanded amorphous structure, site energies are drawn following the Gaussian distribution of $\Delta E_{ij}^{\mathrm{HOMO/LUMO}}$ around the IP and EA of the specific material. The resulting schematic energy diagram is depicted in fig. 6.18 (left panel). Reorganization energies are drawn following the Gaussian distribution of λ_i. Electronic coupling elements J_{ij} and Coulomb binding energy V_{C} for each pair of sites with distance r_{ij} are drawn from the microscopic distribution $J(r)$ and $V_{\mathrm{C}}(r)$, respectively, within the small interval dr around r_{ij}. Connectivity of a given pair of sites i and j with distance r_{ij} is determined by the probability of a pair of molecules

with a centre of mass distance r having a nearest atom distance of less than 7 Å. Dipole transition moments $\vec{d}$ are mapped onto the expanded structure by randomly rotating the set of vacuum moments.

Based on these thin-films, charge transport and exciton dynamics are simulated in these expanded devices using the kMC model. Charge transport rates are computed based on Marcus theory (eq. 2.4). The dynamic electrostatic potential included in ΔE_{if} is reevaluated after each charge movement by calculating the electrostatic Ewald Sum [147] including all charges in the system and an infinite series of image charges due to the metallic boundary conditions at both electrodes. Charge injection and extraction is modelled with the MA rate (eq. 3.11). Förster and Dexter rates are calculated based on Marcus theory (eq. 2.4) with the Dexter electronic coupling computed as given by eq. 3.4 and the Förster coupling as given by eq. 2.12. The microscopic inputs and the respective rates they influence are sketched in fig. 6.19.

Improved electron injection due to the addition of a thin layer of LiQ is modelled as Li doping the ETL [172]. A small fraction of LiQ (2 %; varying the fraction from 0.5 % to 4 % did not have an impact on the computed current densities) is assumed to act as a dopant for the ETL material close to the ETL–LiQ interface.

As discussed in section 6.2, kMC models of full OLED stacks struggle with the large number of charge carriers in the DILs leading to small timesteps, which in turn require an excessive number of simulation steps to sample a sufficient number of, comparatively rare, exciton processes in the EML. To solve this problem, the method discussed in section 6.4 is used to decouple the HIL and EIL from the rest of the device. First, the full stack, including both HIL and EIL, is simulated for approx. 10 µs to equilibrate charge densities in both HIL and EIL simultaneously. After initial equilibration, charge densities are equilibrated iteratively in each part of the device – HIL, EIL and HTL–EML–ETL – for two cycles. Finally, the inner part of the device is simulated for an additional 4×10^7 kMC steps to sample a sufficient number of exciton processes.

During equilibration, dopant sites are activated, with the resulting charge movement shifting the Fermi level of HIL and EIL towards the work function of the attached electrodes. Figure 6.18 (right panel) depicts the energy levels in the device in the equilibrated state. As can be seen, p-type doping in the HIL is sufficient for complete Fermi level

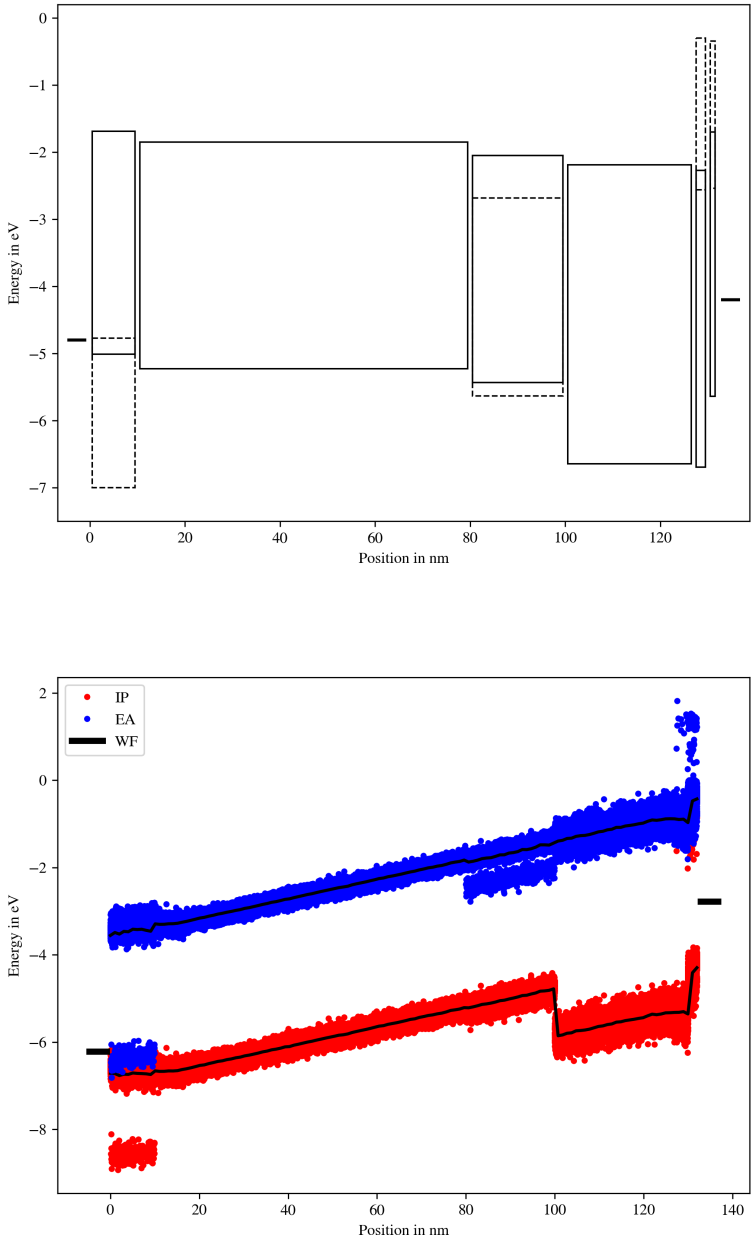

Figure 6.18: Schematic energy diagram of the device variant *B* based on IP and EA levels computed with the QuantumPatch method (top panel, values listed in table 6.1) and polaron energy levels after equilibration in the kMC model (bottom panel) at a bias voltage of 3.4 V.

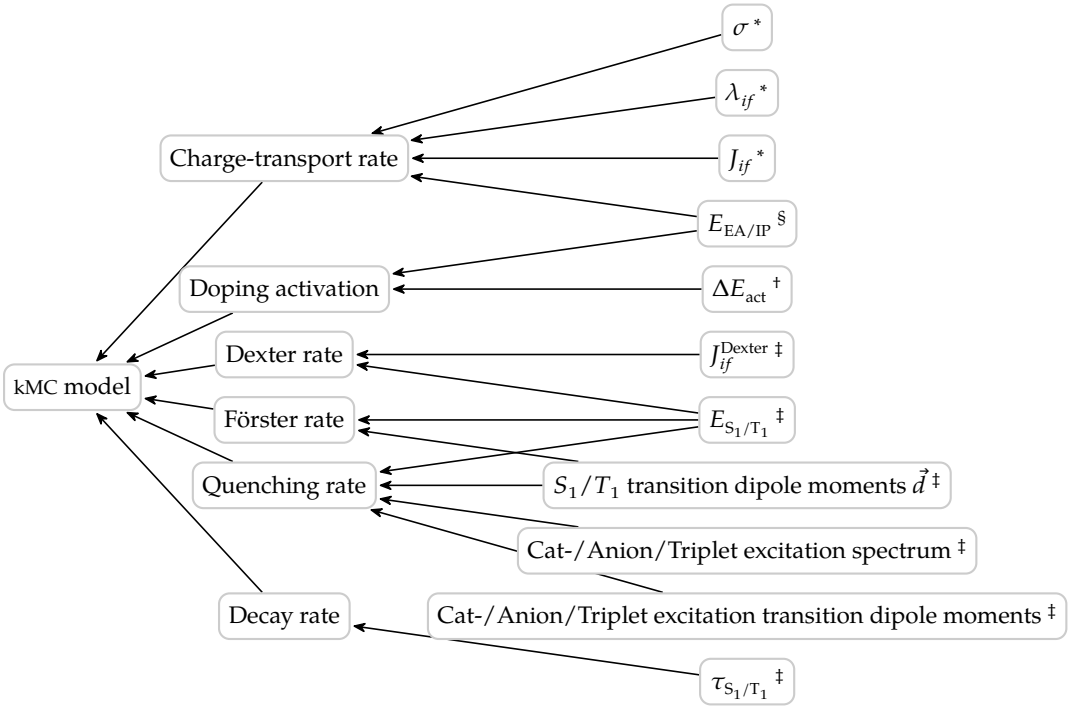

Figure 6.19: Microscopic input for the kMC device simulation. Quantities computed as presented by *Friederich et al. [85], †Symalla et al. [A8], ‡Symalla et al. [39] and §Armleder et al. [134].

alignment between HIL and anode, while the modelled *in situ* doping of the EIL [172] still leaves an injection barrier between EIL and cathode.

To account for stochastics in morphology expansion and site energy distribution, 60 different configurations are sampled per applied field. Convergence is reached when the current density is constant over two thirds of the simulation.

Current densities are computed from the cumulative drift of charge carriers through the HTL, EML and ETL. The simulated J–V characteristics are depicted in fig. 6.20 along with the J–V measured by IMEC for comparison. As can be seen, simulated and measured J–Vs show a good agreement. The measured current densities lie within the standard deviation of the simulations for all voltages in both devices. However, the simulations tend to underestimate the field-dependency for larger voltages.

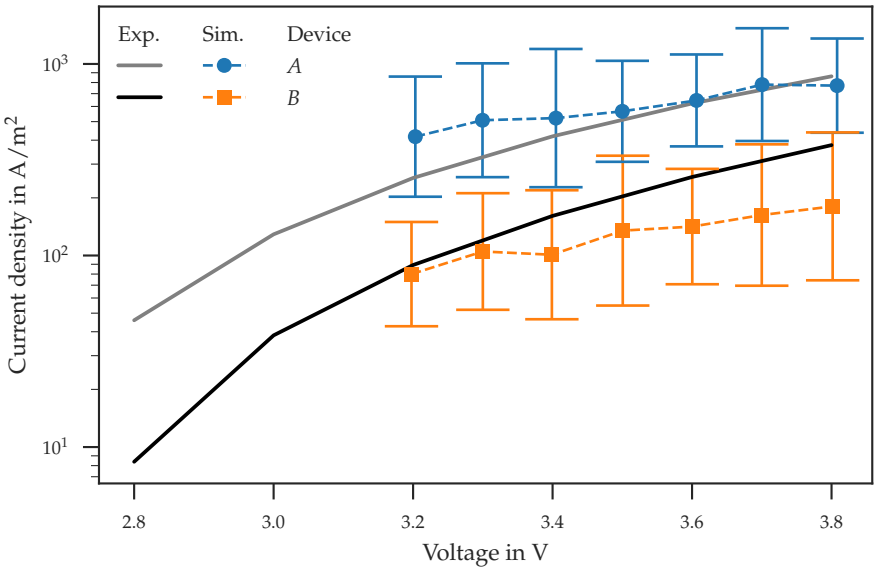

Figure 6.20: The simulated *J–V* curve of the red OLED stack variants *A* and *B* along with the experimental data provided by IMEC. Both *J–V*s compare well with experiment. While the simulations of both devices appear to underestimate the field-dependence, the computed characteristics are consistent with one another, likely caused by a systematic error in both devices.

The IQE is computed as discussed in section 4.3 from the total number of excitons and photons in all 60 samples.

As only external quantum efficiencys (EQEs) are measured, approximate EQEs are computed from the simulated IQEs and the outcoupling efficiency (OCE) η_{out} as

$$\eta_{\text{EQE}} = \eta_{\text{IQE}} \eta_{\text{out}} \,. \tag{6.7}$$

As the computation of η_{out} requires optoelectronic models, which are out of scope of our multiscale workflow, a common OCE for OLEDs of $\eta_{\text{out}} = 20\,\%$ is assumed [175]. Varying ETL thickness leads to differences in OCE [176]. Using the relative radiance determined by IMEC (fig. A.7), the reduced ETL thickness of device variant *A* leads to a drop of

$$\frac{\eta_{\text{out}}^{A}}{\eta_{\text{out}}^{B}} \approx 0.42 \tag{6.8}$$

compared to device variant *B*. The resulting EQEs are plotted in fig. 6.21 along with the measured EQEs. As can be seen, the simulation is able

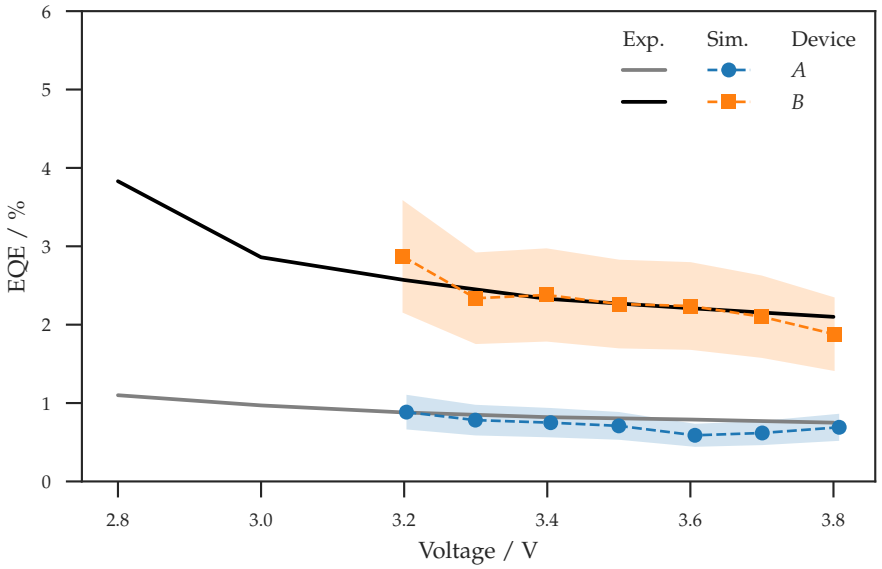

Figure 6.21: Simulated external quantum efficiency (EQE) of device variants *A* and *B* computed from the internal quantum efficiency with an assumed outcoupling efficiency of 20 % [175] (shaded region 15 % to 25 %) compared to the measured external quantum efficiency. The external quantum efficiency of device variant *A* accounts for the reduction in outcoupling efficiency due to the reduced thickness of the electron-transport layer (fig. A.7), which would otherwise lead to an overestimation of external quantum efficiency in this device.

to provide accurate EQEs of both devices and resolve the differences in both stacks.

Analysing the exciton decay processes can help optimize the OLED stack and better interpret the EQE. As can be seen in fig. 6.22, quenching via Förster-transfer of a triplet onto a polaron (labelled TPQ) is the leading loss process in this device. Following TPQ with a large gap are quenching via charge transfer of a polaron onto a triplet (labelled PTQ) and radiative decay. Non-radiative decay is rare and its influence on the device performance can be neglected. Surprisingly, TTA does not play a role as a loss process. Despite a large difference in TTA- and TPQ-rates, $k^{\mathrm{TTA}}/k^{\mathrm{TPQ}} \approx 10$, the large number of charge carriers present in the EML leads to TPQ being greatly favoured over triplet–triplet loss processes. Two of the main contributions that reduce the IQE of device variant *A* compared to variant *B* are the larger quantity of charge carriers within the EML and their less balanced distribution. Thus, based on the kMC

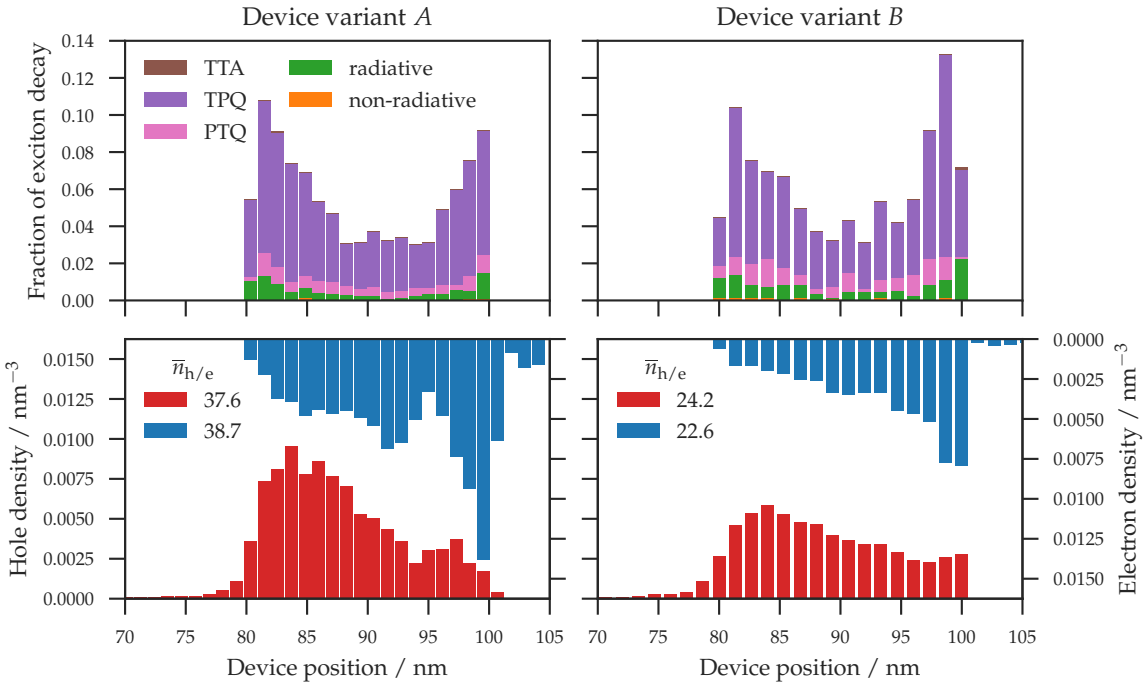

Figure 6.22: Exciton decay by process and position in the device (top panel) along with charge carrier densities in thin slices of the device and average charge density within the emissive layer $\bar{n}_{h/e}$ (bottom panel) at 3.4 V. Triplet–polaron quenching (TPQ) is the leading quenching process, followed by polaron–triplet quenching (PTQ). Triplet–triplet annihilation (TTA) and non-radiative decay are rare. As is expected, regions with large numbers of TPQ and PTQ processes coincide with regions of high charge carrier density. The larger internal quantum efficiency of device variant *B* stems from the lower charge carrier density in this device, leading to a reduced fraction of excitons quenching via TPQ and PTQ.

model, reduction of charge carrier densities in the EML and improved charge balance, along with a reduction of the rates associated with polaron quenching hold the greatest potential for optimization of this device.

6.6 DISCUSSION

This chapter presented a multiscale workflow to compute material properties and simulate charge transport and excitonic dynamics in a

complete OLED stack *de novo*. Microscopic properties were computed in section 6.1 for all materials employed in the red OLED stack. Section 6.2 discussed the performance issues of the kMC model when adding DILs to a large device. A problem, which can be solved with a novel method to decouple parts of the system presented in section 6.4. Using this method, two variants of the full OLED stack were simulated in section 6.5 with the kMC model and compared to experiment. Computed device characteristics of both device variants were in good agreement with experimental data provided by IMEC.

This multiscale model to predict OLED device characteristics can aid experimental R&D in designing efficient and durable OLEDs in two ways. First, as demonstrated in section 6.3, the workflow can be used to parametrize DD models for fast screening of device configurations. Second, as demonstrated in section 6.5, the entire workflow enables a thorough investigation into the detailed device operation, which helps identify bottlenecks in specific device configurations [177] and potential improvements [A10]. Both these parameter-free approaches are able to compute current density–voltage characteristics to good agreement with measurements performed by IMEC. The mesoscopic kMC model of the OLED enables an insight into the device operation, e.g. efficiency characteristics, which closely match efficiency measurements performed by IMEC. The possibility to observe the device operation on the kMC scale allows determination of device and operational properties, which are elusive in experiment, e.g. charge carrier distribution and exciton decay profiles. Thus showing great potential to becoming a valuable asset in OSC research, as well as material and device development.

The kMC simulations in section 6.5 highlight several paths for improving the kMC device model, which would result in increased computational efficiency of the simulations with the goal of both reducing computational cost and allowing for faster sampling of different configurations, enhanced prediction quality and more device characteristics for device designers to base their work on.

When using the slicing method to decouple parts of the system, individual configurations show a much greater variance than in the regular simulations, e.g. computations in the other chapters. In the present case, this effect necessitated simulating a much larger number of samples than usual, greatly increasing the computational cost. The overall efficiency of the simulations could therefore be increased by either im-

proving the slicing method, especially tuning the sampling of configurations close to the slicing boundaries, or going a step further and, using simulations with the slicing method as reference simulations, improving approximations employed in literature to more accurately model the effects of DILs.

Due to site energy differences entering the exponent in the Marcus rate (eq. 2.4), the current density is very sensitive to energy barriers. Even small errors in the computed IP and EA can have a large impact on the computed device characteristics and are prime suspects for the cause of the kMC model underestimating the field-dependence of the *J*–*V*s in section 6.5. Refining both the *Deposit* method to generate amorphous morphology with a closer resemblance of the real morphology and the QP method to allow more accurate computations of the molecular energy levels are therefore likely to further improve the quality of the device characteristics predicted by the kMC device model.

As can be seen in section 6.5, the outcoupling efficiency (OCE) can not be ignored when optimizing the OLED device geometry, since comparatively small modifications to the device geometry can easily lead to an increase or decrease of the external quantum efficiency (EQE) by a factor of 2, in this specific case an increase of ETL thickness by 20 nm between device variants *A* and *B* caused the OCE to increase by factor of 2.5. In order to design an efficient OLED, the device designer thus needs to factor in the OCE when optimizing the device geometry. As a future step, an OCE model could either be integrating directly into the multiscale workflow or the quantity could be computed using the models integrated into the Silvaco TCAD suite via the interface integrated into the multiscale model in section 6.3.

7

SUMMARY AND OUTLOOK

SUMMARY

Design of improved OLED devices and development of novel materials are mainly driven by experiment, aided by fast computational screening methods on the molecular level. Recent progress in multiscale workflows to compute device characteristics with parametric models shows great potential to support experimental research and development of performant OLED devices. However, these models, to date, are not generally applicable, as they e.g. require experimental parametrization, cannot model microscopic processes that influence the operation of OLEDs or neglect relevant parts of the device. In this work, I extended a multiscale workflow to bridge the gap between fundamental chemistry and device design, specifically to compute organic semiconductor material properties and device performance for a broad range of devices, including a full OLED stack, without requiring input from experiment.

In the past decades, much effort has been put into the development of novel materials with improved transport properties. Despite these efforts, charge carrier mobility in amorphous organic semiconductors is still several orders of magnitude below that in inorganic semiconductors, limiting the performance of organic semiconductor devices, like OLEDs and organic solar cells. Computational methods have become an indispensable tool in speeding up characterization of new material candidates, however, these methods require experimental input to achieve good accuracy. Improvements to these methods, allowing for accurate predictions of charge carrier mobility *de novo*, therefore hold great potential to speed up design and discovery of novel material candidates, help explore the vast molecular space and boost the development of balanced devices. In section 4.1.1, I integrated the kMC device model into a multiscale workflow to compute charge carrier mobility based on microscopic charge transport. Using this workflow, I was able to

improve the prediction quality of prior work, enabling computation of charge carrier mobilities for a broad range of different materials to good agreement with experimental data *de novo*.

In order to design efficient OLEDs, it is essential to balance the charge density within the device. However, compared to hole-transport layer materials, electron-transport layer materials suffer from large polarity of the molecules, inducing a large energy disorder. This results in low electron mobilities, further increasing the difficulty of balancing the charge density in the device. Computational methods can help reduce this detriment by providing detailed insight into the device operation, which is available in experiment only with specialized device setups and even then challenging to measure. Building on the insights gained using the multiscale model in the previous computations, I developed a scheme to improve the electron mobility of TPBi, a common electron-transport layer material, by disorder passivation in section 4.1.2: the electron mobility can be tuned by adding transport inert guest molecules with low polarity, allowing for targeted design of OLED layers. Computations are used to identify the sweet spot in the parameter space and show an enhancement in electron mobility of one order of magnitude for the optimal concentration of a sample guest molecule NPB doped into TPBi. As demonstrated, this method offers a very simple tool for device designers to improve charge carrier balance within an OLED, thereby improving device performance and efficiency. Specifically targeted material combinations are expected to have a far stronger effect, allowing for even greater control in designing balanced OLEDs.

Even with good charge transport materials, OLED devices cannot operate efficiently, if charges are injected into the device at an insufficient rate, which cannot sustain charge transport. One option to counteract insufficient charge injection lies in designing devices that feature ohmic injection. In section 4.2, I employed the multiscale workflow to compute device characteristics of large single-carrier devices featuring ohmic injection. Modelling these devices comprises challenges on various levels of the multiscale model: At the device scale, ohmic injection leads to a large number of charge carriers located in the vicinity of the electrode, drastically increasing the complexity in modelling the quickly evolving electrostatic potential in every kMC step. The high thickness of the devices requires a comparatively large number of kMC steps to equilibrate the system, leading to a further increase of computation time. At the microscopic scale, ohmic injection requires accurate com-

putations of ionization potential and electron affinity, as computed current density–voltage curves are very sensitive to the injection barriers. Despite these challenges, using the multiscale model, I was able to compute device characteristics of these single-carrier devices to very good agreement with experiment and provide insight into physical quantities, such as the detailed charge carrier distribution within the devices, which are accessible in experiment only with great difficulty and effort.

To simulate the operation of an OLED, the kMC device model needs to incorporate bipolar charge transport, exciton formation via charge carrier recombination, exciton dynamics and radiative decay of excitons. While OLED devices are designed to restrict excitonic processes to a – or multiple – emissive regions for improved device efficiency, multiple additional layers add a great deal of complexity to the device model. In its simplest form, as demonstrated in section 4.3, all of the required processes can be observed in a simplistic device with the addition of a second layer consisting of a slightly modified molecule, in this case two substitutions of nitrogen for a carbon atom. Simulation of this simplistic device, using the multiscale workflow, provided insight into the charge transport and the resulting charge carrier distribution within this device, as well as the distribution of created and quenched excitons and emitted photons. These properties remain challenging to measure and can presently not be obtained in this level of detail in experiment. The simulations provide clear strategies for possible device optimizations, demonstrating the potential of this multiscale workflow in rational device design.

The second part of this work, namely chapter 5, focuses on a relatively small, yet crucial part of efficient OLED devices: doped injection layers. As effective method to ease injection from the metal electrodes into organic layers, they have become a *de facto* standard in the design of performant OLED devices. Extension of the multiscale workflow to include these doped injection layers allowed investigating their influence on device characteristics of model devices in section 5.1 and benchmark approximations employed in literature multiscale simulations. These computations, on one hand, can aid in tuning the doped injection layers, e.g. layer thickness and doping ratio, to achieve optimal charge injection into the device and charge carrier balance within the device. On the other hand, the computations show a significant influence of the doped injection layers on the device characteristics, which are not properly

rendered by common approximations, which either completely ignore doped injection layers or treat them as effective electrodes. Specifically, even the latter lead to an overestimation in current density by several orders of magnitude in the doping regime relevant for OLED stacks.

Building on these model studies, the doping model was validated in section 5.2 for a realistic doped injection layer using microscopic doping parameters for a prototypical pair of host- and dopant-molecules, α-NPD and F4TCNQ, derived with the multiscale workflow. Based on this input, I computed current density–voltage characteristics of a device reported in literature, and demonstrated that this workflow allows for *in-silico* screening of host–dopant pairs and selection of the ideal dopant for a given combination of hole-transport layer, emissive layer and electron-transport layer, both time-consuming and resource-intensive endeavours when undertaken solely based on experiment.

As the final part of this thesis, in chapter 6, I combined the work presented thus far to simulate a full OLED stack *de novo* using the multiscale model. As discussed in section 6.2, a simulation of the entire stack using the kMC model is not feasible when incorporating the doped injection layers into the device model as is. To overcome this limitation, I investigated two approaches: First, in section 6.3, as a bridge to established device models, I used the microscopic multiscale workflow to parametrize a drift-diffusion model, thus enabling fully virtual design with established continuum-scale models. Second, in section 6.4, I applied and validated a method to decouple individual parts of the OLED stack. Device characteristics computed in section 6.5 using this method to overcome performance issues when incorporating doped injection layers into the OLED stack show good agreement with experiment. As demonstrated, these simulations allow for detailed comparison of different devices and provide valuable insight into the charge carrier distribution within the devices and associated excitonic processes.

With this work, I closed a gap in current multiscale models to simulate the operation of OLED devices on the kMC level *de novo*. Specifically the combination of three key ingredients, namely a) computation of reliable microscopic parameters as input for the device simulation, b) an accurate model for charge transport within doped injection layers and their influence on charge transport through the device and c) a method to efficiently treat doped injection layers while retaining their unique influence on the device performance, enables the simulation

of OLED devices based on microscopic processes modelled with individual, material-specific rates. Using these improved methods, I was able to simulate a modern full-stack OLED *de novo* at the kMC level to experimental accuracy – to my knowledge – for the first time. This work offers a reliable approach to translate molecular design to the device level and to systematically investigate microscopic performance bottlenecks and eliminate them, thus providing a viable tool for rational design of novel OLED materials and devices.

OUTLOOK

To date, OLEDs still suffer from various shortcomings, which limit efficiency and lifetime of devices and thus hinder their more widespread adoption. Among the most pressing issues are phosphorescent blue emitter materials, which are far inferior to red and green emitters with respect to both durability and efficiency. Discovery of blue emitter materials which are both long-lived and efficient requires benchmarks of completely novel materials, followed by design and optimization of novel OLED stacks to utilize their full potential.

As demonstrated in this work, the presented multiscale workflow can aid research and development overcome these remaining impediments of OLED devices via design of improved materials and OLED designs in several ways: First, due to the good agreement with experiment on the computed material properties, such as charge carrier mobility, the fully virtual screening capabilities of this workflow can be used to verify – or falsify – molecule properties predicted by fast screening methods prior to experimental synthetization and characterization, thereby helping to focus experimental effort and resources on truly promising candidate molecules. Secondly, by bridging the gap between these microscopic material parameters and continuum-scale device models, e.g. drift-diffusion models, routinely employed in device design, the multiscale workflow opens the prospect of a higher level of automation in the design of novel OLED devices. Finally, the kMC device model allows inspecting the microscopic details of the device operation, which are not available at this level of detail in experiment or continuum-scale device models. This insight can help track the underlying cause of loss processes and degradation mechanisms and, ultimately, aid in building

a fundamental understanding on the structure–function-relationship that link molecular properties and device performance.

Specifically, the insight into the operation of the OLED device gained from simulation can be used to improve device design in order to reduce loss processes, enabling *in-silico* optimization. While this workflow can be used to predict how changes to specific parameters, e.g. integration of a specific material or variation of layer thicknesses, would influence device operation and the resulting device characteristics, it remains a bottom-up approach, requiring intuition and trial and error to create devices with improved performance. As such, the presented multiscale model is a prime candidate for pairing with artificial intelligence (AI) methods, i.e. use the physical multiscale model to train AI models. In future work, this approach could invert the direction of prediction and provide yet uninvestigated, or undiscovered, molecular structures with specifically targeted properties based on the requested parameters.

The accuracy of the kMC device model depends strongly on the quality of the amorphous morphology and computed microscopic material parameters. Improvements to the DEPOSIT and QUANTUMPATCH methods could therefore further boost the quality of the *de novo* OLED device simulations.

Despite the focus of this work, the presented multiscale model is not limited to the application in OLED research. It can easily be generalised to compute device properties of other actively researched organic semiconductor applications, like organic solar cells. While specifics of organic solar cell operation and fabrication necessitate alterations to some parts of the multiscale model – e.g. replacing the DEPOSIT vapour deposition protocol with a method that can model domain formation during liquid processing of organic solar cells – especially the kMC device model is fully equipped to simulate device operation of organic solar cells and, to a lesser extent, organic field-effect transistors.

A

APPENDIX

A.1 ACRONYMS

3-21G Pople split valence basis-set

AI Artificial intelligence

B2-PLYP Hybrid exchange-correlation functional with pertubative second-order correction

B3LYP Hybrid exchange-correlation functional

BP86 Combination of Becke's exchange functional and Perdew's correlation functional

CAM-B3LYP Hybrid exchange-correlation functional using the Coulomb-attenuating method

COM Center of mass

CT Charge transfer

DD Drift-diffusion

def2-SVP Gaussian basis set of split valence quality

DFT Density-functional theory

DIL Doped injection layer

DOS Density of states

EA Electron affinity

ECP Effective core potentials

EIL Electron injection layer

EML Emissive layer

EQE External quantum efficiency

ESP Electrostatic potential

ETL Electron-transport layer

EXTMOS EXTended Model of Organic Semiconductors

FRET Förster resonance energy transfer

HIL Hole injection layer

HOMO Highest occupied molecular orbital

HTL Hole-transport layer

IMEC Interuniversity Microelectronics Centre

IP Ionization potential

IQE Internal quantum efficiency

ISC Inter system crossing

ITO Indium-tin oxide

J–V Current density–voltage

kMC Kinetic Monte-Carlo

KS Kohn–Sham

LEIPS Low-energy inverse photoemission spectroscopy

LF LightForge

LJ Lennard-Jones

LUMO Lowest unoccupied molecular orbital

MA Miller–Abrahams

MC Monte-Carlo

ME Master Equation

MSMEE Multi-Skalen-Modellierung von Materialien und Bauelementen für die Energieumwandlung

OCE Outcoupling efficiency

OE Organic electronics

OFET Organic field-effect transistor

OLED Organic light-emitting diode

OPV Organic solar cell

OSC Organic semiconductor

PBC Periodic boundary conditions

PTQ Polaron–triplet quenching

QP QuantumPatch

R&D Research and development

RDF Radial distribution function

RFID Radio-frequency identification

SA Simulated annealing

SCLC Space-charge limited current

SI Supporting information

TADF Thermally activated delayed fluorescence

TCAD Technology computer-aided design

TDDFT Time-dependent density-functional theory

ToF	Time-of-flight
TPQ	Triplet–polaron quenching
TTA	Triplet–triplet annihilation
TTF	Triplet–triplet fusion
UPS	Ultraviolet photoelectron spectroscopy

A.2 MOLECULAR STRUCTURES

α-NPD	*N*,*N*′-di(1-naphthyl)-*N*,*N*′-diphenylbenzidine
ADP	9,10-diphenylanthracene
ADP(N)	ADP with two carbon atoms substituted for nitrogen
Alq3	Tris(8-hydroxyquinoline)aluminum
BCP	2,9-Dimethyl-4,7-diphenyl-1,10-phenanthroline
BPBD	2-(4-biphenylyl)-5-(4-tert-butylphenyl)-1,3,4-oxadiazole
DEPB	1,1-bis-(4,4′-diethylaminophenyl)-4,4-diphenyl-1,3-butadiene
F4TCNQ	2,3,5,6-Tetrafluoro-7,7,8,8-tetracyanoquinodimethane
F6TCNNQ	Hexafluorotetracyanonaphthoquinodimethane
$Ir(MDQ)_2(acac)$	Bis(2-methyldibenzo[f,h]quinoxaline)(acetylacetonate)iridium(III)
LiQ	(8-Hydroxyquinolinato)lithium
m-BPD	*N*,*N*′-di(biphenyl-3-yl)-*N*,*N*′-diphenyl-[1,1′-biphenyl]-4,4′-diamine
NNP	*N*,*N*′-bis(1-naphthalenyl)-*N*,*N*′-diphenyl-4,4′-phenyldiamine
NPB	*N*,*N*′-di(1-naphthyl)-*N*,*N*′-diphenylbenzidine

p-BPD	*N*,*N*′-di(biphenyl-4-yl)-*N*,*N*′-diphenyl-[1,1′-biphenyl]-4,4′-diamine
o-BPD	*N*,*N*′-di(biphenyl-2-yl)-*N*,*N*′-diphenyl-[1,1′-biphenyl]-4,4′-diamine
PEDOT:PSS	Poly(2,3-dihydro-thieno-1,4-dioxin):poly(styrenesulfonate)
spiroTAD	2,2′,7,7′-tetrakis(*N*,*N*-diphenylamine)-9,9′-spirobifluorene
TAPC	Di-[4-(*N*,*N*-ditolyl-amino)phenyl]cyclohexane
TCTA	4,4′,4′′-tris(*N*-carbazolyl)triphenylamine
TPBi	1,3,5-tris(*N*-phenylbenzimidazol-2-yl)benzene
TPD	*N*,*N*′-Diphenyl-*N*,*N*′-di(3-tolyl)benzidine
TPDI	5,10,15-triphenyl-5*H*-diindolo[3,2-a:3′,2′-c]carbazole
TpPyPB	1,3,5-tri(*p*-pyrid-3-yl-phenyl)benzene

A.3 STANDARD PARAMETERS

Table A.1: LJ parameters of the DEPOSIT standard force field.

Atom	σ/nm	ϵ/kJ mol^{-1}
C	0.356	0.63
H	0.178	0.08
O	0.285	0.84
N	0.29	0.67
Al	0.35	0.276

Table A.2: Default parameters of the LightForge package.

Parameter	Value
α / nm^{-1}	0.1
j_0 / eV	0.001
ϵ	4
T / K	300

A.4 COMPUTING CHARGE CARRIER MOBILITY

Table A.3: Electronic properties and zero-field mobility computed in this work and reported in literature. The data presented in this table is published as SI to [A6]

Molecule	σ/meV	$\langle J^2 r^2 \rangle$/eV^2 Å^2	λ/meV	μ_0/cm^2 V^{-1} s^{-1}	Source
$Alq3_p$	199	1.0×10^{-2}	195	2.6×10^{-9}	SK
	224	1.0×10^{-2}	296	1.0×10^{-10}	PF
$Alq3_n$	182	8.6×10^{-3}	215	1.7×10^{-7}	SK
$TPBi_n$	164	2.5×10^{-3}	317	4.3×10^{-7}	SK
$BPBD_n$	182	5.2×10^{-3}	291	1.3×10^{-6}	SK
$DEPB_p$	133	2.4×10^{-3}	316	6.0×10^{-6}	SK
	130	1.4×10^{-3}	266	2.1×10^{-5}	PF
m-BPD_p	132	1.6×10^{-3}	210	8.8×10^{-6}	SK
	110	1.5×10^{-3}	143	7.4×10^{-4}	PF
			300	1.7×10^{-3}	DE
BCP_n	139	3.2×10^{-3}	314	1.4×10^{-5}	SK
				1.8×10^{-2}	PK
NNP_p	124	1.6×10^{-3}	281	1.2×10^{-5}	SK
	135	1.6×10^{-3}	160	4.3×10^{-5}	PF
$spiroTAD_p$	105	1.7×10^{-3}	139	8.7×10^{-5}	SK
	90		250	1.6×10^{-3}	NK
$TCTA_p$	107	1.7×10^{-3}	206	1.3×10^{-4}	SK
	136		257	7.2×10^{-7}	AM

Table A.3: (continued)

Molecule	σ/meV	$\langle J^2 r^2 \rangle$/eV^2 Å^2	λ/meV	μ_0/cm^2 V^{-1} s^{-1}	Source
	112		260	1.0×10^{-4}	NK
			290	5.9×10^{-4}	DE
NPB_p	104	1.4×10^{-3}	205	1.8×10^{-4}	SK
	130		203	6.9×10^{-7}	AM
	114			1.3×10^{-5}	PK
	144	2.0×10^{-3}	158	1.8×10^{-5}	PF
	87		310	1.1×10^{-3}	NK
			280	1.3×10^{-3}	DE
o-BPD_p	96	1.8×10^{-3}	213	3.2×10^{-4}	SK
			310	7.2×10^{-4}	DE
$TpPyPB_n$	123	6.4×10^{-3}	200	3.0×10^{-4}	SK
TPD_p	96	1.7×10^{-3}	208	7.9×10^{-4}	SK
	129	1.6×10^{-3}	110	1.5×10^{-4}	PF
			310	8.3×10^{-4}	DE
p-BPD_p	94	1.3×10^{-3}	173	7.0×10^{-4}	SK
			230	3.8×10^{-4}	DE
$TPDI_p$	82	4.8×10^{-3}	145	1.0×10^{-3}	SK
$TAPC_p$	74	1.4×10^{-3}	89	4.6×10^{-3}	SK

SK This work PK P. Kordt et al. [32] AM A. Massé et al. [37] DE D. Evans et al. [129]
PF P. Friederich et al. [104] NK N. Kotadiya et al. [38]

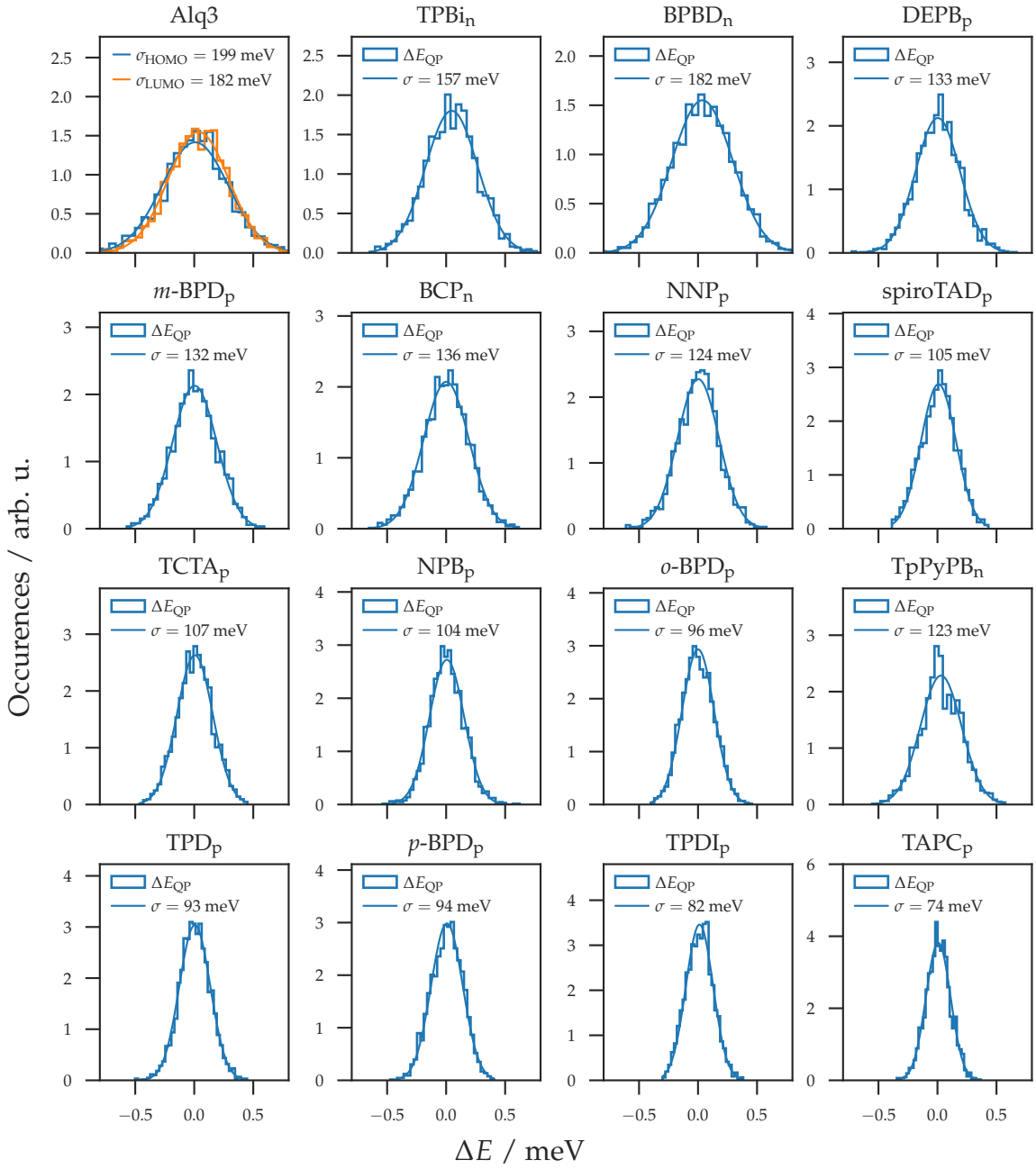

Figure A.1: Distribution of ΔE computed with the QP method, Gaussian fit and resulting disorder σ for all molecules studied in section 4.1.1. The data presented in this fig. is published as SI to [A6].

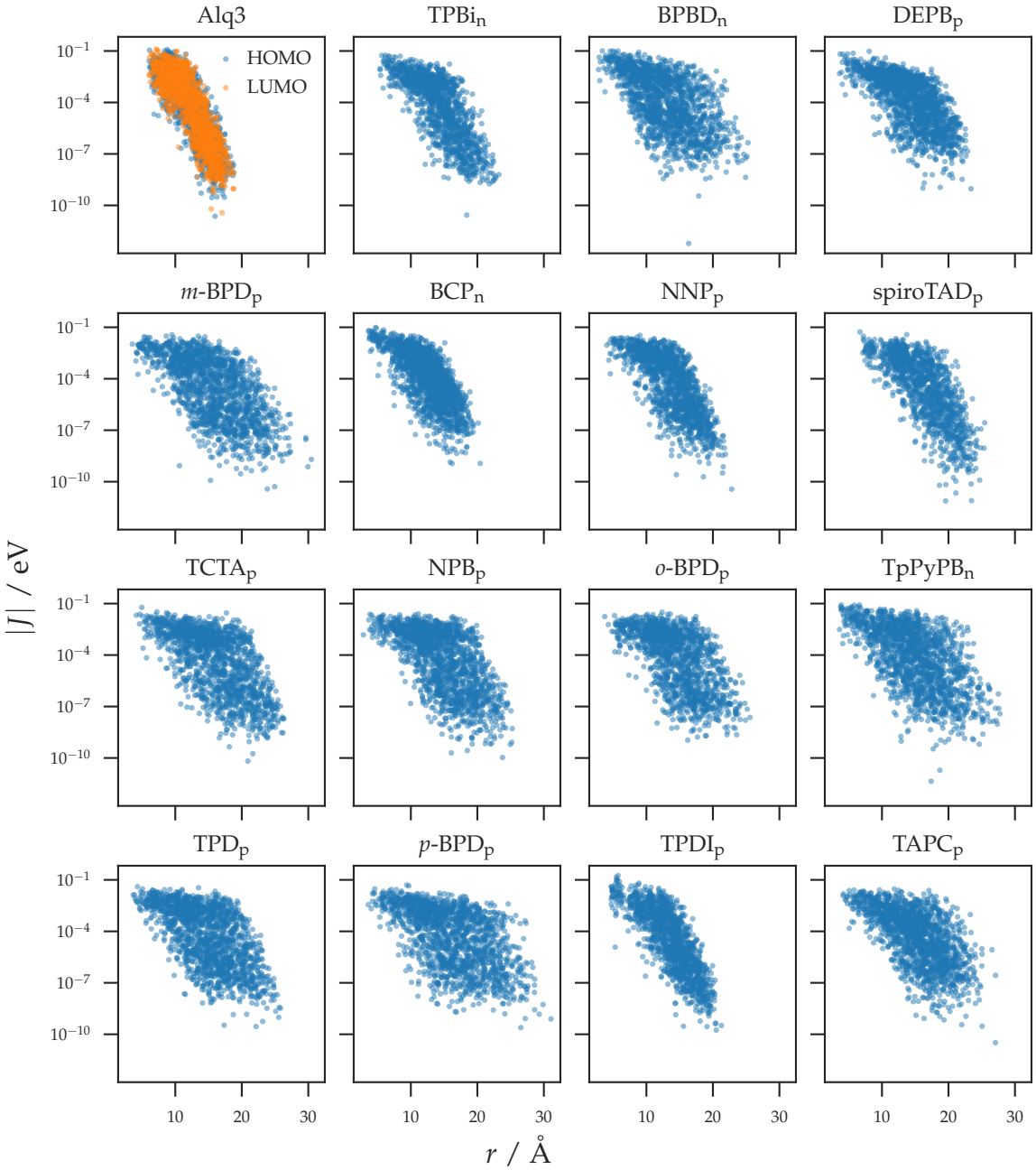

Figure A.2: Distribution of electronic couplings computed with the QP for all molecules studied in section 4.1.1. The data presented in this fig. is published as SI to [A6].

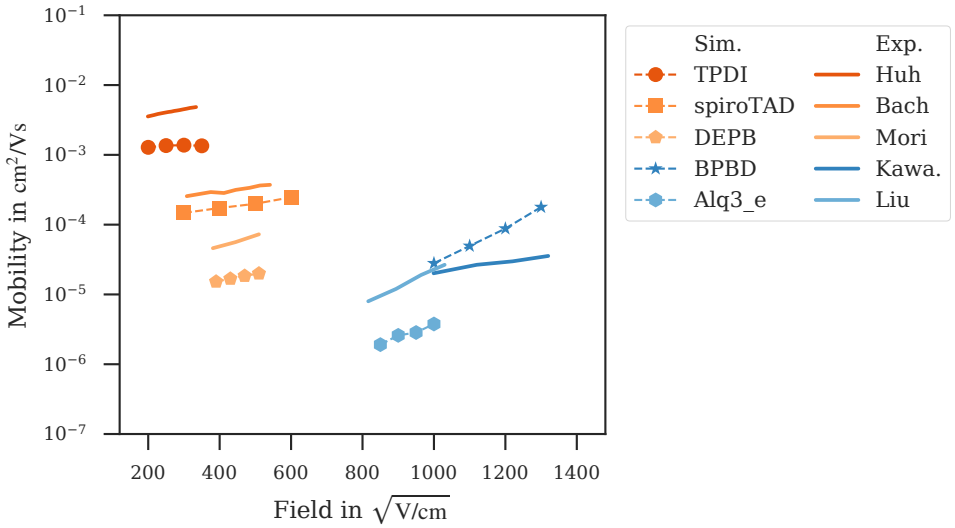

Figure A.3: Computed field-dependent mobilities of the materials not shown in figs. 4.5, 4.6 and 4.8 compared to experimental data reported in literature. Hole mobilities (orange) of TPDI [127], spiroTAD [123], DEPB [120] and electron mobilities (blue) of TpPyPB [126], BPBD [119] and Alq3 [117]. Simulation errors are of the order of symbol size. The data presented in this fig. is published as SI to [A6].

A.5 SENSITIVITY ANALYSIS

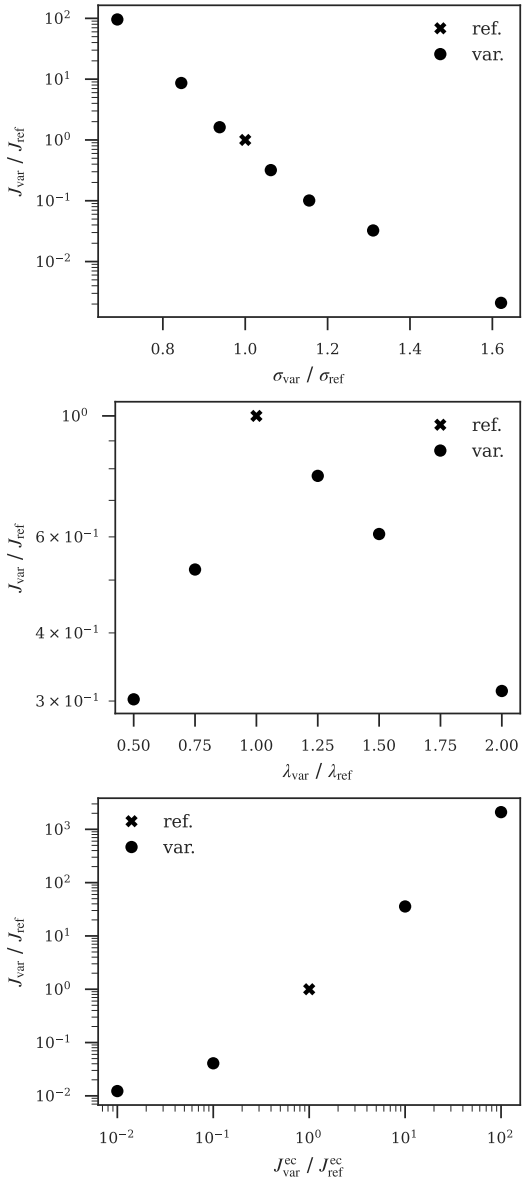

Figure A.4: Sensitivity of the current density J on variations of the microscopic input parameters, namely energetic disorder σ (top), reorganization energy λ (middle) and electronic couplings J^{ec} (bottom). The data presented in this fig. is published as SI to [A5].

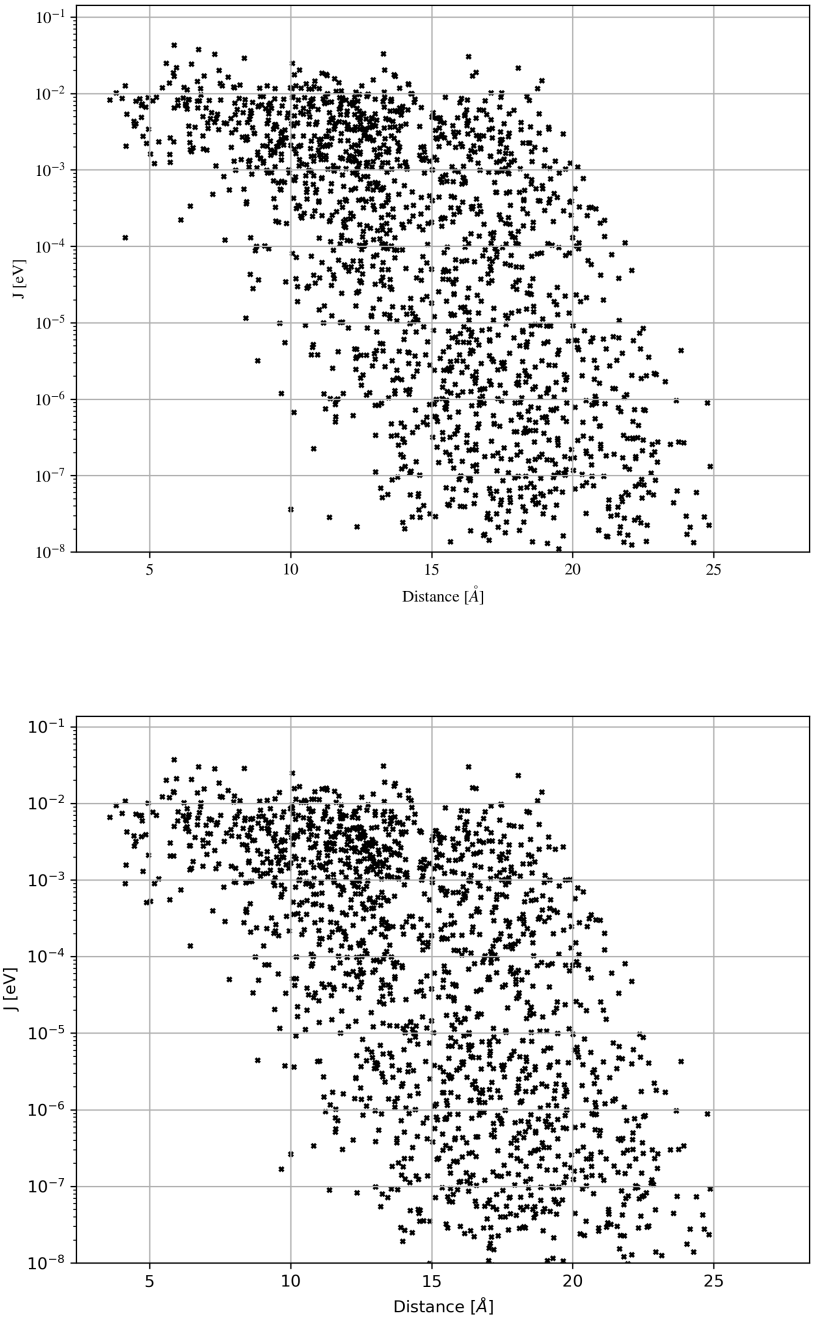

Figure A.5: Distribution of electronic couplings J_{ij} computed for α-NPD with the QP method using the BP86 (top) and B3LYP (bottom) functionals and def2-SVP basis set. As these minor differences only lead to small small deviations in the final current density (comp. w. fig. A.4), the BP86 functional offers a good compromise of computing time and accuracy. The data presented in this fig. is published as SI to [A6].

A.6 SIMULATING THE FULL OLED STACK

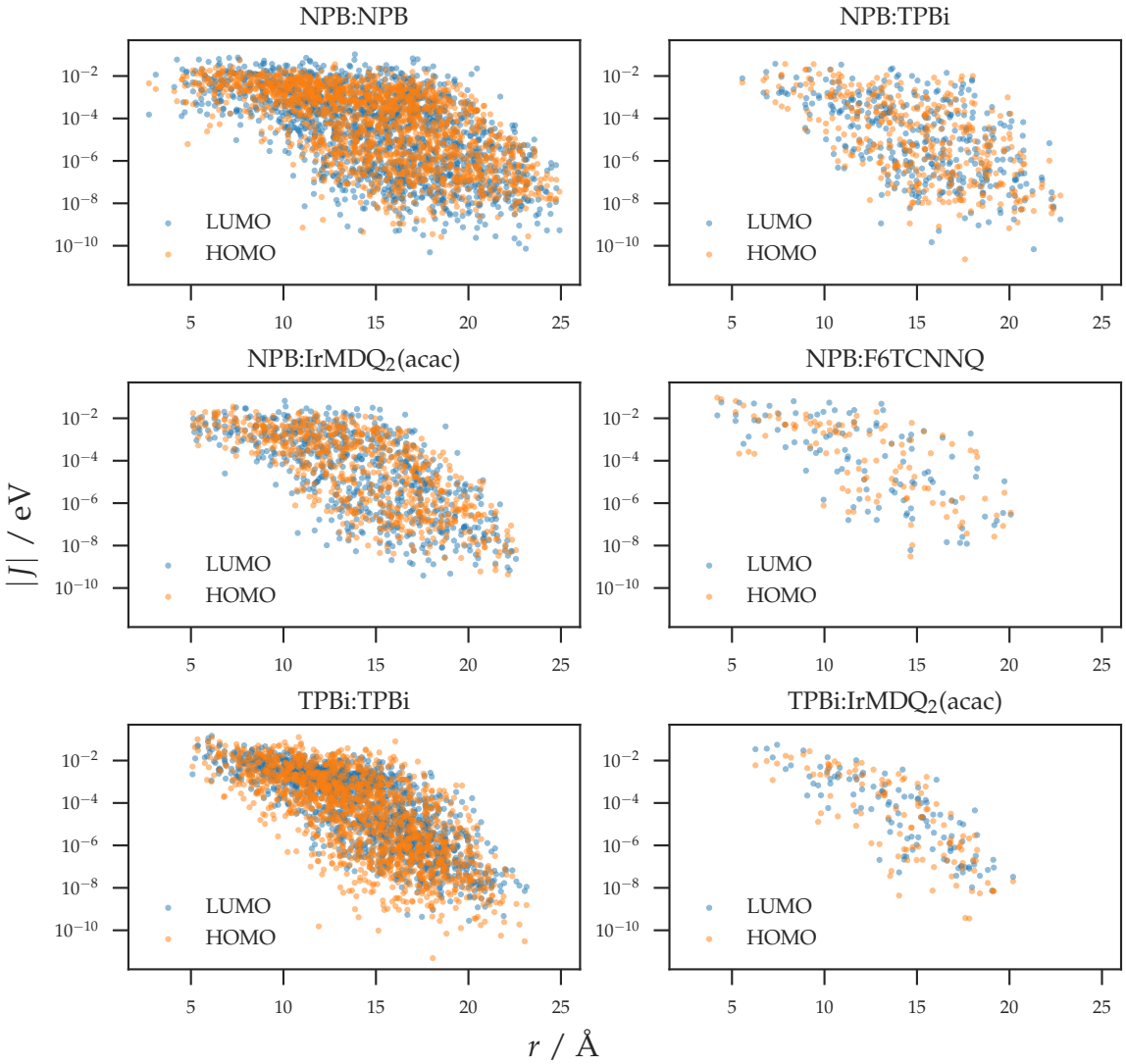

Figure A.6: Distribution of electronic couplings J_{ij} computed with the QP method for the material combinations NPB:NPB (HTL; host–host transport in DIL and EML), NPB:TPBi (transport at EML–ETL interface), NPB:Ir(MDQ)$_2$(acac) (guest–host transport in EML), NPB:F6TCNNQ (guest–host transport in DIL), TPBi:TPBi (ETL) and TPBi:Ir(MDQ)$_2$(acac) (transport at the EML–ETL interface).

Table A.4: Site densities N_0 of each material in the atomistic morphologies deposited in section 6.1.

Layer	Material	N_0/cm^{-3}
DIL	NPB	1.15×10^{21}
	F6TCNNQ	6.03×10^{19}
HTL	NPB	1.18×10^{21}
EML	NPB	1.06×10^{21}
	$Ir(MDQ)_2(acac)$	1.18×10^{20}
ETL	TPBi	1.07×10^{21}

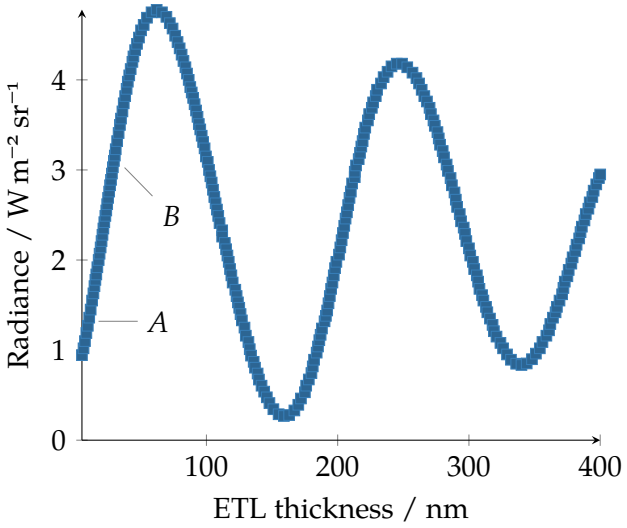

Figure A.7: Radiance depending on ETL thickness determined by IMEC. Annotations highlight the radiance of device variants *A* and *B* simulated in this work. The data presented in this figure was provided by IMEC as part of the EXTMOS project.

BIBLIOGRAPHY

[1] M. Fröbel, F. Fries, T. Schwab, S. Lenk, K. Leo, M. C. Gather and S. Reineke. 'Three-Terminal RGB Full-Color OLED Pixels for Ultrahigh Density Displays'. In: *Scientific Reports* 8.1 (2018), p. 9684. DOI: 10.1038/s41598-018-27976-z.

[2] D. Baran et al. 'Robust Nonfullerene Solar Cells Approaching Unity External Quantum Efficiency Enabled by Suppression of Geminate Recombination'. In: *Nature Communications* 9.1 (2018), p. 2059. DOI: 10.1038/s41467-018-04502-3.

[3] C. Wang et al. 'N-Type 2D Organic Single Crystals for High-Performance Organic Field-Effect Transistors and Near-Infrared Phototransistors'. In: *Advanced Materials* 30.16 (2018), p. 1706260. DOI: 10.1002/adma.201706260.

[4] D. Volz, M. Wallesch, C. Fléchon, M. Danz, A. Verma, J. M. Navarro, D. M. Zink, S. Bräse and T. Baumann. 'From iridium and platinum to copper and carbon: new avenues for more sustainability in organic light-emitting diodes'. In: *Green Chemistry* 17.4 (2015), pp. 1988–2011. DOI: 10.1039/C4GC02195A.

[5] H. Klauk. *Organic Electronics: Materials, Manufacturing, and Applications*. Weinheim: Wiley-VCH Verlag GmbH & Co. KGaA, 2006.

[6] T. Tsujimura. *OLED Display Fundamentals and Applications*. Second edition. Wiley Series in Display Technology. Hoboken, NJ: Wiley, 2017. 287 pp.

[7] T.-H. Han, Y. Lee, M.-R. Choi, S.-H. Woo, S.-H. Bae, B. H. Hong, J.-H. Ahn and T.-W. Lee. 'Extremely Efficient Flexible Organic Light-Emitting Diodes with Modified Graphene Anode'. In: *Nature Photonics* 6.2 (2012), pp. 105–110. DOI: 10.1038/nphoton.2011.318.

[8] P. Görrn, M. Sander, J. Meyer, M. Kröger, E. Becker, H.-H. Johannes, W. Kowalsky and T. Riedl. 'Towards See-Through Displays: Fully Transparent Thin-Film Transistors Driving Transparent Organic Light-Emitting Diodes'. In: *Advanced Materials* 18.6 (2006), pp. 738–741. DOI: 10.1002/adma.200501957.

[9] S.-M. Lee, J. H. Kwon, S. Kwon and K. C. Choi. 'A Review of Flexible OLEDs Toward Highly Durable Unusual Displays'. In: *IEEE Transactions on Electron Devices* 64.5 (2017), pp. 1922–1931. DOI: 10.1109/TED.2017.2647964.

[10] M. Pope, H. P. Kallmann and P. Magnante. 'Electroluminescence in Organic Crystals'. In: *The Journal of Chemical Physics* 38.8 (1963), pp. 2042–2043. DOI: 10.1063/1.1733929.

[11] W. Helfrich and W. G. Schneider. 'Recombination Radiation in Anthracene Crystals'. In: *Physical Review Letters* 14.7 (1965), pp. 229–231. DOI: 10.1103/PhysRevLett.14.229.

[12] C. W. Tang and S. A. VanSlyke. 'Organic Electroluminescent Diodes'. In: *Applied Physics Letters* 51 (1987), pp. 913–915. DOI: 10.1063/1.98799.

[13] J.-H. Jou, S. Kumar, A. Agrawal, T.-H. Li and S. Sahoo. 'Approaches for Fabricating High Efficiency Organic Light Emitting Diodes'. In: *Journal of Materials Chemistry C* 3.13 (2015), pp. 2974–3002. DOI: 10.1039/C4TC02495H.

[14] M. A. Baldo, D. F. O'Brien, Y. You, A. Shoustikov, S. Sibley, M. E. Thompson and S. R. Forrest. 'Highly Efficient Phosphorescent Emission from Organic Electroluminescent Devices'. In: *Nature* 395.6698 (6698 1998), pp. 151–154. DOI: 10.1038/25954.

[15] A. Endo, M. Ogasawara, A. Takahashi, D. Yokoyama, Y. Kato and C. Adachi. 'Thermally Activated Delayed Fluorescence from Sn^{4+}-Porphyrin Complexes and Their Application to Organic Light Emitting Diodes – A Novel Mechanism for Electroluminescence'. In: *Advanced Materials* 21.47 (2009), pp. 4802–4806. DOI: 10.1002/adma.200900983.

[16] B. Lüssem, C.-M. Keum, D. Kasemann, B. Naab, Z. Bao and K. Leo. 'Doped Organic Transistors'. In: *Chemical Reviews* 116.22 (2016), pp. 13714–13751. DOI: 10.1021/acs.chemrev.6b00329.

[17] M. Schwarze et al. 'Molecular parameters responsible for thermally activated transport in doped organic semiconductors'. In: *Nature Materials* 18.3 (2019), pp. 242–248. DOI: 10.1038/s41563-018-0277-0.

[18] C. Gaul, S. Hutsch, M. Schwarze, K. S. Schellhammer, F. Bussolotti, S. Kera, G. Cuniberti, K. Leo and F. Ortmann. 'Insight into doping efficiency of organic semiconductors from the analysis of the density of states in n-doped C_{60} and ZnPc'. In: *Nature*

Materials 17.5 (2018), pp. 439–444. DOI: 10.1038/s41563-018-0030-8.

[19] S.-J. Su, E. Gonmori, H. Sasabe and J. Kido. 'Highly Efficient Organic Blue-and White-Light-Emitting Devices Having a Carrier- and Exciton-Confining Structure for Reduced Efficiency Roll-Off'. In: *Advanced Materials* 20.21 (2008), pp. 4189–4194. DOI: 10.1002/adma.200801375.

[20] M. C. Gather, A. Köhnen and K. Meerholz. 'White Organic Light-Emitting Diodes'. In: *Advanced Materials* 23.2 (2011), pp. 233–248. DOI: 10.1002/adma.201002636.

[21] G. Hong, X. Gan, C. Leonhardt, Z. Zhang, J. Seibert, J. M. Busch and S. Bräse. 'A Brief History of OLEDs—Emitter Development and Industry Milestones'. In: *Advanced Materials* 33.9 (2021), p. 2005630. DOI: 10.1002/adma.202005630.

[22] Y. Li, J.-Y. Liu, Y.-D. Zhao and Y.-C. Cao. 'Recent Advancements of High Efficient Donor–Acceptor Type Blue Small Molecule Applied for OLEDs'. In: *Materials Today* 20.5 (2017), pp. 258–266. DOI: 10.1016/j.mattod.2016.12.003.

[23] M. Y. Wong and E. Zysman-Colman. 'Purely Organic Thermally Activated Delayed Fluorescence Materials for Organic Light-Emitting Diodes'. In: *Advanced Materials* 29.22 (2017), p. 1605444. DOI: 10.1002/adma.201605444.

[24] J.-H. Lee, C.-H. Chen, P.-H. Lee, H.-Y. Lin, M.-k. Leung, T.-L. Chiu and C.-F. Lin. 'Blue Organic Light-Emitting Diodes: Current Status, Challenges, and Future Outlook'. In: *Journal of Materials Chemistry C* 7.20 (2019), pp. 5874–5888. DOI: 10.1039/C9TC00204A.

[25] S.-J. Zou, Y. Shen, F.-M. Xie, J.-D. Chen, Y.-Q. Li and J.-X. Tang. 'Recent Advances in Organic Light-Emitting Diodes: Toward Smart Lighting and Displays'. In: *Materials Chemistry Frontiers* 4.3 (2020), pp. 788–820. DOI: 10.1039/C9QM00716D.

[26] S. Nam et al. 'Improved Efficiency and Lifetime of Deep-Blue Hyperfluorescent Organic Light-Emitting Diode Using Pt(II) Complex as Phosphorescent Sensitizer'. In: *Advanced Science* 8.16 (2021), p. 2100586. DOI: 10.1002/advs.202100586.

[27] S. Scholz, D. Kondakov, B. Lüssem and K. Leo. 'Degradation Mechanisms and Reactions in Organic Light-Emitting Devices'. In: *Chemical Reviews* 115.16 (2015), pp. 8449–8503. DOI: 10.1021/cr400704v.

[28] W. Song and J. Y. Lee. 'Degradation Mechanism and Lifetime Improvement Strategy for Blue Phosphorescent Organic Light-Emitting Diodes'. In: *Advanced Optical Materials* 5.9 (2017), p. 1600901. DOI: 10.1002/adom.201600901.

[29] P. Friederich et al. 'Rational In Silico Design of an Organic Semiconductor with Improved Electron Mobility'. In: *Advanced Materials* 29.43 (2017), p. 1703505. DOI: 10.1002/adma.201703505.

[30] L. Paterson, F. May and D. Andrienko. 'Computer Aided Design of Stable and Efficient OLEDs'. In: *Journal of Applied Physics* 128.16 (2020), p. 160901. DOI: 10.1063/5.0022870.

[31] E. Jansson, B. Minaev, S. Schrader and H. Ågren. 'Time-dependent density functional calculations of phosphorescence parameters for fac-tris(2-phenylpyridine) iridium'. In: *Chemical Physics* 333.2 (2007), pp. 157–167. DOI: 10.1016/j.chemphys.2007.01.021.

[32] P. Kordt, J. J. M. van der Holst, M. A. Helwi, W. Kowalsky, F. May, A. Badinski, C. Lennartz and D. Andrienko. 'Modeling of Organic Light Emitting Diodes: From Molecular to Device Properties'. In: *Advanced Functional Materials* 25.13 (2015), pp. 1955–1971. DOI: 10.1002/adfm.201403004.

[33] C. Groves. 'Simulating Charge Transport in Organic Semiconductors and Devices: A Review'. In: *Reports on Progress in Physics* 80.2 (2016), p. 026502. DOI: 10.1088/1361-6633/80/2/026502.

[34] F. Symalla, P. Friederich, A. Massé, V. Meded, R. Coehoorn, P. Bobbert and W. Wenzel. 'Charge Transport by Superexchange in Molecular Host-Guest Systems'. In: *Physical Review Letters* 117.27 (2016), p. 276803. DOI: 10.1103/PhysRevLett.117.276803.

[35] F. Liu, A. Massé, P. Friederich, F. Symalla, R. Nitsche, W. Wenzel, R. Coehoorn and P. A. Bobbert. 'Ab initio modeling of steady-state and time-dependent charge transport in hole-only α-NPD devices'. In: *Applied Physics Letters* 109.24 (2016), p. 243301. DOI: 10.1063/1.4971969.

[36] M. Mesta et al. 'Molecular-scale Simulation of Electroluminescence in a Multilayer White Organic Light-emitting Diode'. In: *Nature Materials* 12.7 (2013), pp. 652–658. DOI: 10.1038/nmat3622.

[37] A. Massé, P. Friederich, F. Symalla, F. Liu, R. Nitsche, R. Coehoorn, W. Wenzel and P. A. Bobbert. 'Ab Initio Charge-Carrier Mobility Model for Amorphous Molecular Semiconductors'. In:

Physical Review B 93.19 (2016), p. 195209. DOI: 10.1103/PhysRevB.93.195209.

[38] N. B. Kotadiya, A. Mondal, S. Xiong, P. W. M. Blom, D. Andrienko and G.-J. A. H. Wetzelaer. 'Rigorous Characterization and Predictive Modeling of Hole Transport in Amorphous Organic Semiconductors'. In: *Advanced Electronic Materials* 4.12 (2018), p. 1800366. DOI: 10.1002/aelm.201800366.

[39] F. Symalla, S. Heidrich, P. Friederich, T. Strunk, T. Neumann, D. Minami, D. Jeong and W. Wenzel. 'Multiscale Simulation of Photoluminescence Quenching in Phosphorescent OLED Materials'. In: *Advanced Theory and Simulations* 3.4 (2020), p. 1900222. DOI: 10.1002/adts.201900222.

[40] Y. Shen. 'Monte Carlo Simulations of Nanoscale Electrical Inhomogeneity in Organic Light-Emitting Diodes and Its Impact on Their Efficiency and Lifetime'. In: *Physical Review Applied* 4.5 (2015). DOI: 10.1103/PhysRevApplied.4.054017.

[41] W. M. Young and E. W. Elcock. 'Monte Carlo Studies of Vacancy Migration in Binary Ordered Alloys: I'. In: *Proceedings of the Physical Society* 89.3 (1966), p. 735. DOI: 10.1088/0370-1328/89/3/329.

[42] P. W. Atkins and J. de Paula. *Physikalische Chemie*. John Wiley & Sons, 2013.

[43] H. Bässler. 'Localized States and Electronic Transport in Single Component Organic Solids with Diagonal Disorder'. In: *Physica Status Solidi B* 107.1 (1981), pp. 9–54. DOI: 10.1002/pssb.2221070102.

[44] H. Bässler. 'Charge Transport in Disordered Organic Photoconductors a Monte Carlo Simulation Study'. In: *Physica Status Solidi B* 175.1 (1993), pp. 15–56. DOI: 10.1002/pssb.2221750102.

[45] R. H. Young. 'Dipolar Lattice Model of Disorder in Random Media Analytical Evaluation of the Gaussian Disorder Model'. In: *Philosophical Magazine B* 72.4 (1995), pp. 435–457. DOI: 10.1080/13642819508239097.

[46] R. Schmechel. 'Gaussian Disorder Model for High Carrier Densities: Theoretical Aspects and Application to Experiments'. In: *Physical Review B* 66.23 (2002). DOI: 10.1103/PhysRevB.66.235206.

[47] R. Coehoorn, W. F. Pasveer, P. A. Bobbert and M. A. J. Michels. 'Charge-Carrier Concentration Dependence of the Hopping Mobility in Organic Materials with Gaussian Disorder'. In: *Physical Review B* 72.15 (2005). DOI: 10.1103/PhysRevB.72.155206.

[48] P. W. Anderson. 'Absence of Diffusion in Certain Random Lattices'. In: *Physical Review* 109.5 (1958), pp. 1492–1505. DOI: 10.1103/PhysRev.109.1492.

[49] V. Coropceanu, J. Cornil, D. A. da Silva Filho, Y. Olivier, R. Silbey and J.-L. Brédas. 'Charge Transport in Organic Semiconductors'. In: *Chemical Reviews* 107.4 (2007), pp. 926–952. DOI: 10.1021/cr050140x.

[50] A. V. Nenashev, J. O. Oelerich and S. D. Baranovskii. 'Theoretical Tools for the Description of Charge Transport in Disordered Organic Semiconductors'. In: *Journal of Physics: Condensed Matter* 27.9 (2015), p. 093201. DOI: 10.1088/0953-8984/27/9/093201.

[51] X. de Vries. 'Full Quantum Treatment of Charge Dynamics in Amorphous Molecular Semiconductors'. In: *Physical Review B* 97.7 (2018). DOI: 10.1103/PhysRevB.97.075203.

[52] L. Wang, A. Akimov and O. V. Prezhdo. 'Recent Progress in Surface Hopping: 2011–2015'. In: *The Journal of Physical Chemistry Letters* 7.11 (2016), pp. 2100–2112. DOI: 10.1021/acs.jpclett.6b00710.

[53] L. Wang, J. Qiu, X. Bai and J. Xu. 'Surface Hopping Methods for Nonadiabatic Dynamics in Extended Systems'. In: *WIREs Computational Molecular Science* 10.2 (2020), e1435. DOI: 10.1002/wcms.1435.

[54] H. Oberhofer, K. Reuter and J. Blumberger. 'Charge Transport in Molecular Materials: An Assessment of Computational Methods'. In: *Chemical Reviews* 117.15 (2017), pp. 10319–10357. DOI: 10.1021/acs.chemrev.7b00086.

[55] A. Carof, S. Giannini and J. Blumberger. 'How to calculate charge mobility in molecular materials from surface hopping non-adiabatic molecular dynamics – beyond the hopping/band paradigm'. In: *Physical Chemistry Chemical Physics* 21.48 (2019), pp. 26368–26386. DOI: 10.1039/C9CP04770K.

[56] A. Miller and E. Abrahams. 'Impurity Conduction at Low Concentrations'. In: *Physical Review* 120.3 (1960), pp. 745–755. DOI: 10.1103/PhysRev.120.745.

[57] R. A. Marcus. 'On the Theory of Oxidation-Reduction Reactions Involving Electron Transfer. I'. In: *The Journal of Chemical Physics* 24.5 (1956), pp. 966–978. DOI: 10.1063/1.1742723.

[58] S. Arrhenius. 'Über die Dissociationswärme und den Einfluss der Temperatur auf den Dissociationsgrad der Elektrolyte'. In: *Zeitschrift für Physikalische Chemie* 4U.1 (1889), pp. 96–116. DOI: 10.1515/zpch-1889-0408.

[59] S. Arrhenius. 'Über die Reaktionsgeschwindigkeit bei der Inversion von Rohrzucker durch Säuren'. In: *Zeitschrift für Physikalische Chemie* 4U.1 (1889), pp. 226–248. DOI: 10.1515/zpch-1889-0416.

[60] R. A. Marcus. 'Electrostatic Free Energy and Other Properties of States Having Nonequilibrium Polarization. I'. In: *The Journal of Chemical Physics* 24.5 (1956), pp. 979–989. DOI: 10.1063/1.1742724.

[61] S. M. Sze and M.-K. Lee. *Semiconductor Devices: Physics and Technology*. 3rd ed. Hoboken, N.J: Wiley, 2012. 592 pp.

[62] N. W. Ashcroft and N. D. Mermin. *Solid State Physics*. XXI. South Melbourne: Brooks/Cole Thomson Learning, 2005.

[63] Y. Roichman and N. Tessler. 'Generalized Einstein Relation for Disordered Semiconductors—Implications for Device Performance'. In: *Applied Physics Letters* 80.11 (2002), pp. 1948–1950. DOI: 10.1063/1.1461419.

[64] M. Pope and C. E. Swenberg. *Electronic Processes in Organic Crystals and Polymers*. New York: Oxford University Press, 1999.

[65] A. Köhler and H. Bässler. *Electronic Processes in Organic Semiconductors: An Introduction*. Weinheim: Wiley-VCH Verlag GmbH & Co. KGaA, 2015.

[66] T. Förster. 'Zwischenmolekulare Energiewanderung und Fluoreszenz'. In: *Annalen der Physik* 437.1-2 (1948), pp. 55–75. DOI: 10.1002/andp.19484370105.

[67] B. Fückel, A. Köhn, M. E. Harding, G. Diezemann, G. Hinze, T. Basché and J. Gauss. 'Theoretical Investigation of Electronic Excitation Energy Transfer in Bichromophoric Assemblies'. In: *The Journal of Chemical Physics* 128.7 (2008), p. 074505. DOI: 10.1063/1.2829531.

[68] D. L. Dexter. 'A Theory of Sensitized Luminescence in Solids'. In: *Journal of Chemical Physics* 21 (1953), pp. 836–850. DOI: 10.1063/1.1699044.

[69] M. A. Baldo, S. Lamansky, P. E. Burrows, M. E. Thompson and S. R. Forrest. 'Very High-Efficiency Green Organic Light-Emitting Devices Based on Electrophosphorescence'. In: *Applied Physics Letters* 75.1 (1999), pp. 4–6. DOI: 10.1063/1.124258.

[70] H. Yersin, A. F. Rausch, R. Czerwieniec, T. Hofbeck and T. Fischer. 'The Triplet State of Organo-Transition Metal Compounds. Triplet Harvesting and Singlet Harvesting for Efficient OLEDs'. In: *Coordination Chemistry Reviews*. Controlling Photophysical Properties of Metal Complexes: Towards Molecular Photonics 255.21 (2011), pp. 2622–2652. DOI: 10.1016/j.ccr.2011.01.042.

[71] G. He, O. Schneider, D. Qin, X. Zhou, M. Pfeiffer and K. Leo. 'Very high-efficiency and low voltage phosphorescent organic light-emitting diodes based on a p-i-n junction'. In: *Journal of Applied Physics* 95.10 (2004), pp. 5773–5777. DOI: 10.1063/1.1702143.

[72] B. Geffroy, P. le Roy and C. Prat. 'Organic Light-Emitting Diode (OLED) Technology: Materials, Devices and Display Technologies'. In: *Polymer International* 55.6 (2006), pp. 572–582. DOI: 10.1002/pi.1974.

[73] M. Born and R. Oppenheimer. 'Zur Quantentheorie Der Molekeln'. In: *Annalen der Physik* 389.20 (1927), pp. 457–484. DOI: 10.1002/andp.19273892002.

[74] R. M. Dreizler and E. K. U. Groß. *Density Functional Theory: An Approach to the Quantum Many-Body Problem*. Berlin, Heidelberg: Springer, 1990. DOI: 10.1007/978-3-642-86105-5.

[75] P. Hohenberg and W. Kohn. 'Inhomogeneous Electron Gas'. In: *Physical Review* 136.3B (1964), B864–B871. DOI: 10.1103/PhysRev.136.B864.

[76] W. Kohn and L. J. Sham. 'Self-Consistent Equations Including Exchange and Correlation Effects'. In: *Physical Review* 140.4A (1965), A1133–A1138. DOI: 10.1103/PhysRev.140.A1133.

[77] A. D. Becke. 'Density-Functional Exchange-Energy Approximation with Correct Asymptotic Behavior'. In: *Physical Review A* 38.6 (1988), pp. 3098–3100. DOI: 10.1103/PhysRevA.38.3098.

[78] J. P. Perdew. 'Density-Functional Approximation for the Correlation Energy of the Inhomogeneous Electron Gas'. In: *Physical Review B* 33.12 (1986), pp. 8822–8824. DOI: 10.1103/PhysRevB.33.8822.

[79] P. J. Stephens, F. J. Devlin, C. F. Chabalowski and M. J. Frisch. 'Ab Initio Calculation of Vibrational Absorption and Circular Dichroism Spectra Using Density Functional Force Fields'. In: *The Journal of Physical Chemistry* 98.45 (1994), pp. 11623–11627. DOI: 10.1021/j100096a001.

[80] F. Weigend and R. Ahlrichs. 'Balanced Basis Sets of Split Valence, Triple Zeta Valence and Quadruple Zeta Valence Quality for H to Rn: Design and Assessment of Accuracy'. In: *Physical Chemistry Chemical Physics* 7.18 (2005), pp. 3297–3305. DOI: 10.1039/B508541A.

[81] W. F. Pasveer, J. Cottaar, C. Tanase, R. Coehoorn, P. A. Bobbert, P. W. M. Blom, D. M. de Leeuw and M. A. J. Michels. 'Unified Description of Charge-Carrier Mobilities in Disordered Semiconducting Polymers'. In: *Physical Review Letters* 94.20 (2005), p. 206601. DOI: 10.1103/PhysRevLett.94.206601.

[82] J. Cottaar, L. J. A. Koster, R. Coehoorn and P. A. Bobbert. 'Scaling Theory for Percolative Charge Transport in Disordered Molecular Semiconductors'. In: *Physical Review Letters* 107.13 (2011), p. 136601. DOI: 10.1103/PhysRevLett.107.136601.

[83] A. Massé, R. Coehoorn and P. A. Bobbert. 'Universal Size-Dependent Conductance Fluctuations in Disordered Organic Semiconductors'. In: *Physical Review Letters* 113.11 (2014), p. 116604. DOI: 10.1103/PhysRevLett.113.116604.

[84] T. Neumann, D. Danilov, C. Lennartz and W. Wenzel. 'Modeling Disordered Morphologies in Organic Semiconductors'. In: *Journal of Computational Chemistry* 34.31 (2013), pp. 2716–2725. DOI: 10.1002/jcc.23445.

[85] P. Friederich, F. Symalla, V. Meded, T. Neumann and W. Wenzel. 'Ab Initio Treatment of Disorder Effects in Amorphous Organic Materials: Toward Parameter Free Materials Simulation'. In: *Journal of Chemical Theory and Computation* 10.9 (2014), pp. 3720–3725. DOI: 10.1021/ct500418f.

[86] B. Baumeier, O. Stenzel, C. Poelking, D. Andrienko and V. Schmidt. 'Stochastic Modeling of Molecular Charge Transport Networks'. In: *Physical Review B* 86.18 (2012), p. 184202. DOI: 10.1103/PhysRevB.86.184202.

[87] T. Strunk et al. 'SIMONA 1.0: An Efficient and Versatile Framework for Stochastic Simulations of Molecular and Nanoscale Systems'. In: *Journal of Computational Chemistry* 33.32 (2012), pp. 2602–2613. DOI: 10.1002/jcc.23089.

[88] T. Strunk. 'High-Throughput Atomistic Modeling of Biomolecular Structure and Association'. PhD thesis. Karlsruher Institut für Technologie (KIT), 2012. DOI: 10.5445/IR/1000036224.

[89] T. Neumann. 'Modeling Structural and Electronic Properties of Nano-Scale Systems'. PhD thesis. Karlsruher Institut für Technologie (KIT), 2016. DOI: 10.5445/IR/1000055205.

[90] P. Friederich. 'Simulation of Charge Transport in Amorphous Organic Semiconductors'. PhD thesis. Karlsruher Institut für Technologie (KIT), 2016. DOI: 10.5445/IR/1000069385.

[91] F. Symalla. 'Modeling of Charge and Exciton Dynamics in Amorphous Organic Semiconductors'. PhD thesis. Karlsruher Institut für Technologie (KIT), 2018. DOI: 10.5445/IR/1000080716.

[92] U. C. Singh and P. A. Kollman. 'An Approach to Computing Electrostatic Charges for Molecules'. In: *Journal of Computational Chemistry* 5.2 (1984), pp. 129–145. DOI: 10.1002/jcc.540050204.

[93] W. K. Hastings. 'Monte Carlo Sampling Methods Using Markov Chains and Their Applications'. In: *Biometrika* 57.1 (1970), pp. 97–109. DOI: 10.1093/biomet/57.1.97.

[94] P. Friederich, V. Rodin, F. von Wrochem and W. Wenzel. 'Built-In Potentials Induced by Molecular Order in Amorphous Organic Thin Films'. In: *ACS Applied Materials & Interfaces* 10.2 (2018), pp. 1881–1887. DOI: 10.1021/acsami.7b11762.

[95] P.-O. Löwdin. 'On the Non-Orthogonality Problem Connected with the Use of Atomic Wave Functions in the Theory of Molecules and Crystals'. In: *The Journal of Chemical Physics* 18.3 (1950), pp. 365–375. DOI: 10.1063/1.1747632.

[96] V. Stehr, J. Pfister, R. F. Fink, B. Engels and C. Deibel. 'First-Principles Calculations of Anisotropic Charge-Carrier Mobilities in Organic Semiconductor Crystals'. In: *Physical Review B* 83.15 (2011), p. 155208. DOI: 10.1103/PhysRevB.83.155208.

[97] S. F. Nelsen, S. C. Blackstock and Y. Kim. 'Estimation of Inner Shell Marcus Terms for Amino Nitrogen Compounds by Molecular Orbital Calculations'. In: *Journal of the American Chemical Society* 109.3 (1987), pp. 677–682. DOI: 10.1021/ja00237a007.

[98] A. Dieckmann, H. Bässler and P. M. Borsenberger. 'An Assessment of the Role of Dipoles on the Density-of-states Function of Disordered Molecular Solids'. In: *The Journal of Chemical Physics* 99.10 (1993), pp. 8136–8141. DOI: 10.1063/1.465640.

[99] Y. Gartstein and E. Conwell. 'High-Field Hopping Mobility in Molecular Systems with Spatially Correlated Energetic Disorder'. In: *Chemical Physics Letters* 245.4-5 (1995), pp. 351–358. DOI: 10.1016/0009-2614(95)01031-4.

[100] M. Bouhassoune, S. L. M. van Mensfoort, P. A. Bobbert and R. Coehoorn. 'Carrier-Density and Field-Dependent Charge-Carrier Mobility in Organic Semiconductors with Correlated Gaussian Disorder'. In: *Organic Electronics* 10.3 (2009), pp. 437–445. DOI: 10.1016/j.orgel.2009.01.005.

[101] H. Yoshida. 'Near-Ultraviolet Inverse Photoemission Spectroscopy Using Ultra-Low Energy Electrons'. In: *Chemical Physics Letters* 539–540 (2012), pp. 180–185. DOI: 10.1016/j.cplett.2012.04.058.

[102] H. Bronstein, C. B. Nielsen, B. C. Schroeder and I. McCulloch. 'The Role of Chemical Design in the Performance of Organic Semiconductors'. In: *Nature Reviews Chemistry* 4.2 (2 2020), pp. 66–77. DOI: 10.1038/s41570-019-0152-9.

[103] K. Zojer. 'Simulation of Charge Carriers in Organic Electronic Devices: Methods with Their Fundamentals and Applications'. In: *Advanced Optical Materials* 9.14 (2021), p. 2100219. DOI: 10.1002/adom.202100219.

[104] P. Friederich et al. 'Molecular Origin of the Charge Carrier Mobility in Small Molecule Organic Semiconductors'. In: *Advanced Functional Materials* 26.31 (2016), pp. 5757–5763. DOI: 10.1002/adfm.201601807.

[105] V. Rodin, F. Symalla, V. Meded, P. Friederich, D. Danilov, A. Poschlad, G. Nelles, F. von Wrochem and W. Wenzel. 'Generalized Effective-Medium Model for the Carrier Mobility in Amorphous Organic Semiconductors'. In: *Physical Review B* 91.15 (2015), p. 155203. DOI: 10.1103/PhysRevB.91.155203.

[106] M. Casalegno, G. Raos and R. Po. 'Methodological Assessment of Kinetic Monte Carlo Simulations of Organic Photovoltaic Devices: The Treatment of Electrostatic Interactions'. In: *The Journal of Chemical Physics* 132.9 (2010), p. 094705. DOI: 10.1063/1.3337909.

[107] J. J. M. van der Holst, F. W. A. van Oost, R. Coehoorn and P. A. Bobbert. 'Monte Carlo Study of Charge Transport in Organic Sandwich-Type Single-Carrier Devices: Effects of Coulomb Interactions'. In: *Physical Review B* 83.8 (2011), p. 085206. DOI: 10.1103/PhysRevB.83.085206.

[108] M. Casalegno, A. Bernardi and G. Raos. 'Numerical Simulation of Photocurrent Generation in Bilayer Organic Solar Cells: Comparison of Master Equation and Kinetic Monte Carlo Approaches'. In: *The Journal of Chemical Physics* 139.2 (2013), p. 024706. DOI: 10.1063/1.4812826.

[109] F. Liu, H. van Eersel, B. Xu, J. G. E. Wilbers, M. P. de Jong, W. G. van der Wiel, P. A. Bobbert and R. Coehoorn. 'Effect of Coulomb Correlation on Charge Transport in Disordered Organic Semiconductors'. In: *Physical Review B* 96.20 (2017), p. 205203. DOI: 10.1103/PhysRevB.96.205203.

[110] R. Ahlrichs, M. Bär, M. Häser, H. Horn and C. Kölmel. 'Electronic structure calculations on workstation computers: The program system TURBOMOLE'. In: *Chemical Physics Letters* 162.3 (1989), pp. 165–169. DOI: 10.1016/0009-2614(89)85118-8.

[111] R. G. Kepler. 'Charge Carrier Production and Mobility in Anthracene Crystals'. In: *Physical Review* 119.4 (1960), pp. 1226–1229. DOI: 10.1103/PhysRev.119.1226.

[112] R. G. Kepler, P. M. Beeson, S. J. Jacobs, R. A. Anderson, M. B. Sinclair, V. S. Valencia and P. A. Cahill. 'Electron and hole mobility in tris(8-hydroxyquinolinolato-*N*1,*O*8) aluminum'. In: *Applied Physics Letters* 66.26 (1995), pp. 3618–3620. DOI: 10.1063/1.113806.

[113] N. F. Mott and R. W. Gurney. *Electronic Processes in Ionic Crystals*. 2.ed. The International Series of Monographs on Physics. Oxford: Clarendon Pr., 1957. XII, 275 S. : graph. Darst.

[114] P. N. Murgatroyd. 'Theory of Space-Charge-Limited Current Enhanced by Frenkel Effect'. In: 3.2 (1970), pp. 151–156. DOI: 10.1088/0022-3727/3/2/308.

[115] J. C. Blakesley, F. A. Castro, W. Kylberg, G. F. A. Dibb, C. Arantes, R. Valaski, M. Cremona, J. S. Kim and J.-S. Kim. 'Towards Reliable Charge-Mobility Benchmark Measurements for Organic Semiconductors'. In: *Organic Electronics* 15.6 (2014), pp. 1263–1272. DOI: 10.1016/j.orgel.2014.02.008.

[116] S. Naka, H. Okada, H. Onnagawa, J. Kido and T. Tsutsui. 'Time-of-Flight Measurement of Hole Mobility in Aluminum (III) Complexes'. In: *Japanese Journal of Applied Physics* 38.11A (1999), p. L1252. DOI: 10.1143/JJAP.38.L1252.

[117] S.-W. Liu, C.-C. Lee, C.-F. Lin, J.-C. Huang, C.-T. Chen and J.-H. Lee. '4-hydroxy-8-methyl-1,5-naphthyridine aluminium chelate: a morphologically stable and efficient exciton-blocking material for organic photovoltaics with prolonged lifetime'. In: *Journal of Materials Chemistry* 20.36 (2010), pp. 7800–7806. DOI: 10.1039/C0JM01049A.

[118] W.-Y. Hung, T.-H. Ke, Y.-T. Lin, C.-C. Wu, T.-H. Hung, T.-C. Chao, K.-T. Wong and C.-I. Wu. 'Employing Ambipolar Oligofluorene as the Charge-Generation Layer in Time-of-Flight Mobility Measurements of Organic Thin Films'. In: *Applied Physics Letters* 88.6 (2006), p. 064102. DOI: 10.1063/1.2172708.

[119] Y. Kawabe and J. Abe. 'Electron Mobility Measurement Using Exciplex-Type Organic Light-Emitting Diodes'. In: *Applied Physics Letters* 81.3 (2002), pp. 493–495. DOI: 10.1063/1.1494105.

[120] T. Mori, E. Sugimura and T. Mizutani. 'Estimate of Hole Mobilities of Some Organic Photoconducting Materials Using the Time-of-Flight Method'. In: *Journal of Physics D: Applied Physics* 26.3 (1993), pp. 452–455. DOI: 10.1088/0022-3727/26/3/017.

[121] K. Okumoto, K. Wayaku, T. Noda, H. Kageyama and Y. Shirota. 'Amorphous molecular materials: charge transport in the glassy state of *N*,*N*′-di(biphenylyl)-*N*,*N*′-diphenyl-[1,1′-biphenyl]-4,4′-diamines'. In: *Synthetic Metals* 111–112 (2000), pp. 473–476. DOI: 10.1016/S0379-6779(99)00421-X.

[122] P. M. Borsenberger and J. Shi. 'Hole Transport in a Vapor Deposited Phenylenediamine Molecular Glass'. In: *Physica Status Solidi B* 191.2 (1995), pp. 461–469. DOI: 10.1002/pssb.2221910219.

[123] U. Bach, K. D. Cloedt, H. Spreitzer and M. Grätzel. 'Characterization of Hole Transport in a New Class of Spiro-Linked Oligotriphenylamine Compounds'. In: *Advanced Materials* 12.14 (2000), pp. 1060–1063. DOI: 10.1002/1521-4095(200007)12:14<1060::AID-ADMA1060>3.0.CO;2-R.

[124] S. Noh, C. K. Suman, Y. Hong and C. Lee. 'Carrier Conduction Mechanism for Phosphorescent Material Doped Organic Semiconductor'. In: *Journal of Applied Physics* 105.3 (2009), p. 033709. DOI: 10.1063/1.3072693.

[125] S. Naka, H. Okada, H. Onnagawa, Y. Yamaguchi and T. Tsutsui. 'Carrier Transport Properties of Organic Materials for EL Device Operation'. In: *Synthetic Metals* 111–112 (2000), pp. 331–333. DOI: 10.1016/S0379-6779(99)00358-6.

[126] S.-J. Su, T. Chiba, T. Takeda and J. Kido. 'Pyridine-Containing Triphenylbenzene Derivatives with High Electron Mobility for Highly Efficient Phosphorescent OLEDs'. In: *Advanced Materials* 20.11 (2008), pp. 2125–2130. DOI: 10.1002/adma.200701730.

[127] D. H. Huh, G. W. Kim, G. H. Kim, C. Kulshreshtha and J. H. Kwon. 'High Hole Mobility Hole Transport Material for Organic Light-Emitting Devices'. In: *Synthetic Metals* 180 (2013), pp. 79–84. DOI: 10.1016/j.synthmet.2013.07.021.

[128] P. M. Borsenberger, L. Pautmeier, R. Richert and H. Bässler. 'Hole transport in 1,1-bis(di-4-tolylaminophenyl)cyclohexane'. In: *The Journal of Chemical Physics* 94.12 (1991), pp. 8276–8281. DOI: 10.1063/1.460112.

[129] D. R. Evans, H. S. Kwak, D. J. Giesen, A. Goldberg, M. D. Halls and M. Oh-e. 'Estimation of Charge Carrier Mobility in Amorphous Organic Materials Using Percolation Corrected Random-Walk Model'. In: *Organic Electronics* 29 (2016), pp. 50–56. DOI: 10.1016/j.orgel.2015.11.021.

[130] A. Fuchs, T. Steinbrecher, M. S. Mommer, Y. Nagata, M. Elstner and C. Lennartz. 'Molecular origin of differences in hole and electron mobility in amorphous Alq_3—a multiscale simulation study'. In: *Physical Chemistry Chemical Physics* 14.12 (2012), pp. 4259–4270. DOI: 10.1039/C2CP23489K.

[131] G. Aydin and I. Yavuz. 'Intrinsic Static/Dynamic Energetic Disorders of Amorphous Organic Semiconductors: Microscopic Simulations and Device Study'. In: *The Journal of Physical Chemistry C* 125.12 (2021), pp. 6862–6869. DOI: 10.1021/acs.jpcc.0c11219.

[132] J. Frenkel. 'On Pre-Breakdown Phenomena in Insulators and Electronic Semi-Conductors'. In: *Physical Review* 54.8 (1938), pp. 647–648. DOI: 10.1103/PhysRev.54.647.

[133] L. Pautmeier, R. Richert and H. Bässler. 'Poole–Frenkel behavior of charge transport in organic solids with off-diagonal disorder studied by Monte Carlo simulation'. In: *Synthetic Metals*. Proceedings of the 21st Europhysics Conference on Macromolecular Physics 'Electrical and Optical Active Polymers" Structure, Morphology and Properties 37.1 (1990), pp. 271–281. DOI: 10.1016/0379-6779(90)90158-H.

[134] J. Armleder, T. Strunk, F. Symalla, P. Friederich, J. Enrique Olivares Peña, T. Neumann, W. Wenzel and A. Fediai. 'Computing Charging and Polarization Energies of Small Organic Molecules Embedded into Amorphous Materials with Quantum Accuracy'. In: *Journal of Chemical Theory and Computation* 17.6 (2021), pp. 3727–3738. DOI: 10.1021/acs.jctc.1c00036.

[135] K. Sugi, T. Ono, D. Kato, T. Yonehara, T. Sawabe, S. Enomoto and I. Amemiya. 'P-154L: Late-News Poster: High-efficacy OLED Panel with High-mobility Electron Transport Layers for New Lighting Applications'. In: *SID Symposium Digest of Technical Papers* 43.1 (2012), pp. 1548–1550. DOI: 10.1002/j.2168-0159.2012.tb06111.x.

[136] Q. Zhang, B. Wang, J. Tan, G. Mu, W. Yi, X. Lv, S. Zhuang, W. Liu and L. Wang. 'Optimized Electron-Transport Material Based on m-Terphenyl-Diphenylphosphine Oxide with the Harmonious Compatibility of High ET and Electron Mobility for Highly Efficient OLEDs'. In: *Journal of Materials Chemistry C* 5.33 (2017), pp. 8516–8526. DOI: 10.1039/C7TC02459B.

[137] G. Lin et al. 'Improving Electron Mobility of Tetraphenylethene-Based AIEgens to Fabricate Nondoped Organic Light-Emitting Diodes with Remarkably High Luminance and Efficiency'. In: *ACS Applied Materials & Interfaces* 8.26 (2016), pp. 16799–16808. DOI: 10.1021/acsami.6b04924.

[138] R. A. Klenkler, H. Aziz, A. Tran, Z. D. Popovic and G. Xu. 'High Electron Mobility Triazine for Lower Driving Voltage and Higher Efficiency Organic Light Emitting Devices'. In: *Organic Electronics* 9.3 (2008), pp. 285–290. DOI: 10.1016/j.orgel.2007.11.004.

[139] D. P. Tabor, V. A. Chiykowski, P. Friederich, Y. Cao, D. J. Dvorak, C. P. Berlinguette and A. Aspuru-Guzik. 'Design Rules for High Mobility Xanthene-Based Hole Transport Materials'. In: *Chemical Science* 10.36 (2019), pp. 8360–8366. DOI: 10.1039/C9SC01491H.

[140] H. Sasabe and J. Kido. 'Multifunctional Materials in High-Performance OLEDs: Challenges for Solid-State Lighting'. In: *Chemistry of Materials* 23.3 (2011), pp. 621–630. DOI: 10.1021/cm1024052.

[141] T. N. Ng, W. R. Silveira and J. A. Marohn. 'Dependence of Charge Injection on Temperature, Electric Field, and Energetic Disorder in an Organic Semiconductor'. In: *Physical Review Letters* 98.6 (2007), p. 066101. DOI: 10.1103/PhysRevLett.98.066101.

[142] Y. Hirose, W. Chen, E. I. Haskal, S. R. Forrest and A. Kahn. 'Band Lineup at an Organic-inorganic Semiconductor Heterointerface: Perylenetetracarboxylic Dianhydride/GaAs(100)'. In: *Applied Physics Letters* 64.25 (1994), pp. 3482–3484. DOI: 10.1063/1.111247.

[143] S. M. Tadayyon, H. M. Grandin, K. Griffiths, L. L. Coatsworth, P. R. Norton, H. Aziz and Z. D. Popovic. 'Reliable and Reproducible Determination of Work Function and Ionization Potentials of Layers and Surfaces Relevant to Organic Light Emitting Diodes'. In: *Organic Electronics* 5.4 (2004), pp. 199–205. DOI: 10.1016/j.orgel.2003.12.002.

[144] H. Yoshida. 'Measuring the Electron Affinity of Organic Solids: An Indispensable New Tool for Organic Electronics'. In: *Analytical and Bioanalytical Chemistry* 406.9 (2014), pp. 2231–2237. DOI: 10.1007/s00216-014-7659-1.

[145] J. J. M. van der Holst, M. A. Uijttewaal, B. Ramachandhran, R. Coehoorn, P. A. Bobbert, G. A. de Wijs and R. A. de Groot. 'Modeling and Analysis of the Three-Dimensional Current Density in Sandwich-Type Single-Carrier Devices of Disordered Organic Semiconductors'. In: *Physical Review B* 79.8 (2009), p. 085203. DOI: 10.1103/PhysRevB.79.085203.

[146] P. W. M. Blom, M. J. M. de Jong and J. J. M. Vleggaar. 'Electron and Hole Transport in Poly(P-phenylene Vinylene) Devices'. In: *Applied Physics Letters* 68.23 (1996), pp. 3308–3310. DOI: 10.1063/1.116583.

[147] P. P. Ewald. 'Die Berechnung optischer und elektrostatischer Gitterpotentiale'. In: *Annalen der Physik* 369.3 (1921), pp. 253–287. DOI: 10.1002/andp.19213690304.

[148] M. Kröger, S. Hamwi, J. Meyer, T. Riedl, W. Kowalsky and A. Kahn. 'P-Type Doping of Organic Wide Band Gap Materials by Transition Metal Oxides: A Case-Study on Molybdenum Trioxide'. In: *Organic Electronics* 10.5 (2009), pp. 932–938. DOI: 10.1016/j.orgel.2009.05.007.

[149] A. Kahn, N. Koch and W. Gao. 'Electronic Structure and Electrical Properties of Interfaces between Metals and π-Conjugated Molecular Films'. In: *Journal of Polymer Science Part B: Polymer Physics* 41.21 (2003), pp. 2529–2548. DOI: 10.1002/polb.10642.

[150] R. T. White, E. S. Thibau and Z.-H. Lu. 'Interface Structure of MoO_3 on Organic Semiconductors'. In: *Scientific Reports* 6.1 (2016), p. 21109. DOI: 10.1038/srep21109.

[151] T.-Y. Chu and O.-K. Song. 'Apparent Thickness Dependence of Mobility in Organic Thin Films Analyzed by Gaussian Disorder Model'. In: *Journal of Applied Physics* 104.2 (2008), p. 023711. DOI: 10.1063/1.2959825.

[152] S. L. M. van Mensfoort, V. Shabro, R. J. de Vries, R. a. J. Janssen and R. Coehoorn. 'Hole Transport in the Organic Small Molecule Material α-NPD: Evidence for the Presence of Correlated Disorder'. In: *Journal of Applied Physics* 107.11 (2010), p. 113710. DOI: 10.1063/1.3407561.

[153] T. D. Anthopoulos, J. P. J. Markham, E. B. Namdas, I. D. W. Samuel, S.-C. Lo and P. L. Burn. 'Highly Efficient Single-Layer Dendrimer Light-Emitting Diodes with Balanced Charge Transport'. In: *Applied Physics Letters* 82.26 (2003), pp. 4824–4826. DOI: 10.1063/1.1586999.

[154] A. Fediai, F. Symalla, P. Friederich and W. Wenzel. 'Disorder Compensation Controls Doping Efficiency in Organic Semiconductors'. In: *Nature Communications* 10.1 (2019), p. 4547. DOI: 10.1038/s41467-019-12526-6.

[155] A. Fediai, A. Emering, F. Symalla and W. Wenzel. 'Disorder-Driven Doping Activation in Organic Semiconductors'. In: *Physical Chemistry Chemical Physics* 22.18 (2020), pp. 10256–10264. DOI: 10.1039/D0CP01333A.

[156] W. Gao and A. Kahn. 'Controlled p doping of the hole-transport molecular material *N*,*N*′-diphenyl-*N*,*N*′-bis(1-naphthyl)-1,1′-biphenyl-4,4′-diamine with tetrafluorotetracyanoquinodimethane'. In: *Journal of Applied Physics* 94.1 (2003), pp. 359–366. DOI: 10.1063/1.1577400.

[157] V. Ambegaokar, B. I. Halperin and J. S. Langer. 'Hopping Conductivity in Disordered Systems'. In: *Physical Review B* 4.8 (1971), pp. 2612–2620. DOI: 10.1103/PhysRevB.4.2612.

[158] V. I. Arkhipov. 'Effect of Doping on the Density-of-States Distribution and Carrier Hopping in Disordered Organic Semiconductors'. In: *Physical Review B* 71.4 (2005). DOI: 10.1103/PhysRevB.71.045214.

[159] M. Mesta, H. van Eersel, R. Coehoorn and P. A. Bobbert. 'Kinetic Monte Carlo Modeling of the Efficiency Roll-off in a Multilayer White Organic Light-Emitting Device'. In: *Applied Physics Letters* 108.13 (2016), p. 133301. DOI: 10.1063/1.4945087.

[160] M. L. Tietze, J. Benduhn, P. Pahner, B. Nell, M. Schwarze, H. Kleemann, M. Krammer, K. Zojer, K. Vandewal and K. Leo. 'Elementary Steps in Electrical Doping of Organic Semiconductors'. In: *Nature Communications* 9.1 (2018), p. 1182. DOI: 10.1038/s41467-018-03302-z.

[161] S. Bag, P. Friederich, I. Kondov and W. Wenzel. 'Concentration Dependent Energy Levels Shifts in Donor-Acceptor Mixtures Due to Intermolecular Electrostatic Interaction'. In: *Scientific Reports* 9.1 (2019), p. 12424. DOI: 10.1038/s41598-019-48877-9.

[162] S. Grimme. 'Semiempirical Hybrid Density Functional with Perturbative Second-Order Correlation'. In: *The Journal of Chemical Physics* 124.3 (2006), p. 034108. DOI: 10.1063/1.2148954.

[163] T. Yanai, D. P. Tew and N. C. Handy. 'A new hybrid exchange–correlation functional using the Coulomb-attenuating method (CAM-B3LYP)'. In: *Chemical Physics Letters* 393.1 (2004), pp. 51–57. DOI: 10.1016/j.cplett.2004.06.011.

[164] K. Aidas et al. 'The Dalton Quantum Chemistry Program System'. In: *WIREs Computational Molecular Science* 4.3 (2014), pp. 269–284. DOI: 10.1002/wcms.1172.

[165] E. Runge and E. K. U. Groß. 'Density-Functional Theory for Time-Dependent Systems'. In: *Physical Review Letters* 52.12 (1984), pp. 997–1000. DOI: 10.1103/PhysRevLett.52.997.

[166] J. S. Binkley, J. A. Pople and W. J. Hehre. 'Self-Consistent Molecular Orbital Methods. 21. Small Split-Valence Basis Sets for First-Row Elements'. In: *Journal of the American Chemical Society* 102.3 (1980), pp. 939–947. DOI: 10.1021/ja00523a008.

[167] K. D. Dobbs and W. J. Hehre. 'Molecular Orbital Theory of the Properties of Inorganic and Organometallic Compounds. 4. Extended Basis Sets for Third-and Fourth-Row, Main-Group Elements'. In: *Journal of Computational Chemistry* 7.3 (1986), pp. 359–378. DOI: 10.1002/jcc.540070313.

[168] K. D. Dobbs and W. J. Hehre. 'Molecular Orbital Theory of the Properties of Inorganic and Organometallic Compounds. 5. Extended Basis Sets for First-Row Transition Metals'. In: *Journal of Computational Chemistry* 8.6 (1987), pp. 861–879. DOI: 10.1002/jcc.540080614.

[169] K. D. Dobbs and W. J. Hehre. 'Molecular Orbital Theory of the Properties of Inorganic and Organometallic Compounds. 6. Extended Basis Sets for Second-Row Transition Metals'. In: *Journal of Computational Chemistry* 8.6 (1987), pp. 880–893. DOI: 10.1002/jcc.540080615.

[170] M. S. Gordon, J. S. Binkley, J. A. Pople, W. J. Pietro and W. J. Hehre. 'Self-Consistent Molecular-Orbital Methods. 22. Small Split-Valence Basis Sets for Second-Row Elements'. In: *Journal of the American Chemical Society* 104.10 (1982), pp. 2797–2803. DOI: 10.1021/ja00374a017.

[171] W. J. Pietro, M. M. Francl, W. J. Hehre, D. J. DeFrees, J. A. Pople and J. S. Binkley. 'Self-Consistent Molecular Orbital Methods. 24. Supplemented Small Split-Valence Basis Sets for Second-Row Elements'. In: *Journal of the American Chemical Society* 104.19 (1982), pp. 5039–5048. DOI: 10.1021/ja00383a007.

[172] Q. T. Le, L. Yan, Y. Gao, M. G. Mason, D. J. Giesen and C. W. Tang. 'Photoemission study of aluminum/tris-(8-hydroxyquinoline)-aluminum and aluminum/LiF/tris-(8-hydroxyquinoline) aluminum interfaces'. In: *Journal of Applied Physics* 87.1 (2000), pp. 375–379. DOI: 10.1063/1.371870.

[173] I. A. Lysenko, L. A. Patrashanu and D. D. Zykov. 'Organic Light Emitting Diode Simulation Using Silvaco TCAD Tools'. In: *International Siberian Conference on Control and Communications (SIBCON)*. 2016, pp. 1–5. DOI: 10.1109/SIBCON.2016.7491782.

[174] P. Langevin. 'Recombinaison et Mobilites Des Ions Dans Les Gaz'. In: *Annales de Chimie et de Physique* 28.433 (1903), p. 122.

[175] W. Brütting, J. Frischeisen, T. D. Schmidt, B. J. Scholz and C. Mayr. 'Device Efficiency of Organic Light-Emitting Diodes: Progress by Improved Light Outcoupling'. In: *physica status solidi (a)* 210.1 (2013), pp. 44–65. DOI: 10.1002/pssa.201228320.

[176] D. S. Setz et al. 'Comprehensive Efficiency Analysis of Organic Light-Emitting Devices'. In: *Journal of Photonics for Energy* 1.1 (2011), p. 011006. DOI: 10.1117/1.3528274.

[177] F. Symalla, S. Heidrich, M. Kubillus, T. Strunk, T. Neumann and W. Wenzel. '19-4: Boosting OLED Performance with Ab-initio Modeling of Roll-off and Quenching Processes'. In: *SID Symposium Digest of Technical Papers* 50.1 (2019), pp. 259–262. DOI: 10.1002/sdtp.12905.

DANKSAGUNG

An dieser Stelle möchte ich mich bei allen bedanken, die mich während meiner Promotion begleitet und unterstützt haben.

Mein Dank gilt besonders Prof. Dr. Wolfgang Wenzel für die Gelegenheit zur Durchführung dieser Promotion, das große Vertrauen, sowie die Freiheit bei der Wahl meiner Schwerpunkte. Mein Dank gilt außerdem Prof. Dr. Markus Garst für das Korreferieren dieser Arbeit und die Flexibilität bei meiner am Ende sehr spontanen Terminanfrage.

Vielen Dank gilt meinen Bürokollegen, Manuel K. und Carl, sowie unserem Nachzügler Deniz, für die hervorragende Stimmung im Büro, die vielen spannenden Diskussionen und Gespräche, nicht zuletzt eurer Offenheit für mich, als bekennenden Teetrinker, in eurer Kaffeerunde.

Herzlichen Dank auch an die Kollegen bei Nanomatch, hier insbesondere Franz, Timo und Tobi. Ohne die sehr enge und fruchtbare Zusammenarbeit wäre diese Promotion so nicht möglich gewesen. Darüber hinaus vielen Dank für die zahlreichen fachlichen Diskussionen und euer stets offenes Ohr bei allen (nicht)wissenschaftlichen Problemen.

Darüber hinaus danke ich allen weiteren Kollegen der AG Wenzel, insbesondere Manuel R., Artem, Jörg, Tobi S., Montserrat, Shahriar, Praneeth, Mariana, Yohannes und Pascal, sowie den Mitgliedern der AG Schug, hier besonders Oskar, Ines und Claude, für zahlreiche schöne Stunden auf dem Weg zur und in der Mensa, bei Kuchen, dem Wochenabschlussbier und dem sonstigen Miteinander.

Ich danke der Baden-Württemberg-Stiftung für die Finanzierung meiner Arbeit im Rahmen des Projekts 'Multi-Skalen-Modellierung von Materialien und Bauelementen für die Energieumwandlung'.

Zu guter Letzt danke ich meiner Freundin Alexandra, die mich über den gesamten Zeitraum der Promotion stets unterstützt hat und, ins-

besondere im Endspurt, etliche Male kürzer getreten ist, um mir den Rücken für die Fertigstellung der Dissertation frei zu halten.